UNIVERSIDADE DE SÃO PAULO
INSTITUTO DE FÍSICA DE SÃO CARLOS

FILIPE ASSIS COUTO

Fabrication of polymeric microresonators doped with nanodiamonds for quantum information technologies

São Carlos
2024

FILIPE ASSIS COUTO

Fabrication of polymeric microresonators doped with nanodiamonds for quantum information technologies

Thesis presented to the Graduate Program in Physics at the Instituto de Física de São Carlos, Universidade de São Paulo to obtain the degree of Doctor of Science.

Concentration area: Theoretical and Experimental Physics

Advisor: Prof. Dr. Cleber Renato Mendonça

Corrected Version

((original version available on the Program Unit)

São Carlos

2024

Couto, Filipe Assis
Fabrication of polymeric microresonators doped with nanodiamonds for quantum information technologies / Filipe Assis Couto; advisor Cleber Renato Mendonça - corrected version -- São Carlos 2024.
107 p.

Thesis (Doctorate - Graduate Program in Theoretical and Experimental Physics) -- Instituto de Física de São Carlos, Universidade de São Paulo - Brasil , 2024.

1. Two-photon polymerization. 2. Color centers. 3. Whispering gallery modes. I. Mendonça, Cleber Renato, advisor. II. Title.

In memory of Luiz Carlos de Andrade

ACKNOWLEDGEMENTS

First, I would like to express my sincere gratitude to my advisor, Prof. Dr. Cleber Renato Mendonça, who welcomed me into his research group since my undergraduate years, and whose genuine passion and curiosity have been an inspiration since day one. It has been a true privilege to be mentored by such an amazing scientist and person, who is always looking for the best of his students.

I would also like to thank all members of the Photonics Group, an incredible and welcoming scientific community, especially thanks to Prof. Dr. Lino Misoguti and Prod. Dr. Leonardo de Boni, who were always available to share their deep knowledge and provide valuable insights. I would also like to thank our laboratory technician André Romero, for all the assistance and friendship.

I would also like to express my sincere gratitude to Prof. Dr. Nathália Tomazio and Prof. Dr. Adriano Otuka for all their help, and for laying the foundation for this work.

I wish to express my sincere gratitude to Prof. Dr. Sérgio Muniz and his students, for providing the nanodadiamonds used in this work, ODMR measuraments and many fruitful insights.

I would like to express my sincere gratitude to Prof. Dr. Evelyn Hu and her students for their warm hospitality during my internship at their group. I am grateful for the opportunity to have learned from them and for all the knowledge they shared. It was an amazing period that truly enriched my academic development.

My deepest gratitude goes to all the staff and professors at the University of São Paulo and the São Carlos Institute of Physics, who provided an outstanding environment for academic development.

I would like to thank my family and friends for their care and support throughout this journey. A special thanks to my mother, Neide, for her unwavering strength, her love and support.

I would like to acknowledge the financial support of the following funding agencies: CAPES, CNPq, and the U.S. Air Force. I am particularly grateful to the São Paulo Research Foundation (FAPESP) grant number 2020/08715-2, which funded this research, and for FAPESP grant number 2022/13615-2, which supported my internship abroad.

Finally, my deepest gratitude to my wife Nathalie, for her love and partnership, and for the many times that she takes the burden during the challenging moments of this journey.

“Nothing is too wonderful to be true,
if it be consistent with the laws of nature”

Michael Faraday

ABSTRACT

COUTO, F.A. **Fabrication of polymeric microresonators doped with nanodiamonds for quantum information technologies**: 2024. 107 p. Thesis (Doctor in Science) – Instituto de Física de São Carlos, Universidade de São Paulo, São Carlos, 2024.

Color centers have attracted significant attention for their applications in quantum technology, making their integration into photonic structures an essential area of research to advance the realization of quantum platforms. In particular, resonant cavities offer a promising platform for enhancing the light-matter interaction of color centers. This work explores the fabrication of microcavities embedded with fluorescent nanodiamonds using two-photon polymerization (2PP). We investigate the trade-off between nanodiamond concentration in the photoresist and the resulting structural quality and cavity Q-factor. Our results demonstrate the successful integration of nanodiamonds into cylindrical cavities doped with 0.002 wt% concentration. These cavities maintain good quality factors on the order of 10^5 and contain one to three fluorescent color centers. The position of the fluorescent nanodiamonds within the microcavities is confirmed using fluorescence spectroscopy, laser scanning microscopy (LSM), and Raman spectroscopy. Additionally, utilizing Finite-Difference Time-Domain (FDTD) simulations, we explore novel designs for efficient emitter-cavity coupling with color centers in 4H-Silicon Carbide (SiC) nanostructures. We optimized a double nanobeam cavity design supporting high-quality factor resonances and a "sawfish" cavity design for improved fabrication and light-matter interaction with color center in SiC. Building upon this knowledge, we discuss future directions for leveraging 2PP fabrication to integrate nanodiamonds with novel Whispering Gallery Modes (WGM) cavities, aiming at achieving low mode volumes to explore the Purcell effect. Therefore, this research paves the way for developing integrated devices containing nanodiamonds and WGM cavities for quantum technology applications.

Keywords: Two-photon polymerization. Color centers. Whispering gallery modes.

RESUMO

COUTO, F.A. **Fabricação de microresonadores poliméricos dopados com nanodiamantes para aplicações em tecnologias de informação quântica**: 2024. 107 p. Thesis (Doctor in Science) – Instituto de Física de São Carlos, Universidade de São Paulo, São Carlos, 2024.

Centros de cor têm recebido significativa atenção devido ao seu uso em aplicações de tecnologia quântica, tornando importante pesquisas envolvendo sua integração em estruturas fotônicas. Em particular, cavidades fotônicas são uma promissora plataforma para aumentar a interação da radiação com a matéria usando centros de cor. Neste trabalho, exploramos a fabricação de microcavidades dopadas com nanodiamantes fluorescentes usando fotopolimerização por absorção de dois fótons (A2F). Investigamos o compromisso entre a concentração de nanodiamantes no fotoresiste e a qualidade das estruturas fabricadas. Os resultados demonstram a integração bem-sucedida de nanodiamantes em cavidades cilíndricas dopadas com 0,002% em peso de nanodiamantes, mantendo fatores de qualidade na ordem de 10^5. A posição dos nanodiamantes fluorescentes dentro das microcavidades foi confirmada por meio de espectroscopia de fluorescência, microscopia confocal e espectroscopia Raman. Além disso, utilizando simulações via o método de Diferenças Finitas no Domínio do Tempo, exploramos novas estruturas para promover o acoplamento eficiente entre centros de cor em Carbeto de Silício (SiC) e nanocavidades fotônicas. O *design* de uma dupla cavidade de cristal fotônico que suporta duas ressonâncias com alto fator de qualidade foi otimizada, e o *design* de uma nova geometria (cavidade do tipo *sawfish*) foi explorado com o intuito de facilitar a fabricação e melhorar a interação emissor-cavidade. Utilizando os conhecimentos adquiridos, foram propostos caminhos futuros para empregar a técnica de A2F para a integração de nanodiamantes em novas cavidades fotônicas que suportam modos de galeria sussurrante, com o objetivo de produzir estruturas com pequeno volume modal para explorar o engrandecimento Purcell. Portanto, este trabalho abre caminho para o desenvolvimento de estruturas fotônicas integradas contendo nanodiamantes, bem como cavidades fotônicas para aplicações em tecnologias quânticas.

Palavras-chave: Fotopolimerização por absorção de dois fótons. Centros de cor. Modos de galeria sussurrante.

LIST OF FIGURES

LIST OF ABBREVIATIONS AND ACRONYMS

2D	Two-dimensional
3D	Three-dimensional
2PP	Two-photon polymerization
BC	Boundary conditions
DLW	Direct laser writing
FDTD	Finite-difference time domain
FEM	Finite-elements
FWHM	Full width at half maximum
IR	Infrared
LSM	Laser scanning microscopy
NA	Numerical aperture
NV	Nitrogen vacancy
ODMR	Optically detected magnetic resonance
PML	Perfect-matched layer
SEM	Scanning electron microscopy
SIC	Silicon carbide
TE	Transversal electric
TM	Transversal magnetic
WGM	Whispering gallery modes
ZPL	Zero-phonon line

CONTENTS

1 Introduction

The field of photonics plays a major role in modern technologies, as photons are not only the primary carriers of information, but also serve as crucial platforms for data production across various applications such as radars, lidars, sensors, and spectroscopy. Additionally, the physical limitations of electronic devices will likely impact their scalability and energy efficiency in the future,[1] making photonic and optoelectronic devices a promising alternative to push the limits in information processing[2]. In addition, the onset of quantum technology applications adds relevance to photonic systems, as photons can interact with spin qubits, preparing and reading out their spin state, enabling the realization of quantum platforms for many applications, such as cryptography[3] single photon generation,[4] and sensing[5].

To realize these applications, it is necessary to have quantum systems with suitable properties to act as qubits, along with their integration into photonic devices capable of confining, guiding, and enhancing their emission[6]. Although significant progress has been made, an ideal scalable platform that operates at room temperature, and exhibiting sufficient error tolerance remains a challenge[7]. Therefore, research in material science and device engineering is of paramount importance.

Several systems have been explored as qubits, such as quantum dots,[8] single molecules,[9] superconducting circuits,[10] and defects in crystals (also known as color centers). The latter is particularly interesting for applications in quantum technologies due to features such as high coherence times, integration with photonic materials, and stable emission properties. Color centers form due to point defects in semiconductors, resulting from a missing, substitutional, or interstitial atom in the crystal lattice. These defects create localized energy states, behaving similarly to isolated atoms. When these energy states fall within the semiconductor’s bandgap, they can interact with incident radiation, emitting photons that freely propagate outside the material. This phenomenon adds colors that would not be present in a pristine crystal lattice, hence the term "color center”.

Among many color centers found in different materials, the NV^- defect in diamond stands out as particularly promising. This defect features a spin state that can be optically set and read out, along with single photon emission at room temperature, long coherence time,[11] and photo-stability since it does not present photoblinking or photobleaching.[12-13] This color center has been used in diverse fields, including cell

marking in biological applications,[14-15] as well as numerous studies in quantum information processing and single-photon generation.[16–18] Besides presenting many interesting properties, the NV^- center still suffers from a broad phonon sideband at room temperature,[19] which reduces the coherence and emission rate of indistinguishable photons, necessary for many applications. To overcome these limitations, it is of foremost importance to incorporate these emitters into photonic cavities to exploit the Purcell enhancement.[19]

There are two approaches to promote such integration. One is fabricating cavities in bulk diamond and incorporating the color centers into the cavity by ion implantation. Due to its inherent hardness, fabrication in bulk diamond is complex, and structures often suffer from high surface roughness, which degrades their optical properties. Only recently high Q-factor photonic-crystal nanocavities have been fabricated in diamond,[20] using a special V-undercut technique to promote optical insulation, while preserving good surface roughness. Despite the aforementioned progress, this approach is still challenging and requires complex and time-consuming fabrication techniques. Also, the placement of the defects by ion implantation has downsides, such as the non-deterministic positioning of the defects, implantation of undesirable additional defects, and strain in the material that can degrade the color center optical properties.[21]

The second approach, called the hybrid approach,[19] consists in using nanodiamonds as a platform to integrate color centers into structures fabricated in a variety of host materials such as SiC,[19] SiO_2,[22] and GaP.[23] Hence, nanodiamonds integrated with photonic cavities have been the subject of intense research, such as polystyrene microspherical resonators,[24] where the nanodiamonds are positioned outside the spheres using a near-field scanning optical microscopy tip, showing the coupling of the emission of the color center with the WGM's of the resonators. Additionally, researchers have used GaP microdisks fabricated over a diamond substrate to couple, via evanescent wave, the NV color center emission into the modes of the microdisks.[25] More recently, Fabry-Pérot cavities formed with diamond membranes were used to enhance the emission at the zero-phonon line (ZPL) of the NV centers up to 15 times.[26-27] Other approaches, such as photonic crystals[27] and waveguides[28-29] have also been explored. Even though much progress has been made, it is still a challenge to position the nanodiamonds inside the volume of the structures and, consequently, the interaction with the color centers occurs mainly via

the evanescent field of the devices.[19] Also, most of the aforementioned studies still demand complex steps and clean rooms to fabricate the resonant structures, and they are only feasible in inorganic materials. In addition, the methods used to integrate the diamond color centers with the resonators are either complex or present low control regarding the number of emitters.

In order to expand the variety of materials and methods to promote the integration of nanodiamonds in photonic structures, two-photon polymerization (2PP) is a promising technique. Two-photon polymerization is a direct laser writing (DLW) method that exploits the nonlinear absorption of a photoresist to produce structures with sub-diffraction resolution, with nearly arbitrary shapes, and has been used to create a variety of structures for applications in many fields, such as photonic crystals,[30] waveguides,[31] and microneedles.[32] In particular, optical microresonators with good optical qualities can be produced via the 2PP technique.[33]

One interesting feature of 2PP is that it allows relatively simple incorporation of dopants into the photoresist,[34] which makes it an appropriate method to fabricate functional structures, such as nanotube-doped structures,[35] rhodamine-doped and graphene oxide doped microresonators.[36-37] Hence, incorporating nanodiamonds into the resist is an interesting approach to exploit the flexibility of the 2PP technique to produce arbitrary structures with color centers incorporated in their volume, addressing an important issue of the hybrid approach.

In this context, the main objective of this work is to study the incorporation of color centers into photonic cavities, including incorporating nanodiamonds into structures fabricated via 2PP technique, focusing on WGM resonators, and also cavity engineering for optimizing cavity-emitter integration. This work is organized as follows: Chapter 2 will explore fundamental concepts, such as the electromagnetic nature of the WGM resonances and its coupling properties with waveguides, the principles of color centers and its integration into resonant cavities, and aspects regarding the 2PP technique and two-photon absorption. In Chapter 3, we will describe the process of incorporating the nanodiamonds into the photoresist, go through the details of the 2PP setup and fabrication methodology, briefly explain the production of tapered optical fibers and the setup used to promote coupling with the resonators, and discuss the confocal spectroscopy setup assembled to localize and analyze the photoluminescence spectrum of the color centers. In Chapter 4, we will present the nanodiamond doped structures produced via 2PP and characterize their optical

properties and nanodiamond distribution. Chapter 5 describes the work regarding cavity engineering for color center integration, developed during an internship period. The motivation for cavity engineering is discussed, and we will also describe the numerical methods utilized and present the obtained results. In Chapter 6, we will apply similar methodologies to the ones discussed in Chapter 5, to numerically study the structures fabricated via 2PP, and propose new geometries to obtain better emitter-cavity coupling. Finally, Chapter 7 will present the overall perspective of the results presented in Chapters 4, 5, and 6, and discuss future applications of the results obtained in this work.

2 Theory

2.1 Fundamental aspects of whispering gallery modes

Whispering gallery modes (WGM) are resonances that occur in circular symmetry systems, formed by a wave propagating near the rim of a circular-shaped reflective interface through successive reflections. The phenomenon was first observed in acoustics, where a person whispering at a point near a wall of a circular room could be heard on the opposite side. In optics, WGMs can appear in a dielectric structure with circular symmetry, through total internal reflections at its interface[38].

For cylindrical dielectric resonators, far from the extremities, we can neglect border effects and consider the resonances to be independent of the z-coordinate, reducing the problem to a 2D model, as depicted in Fig. 2.1. In this situation, for linear media without absorption and adopting cylindrical coordinates, it is possible to obtain an analytical solution from Maxwell equations.

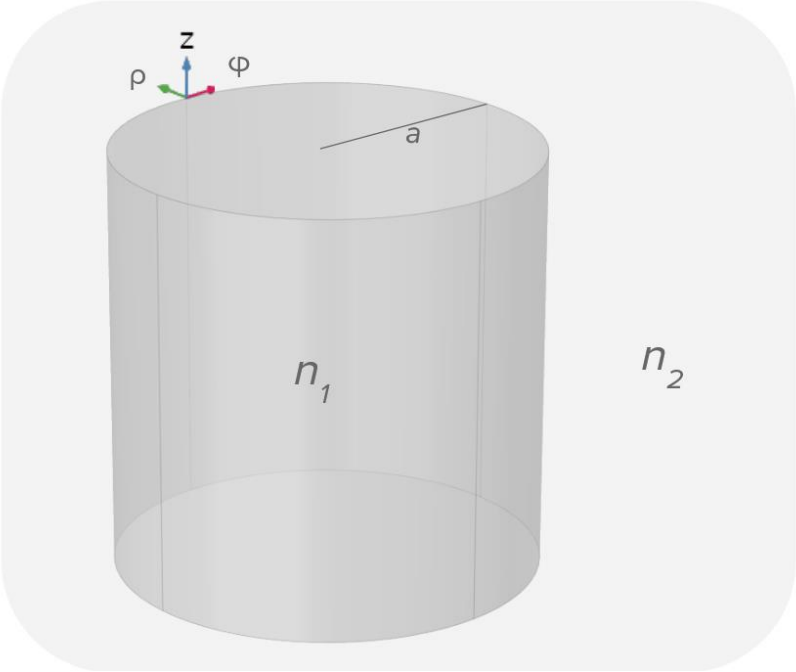

Figure 2.1 - Schematics of the resonator and the vectors for the cylindrical coordinate system adopted, as well as definition of the index distribution, where n_1 stands for index inside the resonator, and n_2 for the exterior region. The radii parameter is defined as *a*.
Source: By the author

Given Maxwell equations in linear lossless media:

$$\nabla.\vec{E} = 0 \tag{2.1}$$

$$\nabla.\vec{B} = 0 \tag{2.2}$$

$$\nabla \times \vec{E} = \frac{-\partial \vec{B}}{\partial t} \tag{2.3}$$

$$\nabla \times \vec{B} = \mu\epsilon \frac{\partial \vec{E}}{\partial t} \tag{2.4}$$

and the constitutive relations:

$$\vec{D} = \epsilon\vec{E} \tag{2.5}$$

$$\vec{B} = \mu\vec{H} \tag{2.6}$$

we will assume that the fields have harmonic temporal dependency at the form $e^{i\omega t}$, hence:

$$\frac{\partial \vec{E}}{\partial t} = i\omega\vec{E}(\vec{r})e^{i\omega t} \tag{2.7}$$

Taking the curl of Faraday and Ampere/Maxwell equations and using the identity $\nabla \times (\nabla \times \phi) = \nabla(\nabla.\phi) - \nabla^2\phi$, we obtain the Helmholtz equations for the electric and magnetic fields:

$$\nabla^2\vec{E} = -\mu\epsilon\omega^2\vec{E}(\rho,\phi) = -k^2\vec{E}(\rho,\phi) \tag{2.8}$$

$$\nabla^2\vec{H} = -\mu\epsilon\omega^2\vec{H}(\rho,\phi) = -k^2\vec{H}(\rho,\phi) \tag{2.9}$$

Since $\mu = \mu_0$ and $= \epsilon_0 n^2$, we can rewrite $\mu\epsilon\omega^2 = \frac{n^2\omega^2}{c^2} = k^2 = \frac{2\pi\lambda_0}{n}$.

Given the geometry of the problem, it is convenient to express the fields in cylindrical coordinates:

$$\vec{E}(\rho,\phi) = E_\rho(\rho,\phi)\hat{\rho} + E_\phi(\rho,\phi)\hat{\phi} + E_z(\rho,\phi)\hat{z} \tag{2.10}$$

$$\vec{B}(\rho,\phi) = B_\rho(\rho,\phi)\hat{\rho} + B_\phi(\rho,\phi)\hat{\phi} + B_z(\rho,\phi)\hat{z} \tag{2.11}$$

Considering that the problem is not dependent on the *z* component, it is convenient to separate the solutions into a set of TM (where $B_z = 0$) and TE (where$E_z = 0$) modes. In this text, we will solve the problem for the TE mode only, but it is straightforward to apply the same methods described below for the TM modes.

Taking the curl of $\vec{E}$, assuming $E_z = 0$ and $\vec{B} = \vec{B}(\rho,\phi)$, we obtain:

$$\nabla \times \vec{E} = \frac{1}{\rho}\left[\rho \frac{\partial E_\phi}{\partial \rho} - \frac{\partial E_\phi}{\partial \phi}\right] \hat{z} = -i\omega \vec{B} \tag{2.12}$$

which implies that:

$$B_\phi = B_\rho = 0 \tag{2.13}$$

Hence, the magnetic field has only the *z* component.

Taking the curl of $\vec{B}$:

$$\nabla \times \vec{B} = \left(\frac{1}{\rho}\frac{\partial B_z}{\partial \phi}\hat{\rho} - \frac{\partial B_z}{\partial \rho}\hat{\phi}\right) e^{i\omega t} = i\omega\mu_0 \epsilon \vec{E}(\rho, \phi) e^{i\omega t} \tag{2.14}$$

we can relate the components of the electric field to the derivatives of the magnetic field as:

$$E_\rho = \frac{-i}{\omega\mu_0\epsilon\rho}\frac{\partial B_z}{\partial \phi} \tag{2.15}$$

$$E_\phi = \frac{i}{\omega\mu_0\epsilon}\frac{\partial B_z}{\partial \rho} \tag{2.16}$$

Hence, the problem is reduced to finding the solution for the *z* component of the magnetic field. To find B_z, we will start with the wave equation for the magnetic field[39]:

$$(\nabla^2 + k) B_z(\rho, \phi) = 0 \tag{2.17}$$

Substituting (2.11) in (2.17) and expanding the Laplacian in cylindrical coordinates, we obtain:

$$\rho^2 \frac{\partial^2 B_z}{\partial \rho^2} + \rho \frac{\partial B_z}{\partial \rho} + \frac{\partial^2 B_z}{\partial \phi^2} + \rho^2 k^2 B_z = 0 \tag{2.18}$$

Using the method of separation of variables, where we will consider the magnetic field as a product of two functions $B_z = F(\phi)R(\rho)$, substituting in Eq. 2.18 we have:

$$\rho^2 \frac{1}{R}\frac{d^2R}{d\rho^2} + \rho \frac{1}{R}\frac{dR}{d\rho} + \frac{1}{F}\frac{d^2F}{d\phi^2} = -\rho^2 k^2 \tag{2.19}$$

Since F is only a function of ϕ, we can assume that $\frac{1}{F}\frac{d^2F}{d\phi^2} = -m^2$, where m is a constant, hence:

$$F(\phi) = \alpha e^{\pm im\phi} \tag{2.20}$$

$$\rho^2 \frac{d^2R}{d\rho^2} + \rho \frac{dR}{d\rho} + R(\rho^2 k^2 - m^2) = 0 \tag{2.21}$$

Now, it is possible to proceed with the substitution of variables $x = \rho k, y = R\left(\frac{\rho}{k}\right)$. Considering that:

$$\frac{dR}{d\rho} = \frac{dy}{dx}\frac{dx}{d\rho} = \frac{dy}{dx}k \tag{2.22}$$

$$\frac{d^2R}{d\rho^2} = \frac{d}{d\rho}\left[\frac{dy}{dx}k\right] = k^2\frac{d^2y}{dx^2} \tag{2.23}$$

we can transform Eq. 2.21 in a Bessel equation, where $x = \rho k$ [40]:

$$x^2 \frac{d^2y}{dx^2} + x\frac{dy}{dx} + y(x^2 - m^2) = 0 \tag{2.24}$$

At this point, it is necessary to separate the solutions for the regions inside ($\rho < a$) and outside ($\rho > a$) the cylinder, and impose the following physical considerations: the solutions are non-divergent, and evanescent outside the cylinder to obtain the confined modes. Inside the cylinder, we have:

$$H_z(\rho, \phi) = A_m J_m^1(\rho k_1) e^{im\phi}, \rho < a \tag{2.25}$$

In the previous equation, J_m^1 is the Bessel function of first kind and $k_1 = \frac{2\pi}{\lambda_0} n_1$. The Bessel functions of second kind are also a solution, but are discarded since they diverge when $\rho = 0$[40]. For the solutions outside the cylinder, we have:

$$H_z(\rho, \phi) = B_m H_m^2(\rho k_2) e^{im\phi}, \rho > a \tag{2.26}$$

where H_m^2 is the Hankel function of second kind, which satisfies the evanescent wave condition, and $k_2 = \frac{2\pi}{\lambda_0} n_2$ [40].

To create a stationary wave, the fields must have the same amplitude after a round trip. Therefore, the equation $E(\rho,\phi) = E(\rho,\phi + 2\pi)$ must be satisfied. This implies that the solutions are a discrete set of modes indexed by \$m$, that must be an integer.

Substituting Eqs. (25) and (26) in Eqs. (15) and (16), we obtain the components for the electric fields:

$$E_\rho = \frac{m}{\omega\mu_0\epsilon_1\rho} A_m J_m^1(\rho k_1) e^{im\phi}, \rho < a \tag{2.27}$$

$$E_\rho = \frac{m}{\omega\mu_0\epsilon_2\rho} B_m H^2(\rho k_2) e^{im\phi}, \rho > a \tag{2.28}$$

$$E_\phi = \frac{ik_1}{\omega\mu_0\epsilon_1} A_m J_m^{'1}(\rho k_1) e^{im\phi}, \rho < a \tag{2.29}$$

$$E_\phi = \frac{ik_2}{\omega\mu_0\epsilon_2} B_m H_m^{'2}(\rho k_2) e^{im\phi}, \rho > a \tag{2.30}$$

where we used: $\frac{\partial f(\rho k)}{\partial \rho} = \frac{\partial(\rho k)}{\partial \rho}\frac{\partial f(\rho k)}{\partial(\rho k)} = k\frac{\partial f(\rho k)}{\partial(\rho k)}$, and the definition $' \equiv \frac{\partial}{\partial(\rho k)}$.

Considering now that the tangential components of the fields must be continuous at the interface, we have [39]:

$$A_m J_m^1(ak_1) e^{im\phi} = B_m H_m^2(ak_1) e^{im\phi} \tag{2.31}$$

$$\frac{ik_1}{\omega\mu_0\epsilon_1} A_m J_m^{'1}(ak_1) e^{im\phi} = \frac{ik_2}{\omega\mu_0\epsilon_2} B_m H_m^{'2}(ak_2) e^{im\phi} \tag{2.32}$$

From Eqs. (31) and (32), we can obtain the transcendental equation that can be numerically solved to obtain the resonant frequencies as a function of the radii and refractive indexes for the TE modes.

$$n_1 \frac{J_m^1(ak_1)}{J_m^{'1}(ak_1)} = n_2 \frac{H_m^2(ak_2)}{H_m^{'2}(ak_2)} \tag{2.33}$$

With similar procedures, one can obtain the transcendental relation for the TM modes as:

$$n_2 \frac{J_m^1(ak_1)}{J_m^{'1}(ak_1)} = n_1 \frac{H_m^2(ak_2)}{H_m^{'2}(ak_2)} \tag{2.34}$$

Since J_m^1 is a real function, and H_m^2 is complex, the solutions of interest are real inside the resonator and complex outside. Therefore, the resonance frequencies can be obtained from the root of Eqs. (2.33) and (2.34), with the condition that the imaginary

part of the right-hand side is equal to 0 when $\rho = a$, to satisfy the boundary conditions. Fig. 2.2a illustrates the possible solutions for a cylinder of radius equal to 25 μm and $n_1 = 1.5$.

We can note from Fig. 2.2b that the successive solutions represent different radial orders for the electromagnetic (EM) fields. For lower radial orders, the fields are more concentrated at the cylinder's rim, reaching high intensities, hence they are more suitable for most applications.

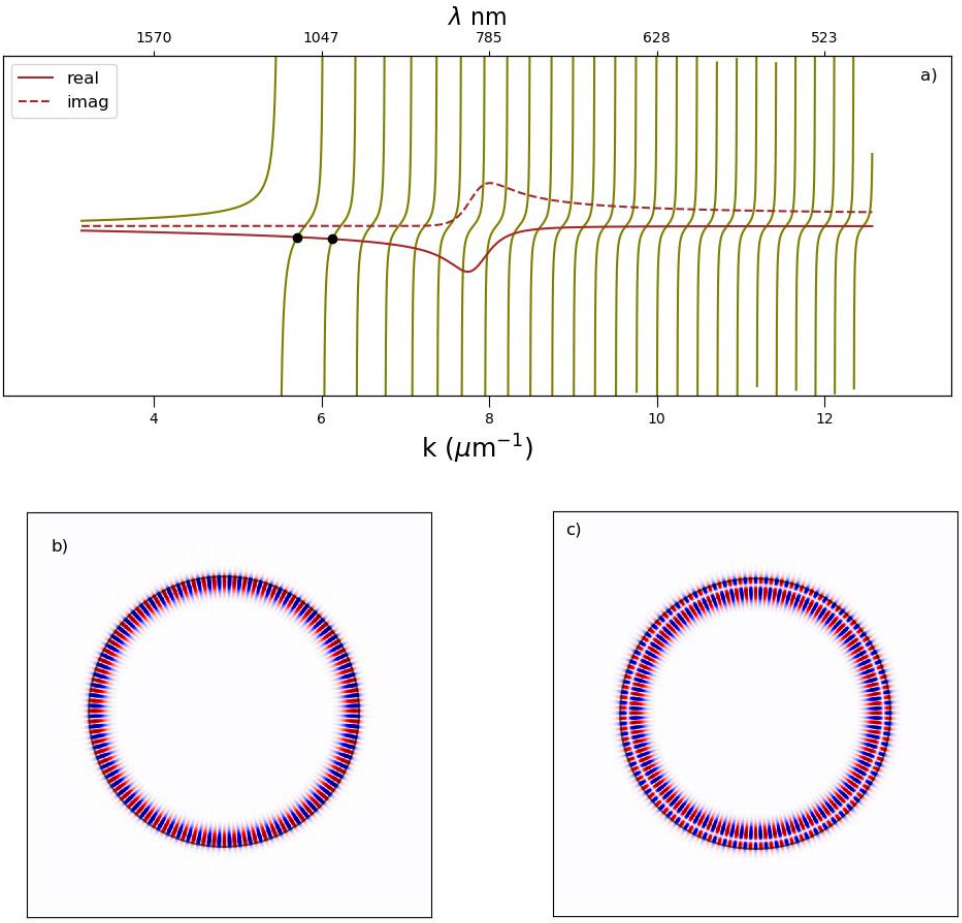

Figure 2.2 - (a) Graphical representation of the roots of equation (2.33). The black dots represent the points where the equation is satisfied, and the red-dotted line shows where the condition for the confined wave is satisfied. (b) Plot of the electric field module for the first solution. (c) Modulus of the electric field for the second solution.
Source: By the author

We can now evaluate the conditions for the total internal reflection, which constrains the possible values for m. For that, we will express the wavevector of the incident wave as:

$$\vec{k}_1 = k_\phi^{(1)}\hat{\phi} + k_\rho^{(1)}\hat{\rho} \tag{2.35}$$

and the one for the transmitted wave as:

$$\vec{k}_2 = k_\phi^{(2)}\hat{\phi} + k_\rho^{(2)}\hat{\rho} \tag{2.36}$$

To have a propagating field inside the resonator, and an evanescent field outside, $k_\rho^{(1)}$ must be real, while $k_\rho^{(2)}$ must be imaginary. Hence, we have:

$$k_\rho^{(1)} = \sqrt{k_1^{(2)^2} - k_\phi^{(1)^2}}; k_\rho^{(1)} \in R \tag{2.37}$$

$$k_\rho^{(2)} = \sqrt{k_2^{(2)^2} - k_\phi^{(2)^2}}; k_\rho^{(2)} \in C \tag{2.38}$$

Considering a wave propagating in the rim of the resonator, we can approximate the phase factor as the wavevector multiplied by the distance propagated by the wave:

$$e^{im\phi} \approx e^{ik_\phi a\phi} \tag{2.39}$$

Since the parallel component of the electric field at the interface (ϕ) must be continuous[41], k_ϕ is conserved. Thus, we can obtain a condition for the total internal reflection and the constraints for the m index as:

$$k_2 a < m < k_1 a \tag{2.40}$$

2.2 Quality factor and other important parameters of cylindrical microresonators

The quality factor of a resonant cavity is its figure of merit, and it is defined as the ratio of the total energy stored inside the resonator to the energy lost in one oscilation of the EM field trip[38]:

$$Q \equiv \omega_0 \frac{U_{stored}}{U_{dissipated}} \tag{2.41}$$

Where ω_0 is the angular frequency of the EM wave.

Since the stored energy is proportional to $\left|\vec{E}\right|^2$, we will consider an electric field with harmonic temporal dependence and complex frequency, where the imaginary part of the frequency is related to the losses, and it is defined as $\frac{1}{\tau}$ (the characteristic lifetime of the photon in the cavity). Therefore, we have:

$$\vec{E}(\vec{r},t) = \vec{E}_0(\vec{r})e^{t\left(i\omega-\frac{1}{\tau}\right)} \tag{2.42}$$

where the Q factor can be written as a function of the photon lifetime:

$$Q = \omega_0 \frac{\left|\vec{E}\right|^2}{\frac{-d}{dt}\left|\vec{E}\right|^2} = \omega_0 \frac{\tau}{2} \tag{2.43}$$

We can also apply a Fourier transform in the field of Eq. 2.42 and obtain its frequency domain relation[42]:

$$\vec{E}(\omega) = \frac{\vec{E}_0}{i(\omega-\omega_0)+\frac{1}{\tau}} \tag{2.44}$$

Note that $\left|\vec{E}(\omega)\right|^2$ is a Lorentzian-like curve with full width at half maximum (FWHM) given by $\Delta\omega = \frac{2}{\tau}$. With these results, we can rewrite the quality factor as a function of the linewidth of the resonances:

$$Q = \frac{\omega_0}{\Delta\omega} = \frac{\lambda_0}{\Delta\lambda} \tag{2.45}$$

For most applications, low radial orders are better suited because the EM fields are more confined to the resonators, reaching higher intensities than high radial orders. This can be expressed by the mode volume, defined by the integral of the electric field in the volume of the resonator, divided by the maximum field value[42]:

$$V_{modal} \approx \frac{\int \epsilon(\vec{r})\left|\vec{E}\right|^2 d^3r}{max\left(\epsilon(\vec{r})\left|\vec{E}\right|^2\right)} \tag{2.46}$$

Therefore, low radial modes have low mode volume, and fields can reach higher intensities inside the cavity.

Another relevant parameter of the resonators is the free spectral range, the spectral distance between consecutive resonances, which can be written as[38]:

$$FSR = \frac{\lambda^2}{2\pi a n_g} \tag{2.47}$$

where n_g is the group index of the mode.

Since the propagation constant is given by $e^{im\phi}$, we may rewrite it as:

$$e^{im\phi} = e^{i\beta a\phi} \tag{2.48}$$

where β is the propagation constant:

$$\beta = \frac{2\pi}{\lambda_0} n_{eff} \tag{2.49}$$

Hence, we can rewrite the FSR in terms of the azimuthal number as:

$$FSR = \frac{\lambda}{m} \tag{2.50}$$

2.3 Light coupling into the resonators

Among many methods used to couple light into cylindrical resonators, one of the most used consists of a tapered optical fiber that couples light into the resonators through evanescent wave. This method is relatively simple and permits coupling efficiency near 100%.[43]

The interaction of the resonators with the tapered fiber can be modeled as shown in Fig. 2.3, where the transmitted field is given by:

$$\vec{S}_{-2} = e^{i\beta_w(z_B - z_A)}\left(\vec{S}_{+1} - k_1^*\vec{E}\right) \tag{2.51}$$

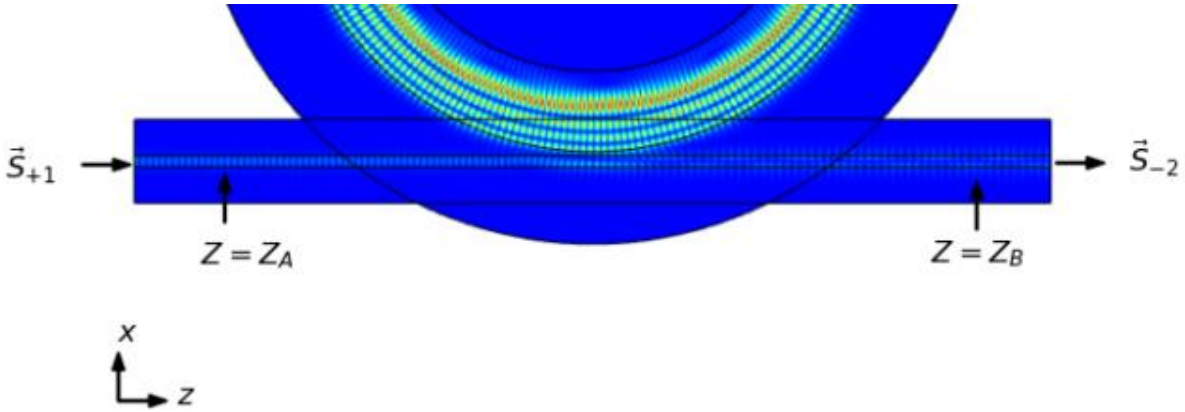

Figure 2.3 - Schematics of the model used to describe the taper-resonator interaction.
Source: By the author

In Eq. 2.31, $\vec{S}_{-2}$ and $\vec{S}_{+1}$ are respectively the transmitted field and the taper pump field, β_w is the propagation constant for the field in the taper, and k_1^* a complex coupling factor. $\vec{E}$ is the electric field inside the resonator, written as:

$$\vec{E}(\vec{r},t) = \vec{E}(\vec{r})e^{t\left[i\omega - \frac{1}{\tau_0} - \frac{1}{\tau_c}\right]} + k_1\vec{S}_{+1}t \tag{2.52}$$

In this equation, $\frac{1}{\tau_0}$ is the term accounting for losses inside the resonator, including radiative, absorption, and scattering losses, and $\frac{1}{\tau_c}$ includes the losses induced by the taper. In the frequency domain, taking ω_0 as the resonant frequency, the field can be expressed as:

$$\vec{E}(\vec{r},\omega) = \frac{k_1\vec{S}_{+1}}{i(\omega-\omega_0)+\frac{1}{\tau_0}+\frac{1}{\tau_c}} \tag{2.53}$$

and the field leaving the taper is:

$$\vec{S}_{-2} = e^{i\beta_w(z_B - z_A)}\left(\vec{S}_{+1} - k_1^*\frac{k_1\vec{S}_{+1}}{i(\omega-\omega_0)+\frac{1}{\tau_0}+\frac{1}{\tau_c}}\right) \tag{2.54}$$

Finally, we can write the transmittance as[39]:

$$T = \frac{\left|\vec{S}_{-2}\right|^2}{\left|\vec{S}_{+1}\right|^2} = \frac{(\omega-\omega_0)^2+\left(\frac{1}{\tau_0}-\frac{1}{\tau_c}\right)^2}{(\omega-\omega_0)^2+\left(\frac{1}{\tau_0}+\frac{1}{\tau_c}\right)^2} \tag{2.55}$$

One can note that factors such as the propagation constant of the taper (and hence its diameter), the gap between taper and resonator, as well as the absorption and scattering losses will define the linewidth and extinction ratio of the observed resonances.

With Eq. 2.55, it is possible to classify each resonance into three categories:

1- *Critical*, when coupling losses are equal to intrinsic losses. In this case, the transmittance at the taper reaches its minimum.

2- *Undercoupled*, when intrinsic losses are higher than coupling losses.

3- *Overcoupled,* when coupling losses are higher than intrinsic losses.

Simulating a resonator coupled to a tapered optical fiber and varying the material losses (α), it is possible to look at a particular resonance and observe the transition over the three regimes described, as shown in Fig. 2.4.

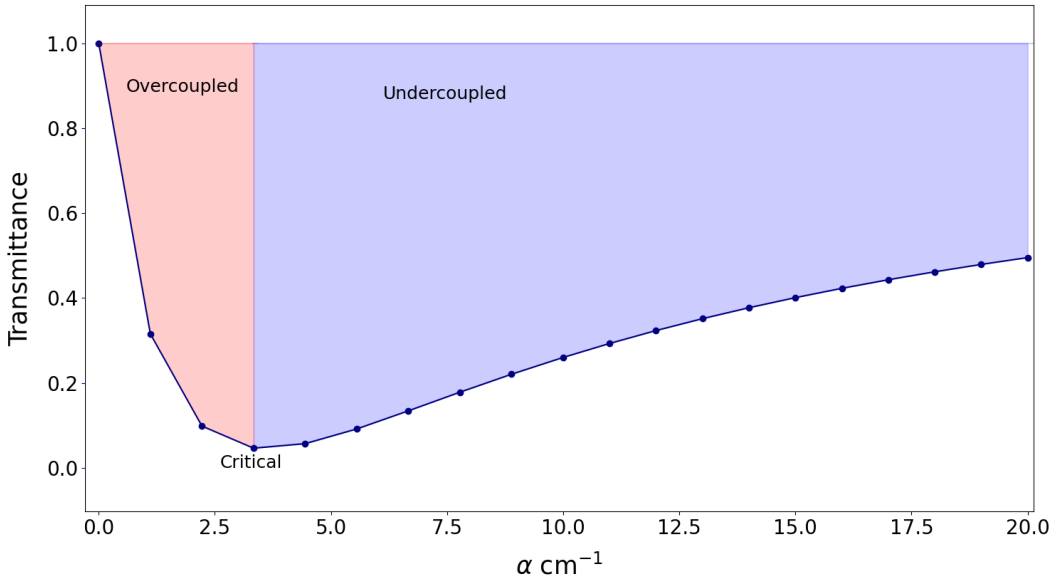

Figure 2.4 - Simulation of the taper transmittance of a particular resonance as a function of the material absorption coefficient.
Source: By the author

2.4 Nitrogen-vacancy color centers

Stable imperfections in the atomic lattice of a crystal can break the crystal symmetries and give rise to local energy levels. When these transitions are within the

crystal´s bandgap, it is possible to excite these local levels, and the emitted photons can propagate outside the crystal. Therefore, upon excitation, some crystals that would be transparent without defects become colored. Hence, such defects are called “color centers”[44].

Many color centers present optical properties suitable for applications in quantum technologies, such as single photon-emission (at room temperature in some cases), photostability, short lifetimes, and spin states that can be optically detected. Color centers emission spectra are composed of a sharp line due to the pure electronic transition between excited and ground state, called zero-phonon line (ZPL), and a broad line of phonon-assisted transitions due to the coupling with vibrational states of the atomic lattice.[44] For most applications in quantum information technologies, the ZPL is preferred as it is the main source of indistinguishable photons.[6] Hence, it is convenient to define the Debye–Waller factor, which is the proportion of the photons that are emitted in the ZPL.

Among many crystals that host color centers, diamond has promising features for applications in quantum information technologies. Due to its high bandgap (5.5 eV at 300 K)[6], it is transparent in a wide spectral range, hosting many bright color centers that can be individually addressed. Also, due to its mechanical properties, its color centers present high stability.[45] Of particular interest is the nitrogen-vacancy (NV) center. It is formed by a single substitutional nitrogen atom in the atomic lattice, adjacent to a carbon vacancy in the ⟨1,1,1⟩ crystallographic orientation, as depicted in the inset of Fig. 2.5b[45]. This color center has attracted significant attention since it is a stable single-photon emitter at room temperature. It has a spin state that can be optically prepared and read-out. Its charge state can be either neutral, so it is referred as NV^0, or negatively charged, referred as NV^-. The latter is the subject of more studies since its spin state can be optically read-out, which was not demonstrated yet for the neutral NV.[45] The emission spectra at room temperature of these color centers are depicted in Fig. 2.5b, where it is possible to observe the ZPLs at 575 nm for the NV^0 and at 637 nm for the NV^-, as well as their broad phonon sidebands. The quantum efficiency of the color centers is estimated as 0.7. [44]

The electronic structure of the NV^- consists of triplet ground ($^3A_2$) and excited (^3E) states, as well as intermediate singlet shelving states. At room temperature, there is a zero-field splitting between the $m_s = 0$ and $m_s \pm 1$ spin sub-levels of approximately 2.87 GHz in the ground state, and of 1.42 GHz in the excited state. Also, there is a

dependency of the fluorescence intensity of the color-center with the spin projection, as the $m_s = \pm 1$ have a higher probability to decay via the intermediate dark states, yielding a lower fluorescence counting when compared to the $m_s = 0$. In addition, there is a higher probability for the ^{1}A state to decay to the ^{3}A ground state in the $m_s = 0$ spin-sublevel[46]. Therefore, uppon excitation, the system is prepared at the $m_s = 0$ state. Since the ^{3}E → ^{3}A transition has a lifetime of approximately 10 ns, and the ^{1}E → ^{1}A of approximately 300 ns, the spin state can be optically read-out observing variations in the fluorescence intensity as the $m_s = 0$ yields a higher photon count, reaching contrasts of up to 30%,[46] which is the principle of optically detected magnetic resonance (ODMR). The schematics of the energy levels and decay rates are depicted in Fig. 2.5 a).

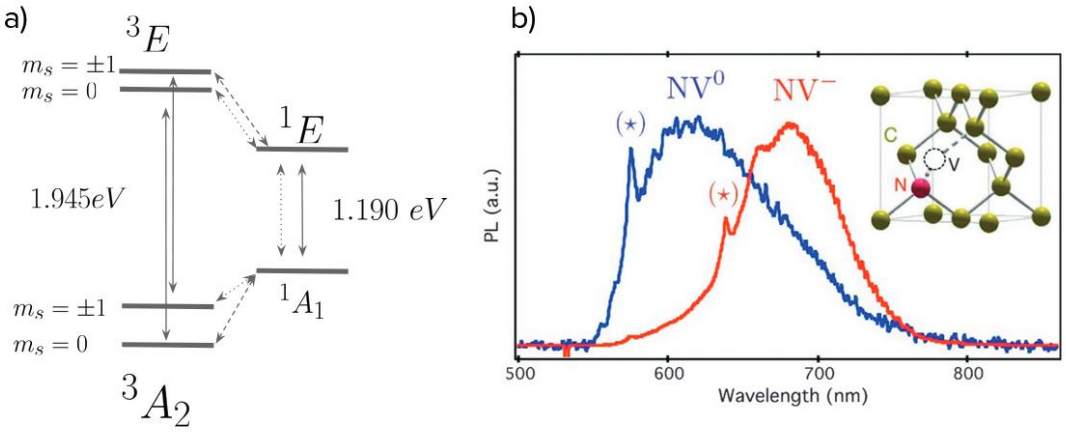

Figure 2.5 - a) Schematics of the electronic transitions of the NV^{-1} color center. The solid arrows denote the optical transitions. The dotted lines indicate the strong (---) and weak (…) non-radiative transitions. b) Emission spectra of the NV^0 (blue) and NV$^-$ (red) color centers. The inset displays a representation of the defect in the diamond lattice.
Source: Adapted from RONDIN[47]

One disadvantage of the NV$^-$ color center is its low Debye–Waller factor of approximately 3% at room temperature.[45] This means that most photons decay through phonon-assisted transitions (where part of the energy is lost as vibrations in the crystal lattice), losing coherence. One way to overcome this issue is to integrate the emitter into a photonic cavity. The cavity modes alter the density of states of the

system, diminishing the excited state lifetime and enhancing the emission of photons in resonance. This phenomenon is known as Purcell enhancement and can be modeled as[48]:

$$F = \xi \frac{3}{4\pi^2}\frac{Q}{V}\left(\frac{\lambda}{n}\right)^3 \tag{2.56}$$

$$\xi = \frac{\omega_c^2}{4Q^2(\omega_c-\omega_0)^2+\omega_c^2}\left(\frac{|\vec{\mu}.\vec{E}|}{|\mu||E_{max}|}\right)^2 \tag{2.57}$$

in which Q is the Q-factor of the cavity, V is the mode volume (Eq. 2.46), *n* is the refractive index of the medium, and ξ is a factor that accounts for the spatial and spectral overlap of the cavity field with the emitter field. In the case of exact resonance and perfect dipole alignment between emitter and cavity mode, $\xi = 1$ and the factor *F* can reach its maximum value.

2.5 Nonlinear optics and multiphoton absorption

In the linear regime, the polarization induced by an EM wave in a dielectric material is given by[49]:

$$\vec{P} = \epsilon_0 \chi^{(1)} \vec{E} \tag{2.58}$$

Equation (2.58) describes the relationship between the electric field of the EM wave and the polarization it induces in the material, which gives rise to everyday optical phenomena such as linear refraction and absorption.

When the electric field intensity of light is at the same order of the interatomic electric field (~10^8 V/cm), the movement of the bound charges cannot be approximated by a harmonic oscillator, as in the Drude-Lorentz model. Therefore, the polarization response of the medium will present a non-linear dependency on the electric field, which can be expressed as a power series[49]:

$$\vec{P}(t) = \epsilon_0 \sum_i \chi^{(i)} \vec{E}^i(t) \tag{2.59}$$

In this series, each term is responsible for particular phenomena in the light-matter interaction. The first term accounts for the linear interaction with light, leading to the well-known phenomena of refraction and linear absorption. The second term is responsible for phenomena such as second harmonic generation (where the output

light has twice the frequency of the input) and the sum of frequencies (where two photons combine to generate a new one at a different frequency). For this work, the third-order term is of particular interest:

$$P^{(3)}(t) = \epsilon_0 \chi^{(3)} E^3(t) \tag{2.60}$$

Considering the simple case of a linear polarized monochromatic electric field with harmonic temporal dependency $E(t) = E_0 cos\,(\omega t)$, propagating in isotropic medium, and applying it in Eq. 2.60, the third-order polarization becomes:

$$P^{(3)}(t) = \epsilon_0 \chi^{(3)} E_0^3 \left[\frac{1}{4} cos(3\omega t) + \frac{3}{4} cos(\omega t)\right] \tag{2.61}$$

The first term in the brackets accounts for the phenomenon of third harmonic generation. Using the relation of the intensity with the square modulus of the electric field given by Poynting theorem[41]:

$$I = \frac{1}{2} n_0 \epsilon_0 c E_0^2 \tag{2.62}$$

the second term can be rewritten as:

$$P^{,(3)}(t) = I \frac{3}{2} \frac{1}{n_0 \epsilon_0 c} \epsilon_0 \chi^{(3)} E_0(t) \tag{2.63}$$

This component has the same functional form of the first-order polarizability, but with an explicit dependency on the intensity of the electric field. Hence, we can define the refractive index of the material as a sum of a linear and a non-linear component:

$$n = n_0 + n_2 I \tag{2.64}$$

The real part of n_2 will be responsible for the Kerr effect, which is a dependency of the refractive index of the medium with the intensity of the incident light.[49] The imaginary part will be responsible for the non-linear absorption of light, so the absorption coefficient is written as:

$$\alpha(I) = \alpha_0 + \beta I \tag{2.65}$$

Taking the derivative of the Beer-Lambert law in a spectral region where there is no linear absorption ($\alpha_0 = 0$), we have[50]:

$$\frac{dI(z)}{dz} = -\beta I^2(z) \tag{2.66}$$

Therefore, the absorption rate for the 2PA depends on the square of the pump intensity. The non-linear absorption coefficient (β) can be related to the 2PA cross-section as[50]:

$$\sigma_{2p} = \frac{\beta h\nu}{N} \tag{2.67}$$

The unit for the 2PP cross-section is the GM, a reference to the Nobel-laureate physicist Maria Goppert-Mayer, who first predicted the 2PA phenomenon. The GM units are $10^{-50} cm^4.s.photon^{-1}$ [49].

In a quantum mechanics approach, the nonlinear absorption can be interpreted as a multiphoton absorption, where two photons with individual energies not high enough to promote an electronic transition are absorbed in a single quantum act, such that their added energies is sufficient to promote the transition, as depicted in Fig. 2.6.

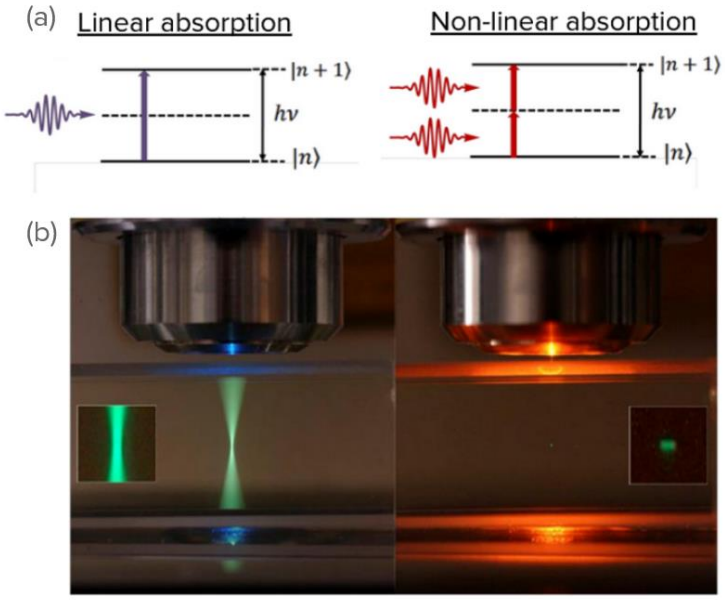

Figure 2.6 - a) Schematics of the linear absorption, where one single photon promotes an electronic transition, and the 2PA, where two photons with half the required energy to promote the transition act together to promote an electron to the excited state. b) On the left, there is an example of linear absorption, where the induced fluorescence by the pump laser can be observed in all the light path. On the right, there is an example of non-linear absorption, where the fluorescence is observed only at the focal point, and the pump photons have lower energy than the fluorescence photons.
Source: Adapted from TOMAZIO[44]

The probability for the 2PA to occur is much lower than the linear absorption, and can only be observed at high intensities of the EM field. In fact, the 2PA cross-section of most molecules is on the order of GM. We can estimate the order of magnitude of β (unit of $cm.\frac{s}{J}$) for a transition with an energy equivalent of a photon with a wavelength of $1\mu m$ ($h\nu \approx 10^{-19}\,J$), and with a concentration of absorbers (N) on the order of 1 Mol/L:

$$\beta = 10^{20}\left(\frac{photon}{cm^3}\right)10^{-50}(cm^4.s.photon^{-1})10^{19}\left(\frac{1}{J}\right) = 10^{-11}cm.\frac{s}{J}$$

Hence, intensities in the order of $10^8\,\frac{W}{cm^2}$ are necessary for the nonlinear process to become comparable to the linear one. The first observation of the 2PA phenomenon was in 1961, one year after the first demonstration of a laser source.[38]

2.6 Two-photon polymerization

Two-photon polymerization is a versatile DLW technique that exploits the non-linear absorption of a photoresist to fabricate 3D structures with sub-wavelength resolution. The photoresist, a light-sensitive material that hardens when exposed to specific wavelengths, is a mixture of monomers (building blocks for the polymer) and a photoinitiator. When the photoinitiator absorbs light, it triggers the polymerization process by forming free radicals that break the double bonds in the monomers, generating active centers for the polymer chain formation[50]. This process is illustrated in Fig. 2.7.

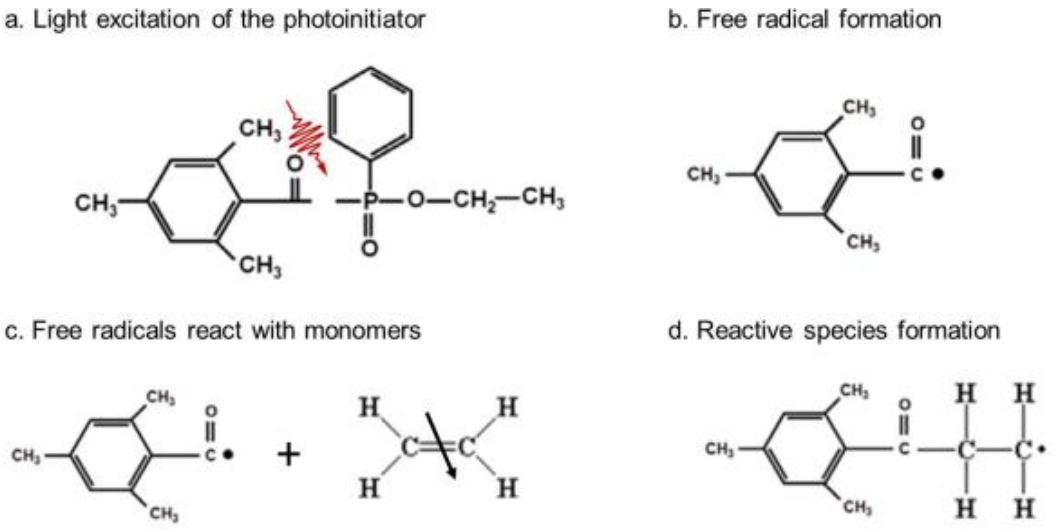

Figure 2.7 - Schematics of the photopolymerization process.
Source: Adapted from TOMAZIO[38]

When the photoresist is irradiated with a pulsed laser focused by a microscope objective, in a spectral region where the photoinitiator will only present nonlinear absorption, it is possible to adjust the laser intensity so that the 2PA will occur only in the focus, hence limiting the polymerization process to a small volume in the photoresist.

The smallest polymerized structure is called a voxel, and its size and shape are determined by the laser properties and objective numerical aperture (NA). Given the intensity of a Gaussian beam[41]:

$$I(r,z) = I_0 \left(\frac{w_0}{w(z)}\right)^2 e^{-2\left(\frac{r}{w(z)}\right)^2} \tag{2.68}$$

where $w_0$is the waist at the focus, defined as the distance from the center in which the intensity decays by a factor of e^{-1}, I_0 is the peak intensity, *r* and z are the radial and progation coordinates, and:

$$w(z) = w_0^2 \left[1 + \left(\frac{z}{z_0}\right)^2\right]^{1/2} \tag{2.69}$$

with the definition[41]:

$$z_0 = \frac{2\pi w_0^2}{\lambda} \tag{2.70}$$

We can write w_0 as a function of the objective NA[50]:

$$w_0 = \frac{\lambda}{\pi NA}\sqrt{n^2 - NA^2} \tag{2.71}$$

where n is the refractive index of the medium, and λ the wavelength.

Since the nonlinear process will occur only above a given intensity threshold (I_{th}), and accounting that the two-photon absorption is, in fact, proportional to the square of the intensity (Eq. 2.66), we can estimate the radius (R_v) and length (L_v) of a voxel from Eq. 2.68 as:

$$I^2(r, z = 0) = I_{tsh}^2 = I_0^2 e^{-4\left(\frac{R_v}{w_0}\right)^2} \tag{2.72}$$

$$R_v = \frac{w0}{2}\sqrt{ln\frac{I_0}{I_{tsh}}} \tag{2.73}$$

and:

$$I(r = 0, z) = I_{tsh}^2 = I_0^2\left(\frac{w_0^2}{w(z)^2}\right)^2 = I_0^2\frac{1}{\left[1+\left(\frac{L_v}{2z_0}\right)^2\right]^2} \tag{2.74}$$

$$L_v = \frac{4\pi w_0^2}{\lambda}\sqrt{\left(\frac{I_0}{I_{th}}\right)^{\frac{1}{2}} - 1} \tag{2.75}$$

Hence, one can note that L_v has a quadratic dependency on w_0, while R_v has a linear dependency. Also, the increase of L_v with the ratio $\left(\frac{I_0}{I_{tsh}}\right)$ is slower as compared to R_v.

For a microscope objective of NA = 0.25, it is possible to estimate the pixel size as a function of the proportion $\frac{I_0}{I_{tsh}}$. The results are presented in Fig. 2.8. For a reasonable proportion of 1.25, the voxel has a diameter of approximately 0.2 µm and a height of 5 µm, considering a 0.25 NA objective and laser excitation at 800 nm.

It is possible to relate I_0 with the laser parameters pulse duration and repetition rate, and the mean power obtained by a power meter. Considering a beam with a Gaussian profile, its power is given by[51]:

$$P = P_{peak} e^{-4ln2\left(\frac{t}{\tau_p}\right)^2} J/s \tag{2.76}$$

The energy per pulse can be estimated as:

$$E_p = \frac{\overline{p}}{f} \tag{2.77}$$

where f is the laser repetition rate and $\overline{p}$ is the average power, measured by a power meter.

Since $E_p = \int Pdt$, the peak power as a function of the temporal width is:

$$P_{peak}(\tau_p, f) = \frac{\overline{p}}{\tau_p f}\sqrt{\frac{4ln2}{\pi}} \tag{2.78}$$

Finally, the peak intensity can be approximated considering a circular area of radius w_0:

$$I_0 = \frac{P_{peak}}{\pi w_0^2} \tag{2.79}$$

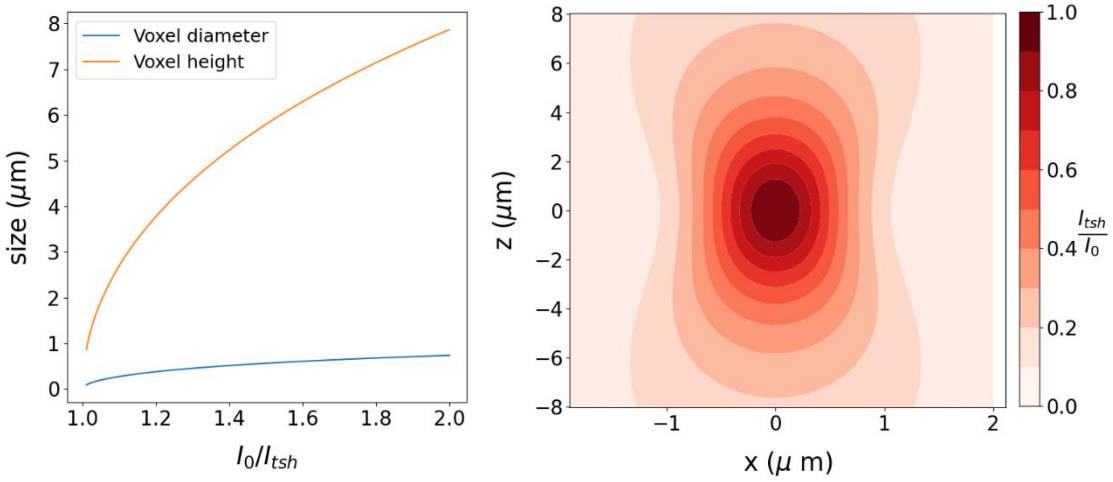

Figure 2.8 - a) Dependency of the voxel diameter (blue) and height (orange) with the ratio of the threshold intensity and excitation laser intensity. b) Voxel cut in the (x,z) plan as a function of I_0.
Source: By the author

3 Experimental methods

3.1 Two-photon polymerization setup

The two-photon polymerization setup consists of a Ti:Sapphire oscillator delivering 100 fs pulses centered at 780 nm, at an 86 MHz repetition rate. The laser is sent to a half-wave plate and a polarizer to control the intensity, then to a pair of galvanometric mirrors, and finally to a 0.25 NA microscope objective that focuses the beam into the sample. To perform the fabrication, a software controls the galvanometric mirrors, that define the *x* and *y* positions of the beam, and a motorized stage sets the *z* position of the sample.[34–37] A schematic of the 2PP setup is depicted in Fig. 3.1.

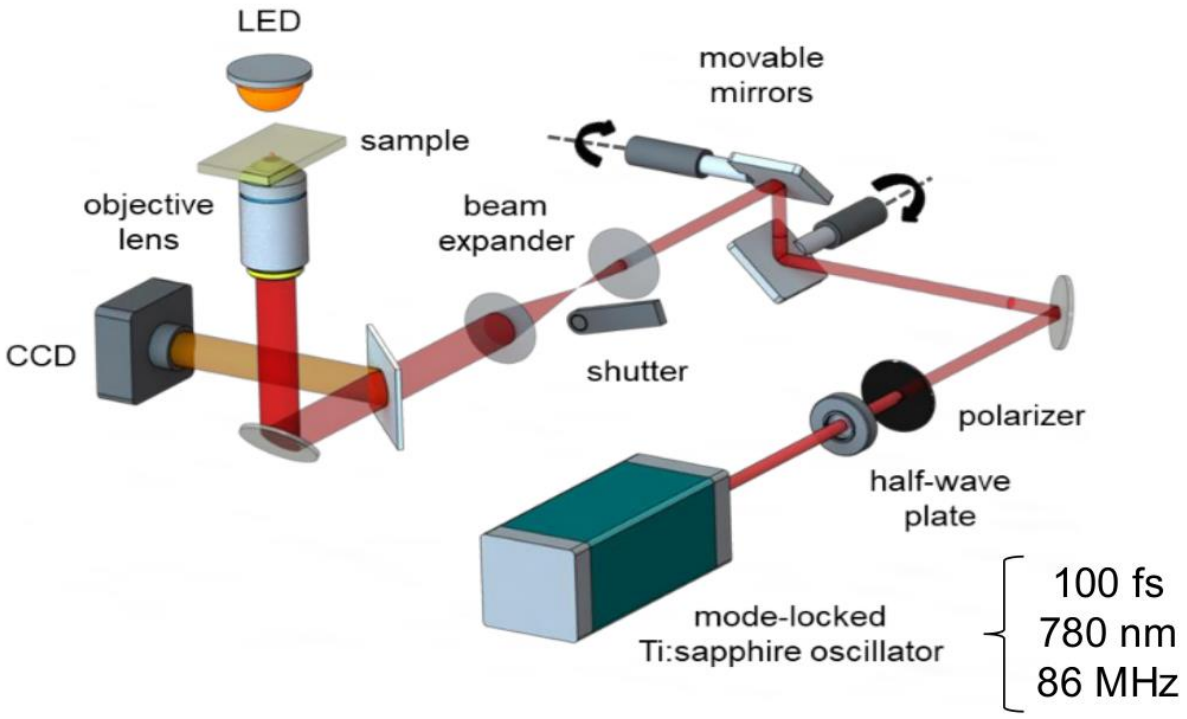

Figure 3.1 - Schematic of the setup used to fabricate the structures via 2PP.
Source: TOMAZIO[29]

3.2 Fabrication methodology

In this work, we leverage a fabrication method demonstrated in previous works.[38] This method involves building structures layer-by-layer using a vectorization strategy consisting of a superposition of concentric circles. This approach has been shown to be effective in achieving low surface roughness and high Q-factors for cylindrical structures.

The free parameters for the fabrication are the number of concentric circles, the final radius of a given layer, the radial increment of each circle, the number of layers in *z*-direction, and the step between layers. The first parameters determine the final radius of the structures, voxel (volumetric pixel) overlap in the radial direction, and the wall thickness for the cylindrical cavity. For instance, if we configure the final radius to be 30 μm, the number of concentric circles to be 5, and the radial increment to be 1 μm, each layer will result in a hollow cylinder with an outer radius of 30 μm and wall thickness of approximately 5 μm.

The number of layers in the *z*-direction controls the height of the structure, and the step parameter defines the amount of voxel overlap, which is crucial to keep the resonator wall smooth. Figure 3.2 shows an example with different overlapping values. One can notice that for exceedingly large steps in the *z*-direction, the voxels will not overlap properly, resulting in rough surfaces that can scatter light and introduce optical losses. For an objective of 0.25 NA, it was experimentally observed that a step of 5 μm would provide a good voxel overlap, and hence smooth walls.[38].

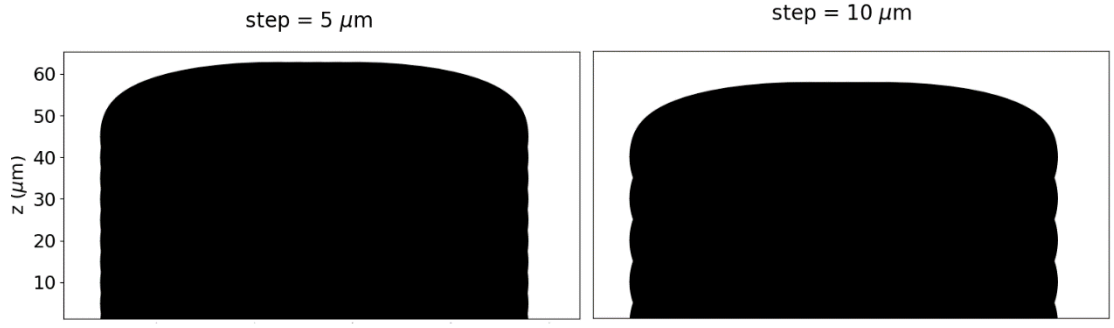

Figure 3.2 - Representation of a wall of a cylindrical structure in the *z*-direction, considering two different z-step parameter values. It is possible to note that a non-ideal parameter leads to a wall with high surface roughness, which can scatter light and introduce optical losses.

Source: By the author

3.3 Photoresist preparation

The photoresist consists in a mixture of dipentaerythritol pentaacrylate (SR399 – Sartomer®) and tris(2-hydroxy ethyl)isocyanurate tryacrylate (SR368 – Sartomer®) monomers, at the proportion of 90/10, and 3% in excess weight of Lucirin TPO-L as the photoinitiator. The former, due to its long chains, provides flexibility to the final structures and reduces the inherent shrinkage of the fabrication process. The latter confers rigidity.[50] The proportion of monomers has been optimized in previous works[38] for an optimum compromise between rigid structures and low shrinkage during the fabrication process.

To dope the photoresist, a solution of nanodiamonds in deionized water in a concentration of 1 mg/mL is incorporated into the monomers and photoinitiator, and the whole mixture is submitted to magnetic stirring at 50 °C until homogenization and complete evaporation of the deionized water. The mean diameter of the nanodiamonds is 40 nm, as informed by the vendor (Adámas Nanotechnologies).[52]

To calculate the quantities of dopant to add in the mixture, we first determined the desired nanodiamond concentration in weight percent (wt%). Then, we weighed a drop of the photoinitiator, and the weight of each monomer is then determined to obtain a 90/10 SR399/SR368 with 3 wt% of photoinitiator. The weights are defined as:

$$w_t = \frac{w_l}{0.03} \tag{3.1}$$

$$w_{399} = (w_t - w_l)0.1 \tag{3.2}$$

$$w_{368} = (w_t - w_l)0.9 \tag{3.3}$$

where w_t, w_l, w_{399} and w_{368} are, respectively, the total, Lucirin, SR399 and SR368 weights.

Subsequently, to obtain a given *P* proportion of nanodiamonds in wt%, the volume of solution (V) to be added to the mixture is defined as:

$$V = w_t \left(\frac{100}{P} - 1\right)^{-1} \tag{3.4}$$

In this definition, 100 g of doped resist at a concentration of 1 wt% will consist of 1g of nanodiamonds and 99g of pure resist.

3.4 Tapered optical fiber preparation and coupling system.

To analyze the quality factor (Q factor) of the structures, a 2 μm diameter tapered optical fiber is used to couple light from a tunable laser source into the resonators via evanescent wave.

For the tapering optical fiber fabrication, we follow the modeling proposed in ref.[53], where we slowly stretch an optical fiber while keeping an approximately constant heat region. In this model, we assume that the total mass of the fiber is conserved. Considering an initial hot length L_0 and that the fiber is stretched by a distance *x*, we define the final length of the taper as a constant region with size l_w, and two transition regions with length z_0 at each side of the constant zone. A schematic of this model is shown in Fig. 3.3.

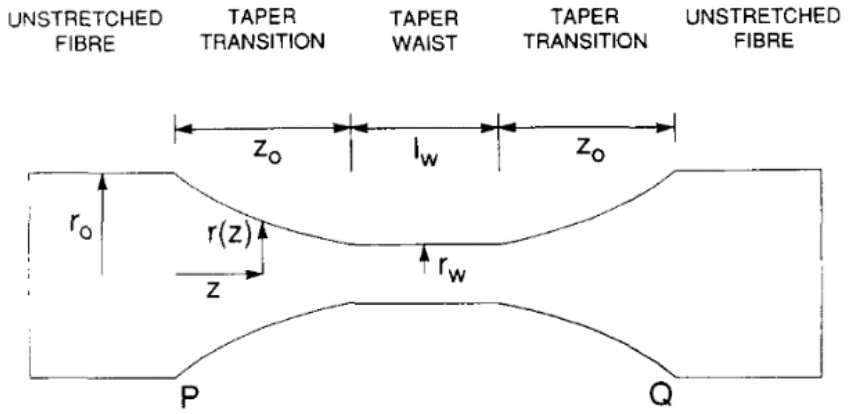

Figure 3. 3 - Schematics of the tapered optical fiber model. r_w is the taper radius, and r_0 the initial fiber radius.
Source: BIRKS[53]

Considering a constant heat zone (L_0), we have $L = L_0$ and $z_0 = x/2$. In this case, the shape of the transition region is given by[53]:

$$r(z) = r_0 e^{-\frac{z}{L_0}} \tag{3.5}$$

where r_0 is the length of the hot zone, and the final size of the tapered fiber is[53]:

$$r(z = z_0) = r_0 e^{-\frac{x}{2L_0}} \tag{3.6}$$

Hence, the final radius is a function of the hot zone length and the total stretched distance.

The setup which implements this process consists of an oscillating flame, that creates an approximate homogeneous heat zone, and a steeper that is responsible for driving a pair of fiber supports apart, as depicted in Fig. 3.4. The free parameters are the total distance in which the fiber is stretched (*x*), and the length of the flame brushing (L_0). With this method, tapers with diameters on the order of 500 nm can be produced, as shown in Fig. 3.4 b.

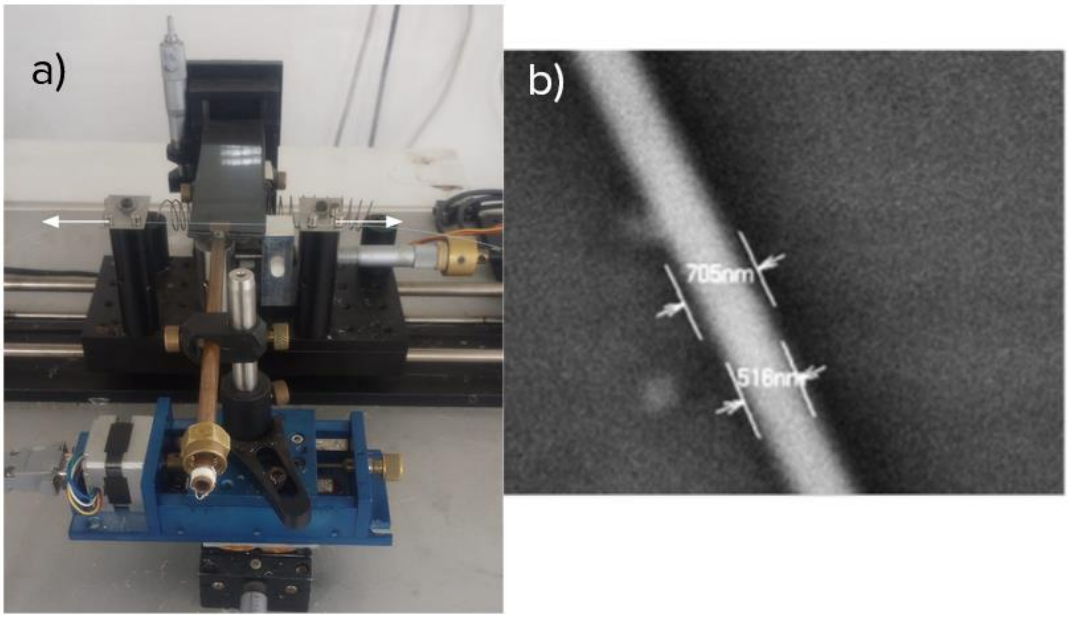

Figure 3.4 - (a) Picture of the setup used to fabricate tapered optical fibers. (b) SEM micrograph of a fiber with radius below 1 µm.
Source: By the author

To promote the cavity-taper coupling, the setup depicted in Fig. 3.5 was assembled. This setup consists of a 3D stage, where the sample is positioned so that the structures are parallel to the floor. Another 3D stage is assembled over a rotatable stage, to control the position of the fiber and keep it aligned with the structures, so it

does not hit the substrate before reaching the structure. The coupling procedure is imaged in real time with a stereo microscope and a CMOS camera. Images of this process are shown in Fig. 3.5(c).

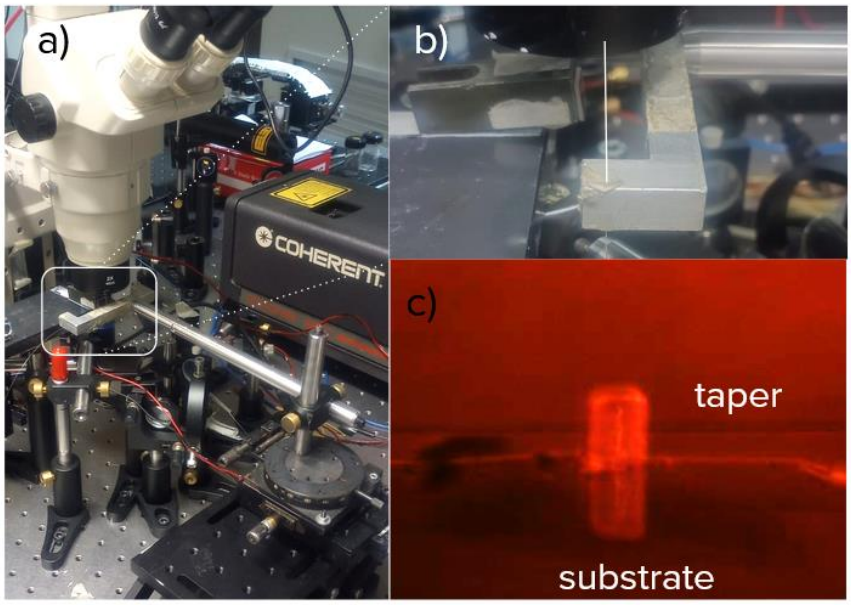

Figure 3.5 - (a) Picture of the coupling system. (b) Zoom at the tapered optical fiber and sample. (c) Image of the fiber coupled structure.
Source: By the author

The optical fiber is excited by a tunable infrared (IR) laser source, with resolution of 0.005 nm. Before reaching the tapered region, the fiber passes through an optical fiber polarizer, that induces birefringence by stress. After interacting with the structure, the transmitted signal is directed to a photodiode. The spectrum is obtained by sweeping the frequency of the tunable laser source, at first in a normalization run, where the fiber is not in contact with the resonator, obtaining a $I_0(\lambda)$ spectrum. Then, the resonator is put in contact with the tapered optical fiber, and another sweep is made to obtain a coupled transmittance spectrum $I_C(\lambda)$. Finally, the transmittance is defined as $I_C \backslash I_0$. The data acquisition process is automated.

The light coupled is seen as a dip in the fiber transmitted spectrum, and the FWHM at each resonance is estimated through a Lorentzian fit:

$$T(\lambda) = \frac{I_0}{\left[1+\frac{4(\lambda-\lambda_0)^2}{\Delta\lambda^2}\right]} \tag{3.7}$$

Experimentally, some resonances are not symmetric, hence the $\Delta\lambda$ definition is given as follows. [37,54]

$$\Delta\lambda = \frac{2\Delta\lambda_0}{1+e^{\alpha(\lambda-\lambda_0)}} \tag{3.8}$$

where α is the asymmetric parameter, and $\Delta\lambda_0$ is the FWHM of a symmetric Lorentzian. The asymmetries can arise from two main factors: spectral position changes caused by rapid resonator heating (faster than the scan speed) or Fano resonances induced by the interaction with the tapered optical fiber.

3.5 Confocal spectroscopy setup

To collect and analyze the nanodiamonds emission, a confocal fluorescence spectroscopy setup was assembled. The setup consists of a microscope objective that is used to both excite the sample with a diode laser emitting at 532 nm and collect its fluorescence. A dichroic mirror is used to separate the excitation light from the fluorescence, which is then sent through a flip mirror. When the flip mirror is lifted, the signal is directed to a CMOS camera, to obtain a real-time image of the sample. Before reaching the camera, a pinhole is placed at the focus of the signal to cut out-of-focus light and establish a confocal configuration, achieving a better spatial resolution. To observe the nanodiamonds fluorescence, it is necessary to keep the integration time of the camera around 100 ms. A picture of the system is presented in Fig. 3.6

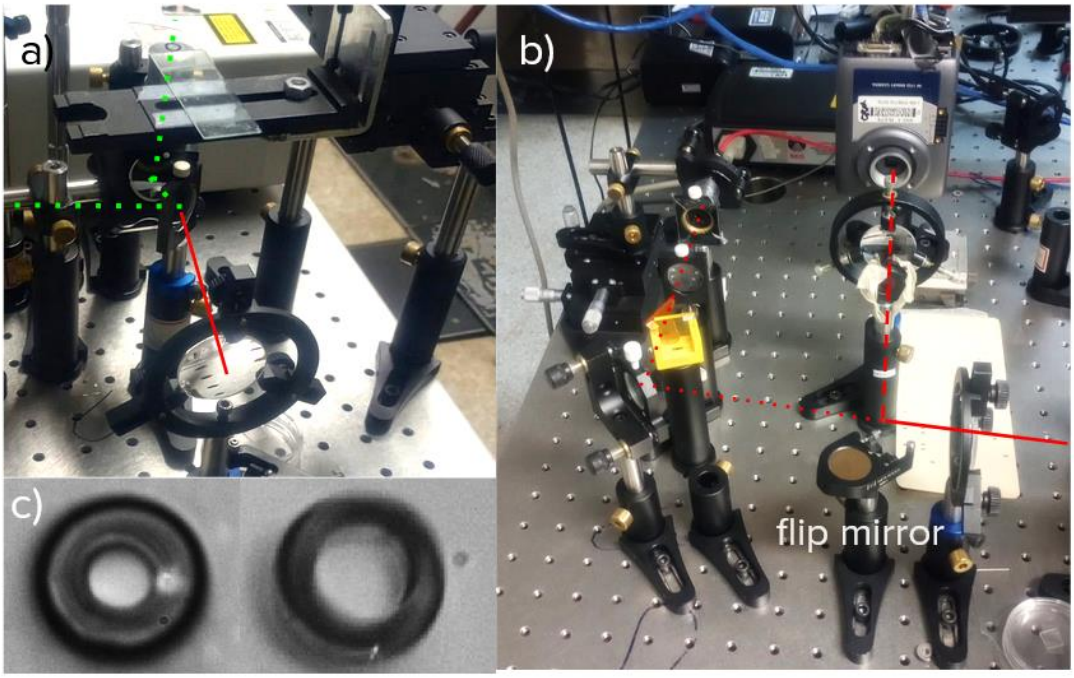

Figure 3.6 - (a) Picture of the laser path (represented in green) to the objective in the confocal spectroscopy system. (b) Picture of the signal path to the CMOS camera (right) and to the optical fiber (left). (c) Typical images taken by the system, where the nanodiamond fluorescence can be seen as a small white spot.
Source: By the author

When a fluorescent spot is located, the flip mirror is lowered, so the signal is collimated and focused on an optical fiber via a microscope objective. The optical fiber is either connected to a spectrometer, for fast analysis, or to a monochromator (1800 lines/mm grating), for higher spectral resolution. In the latter, the spectrally separated light is sent to a photomultiplier tube. A chopper and lock-in amplifier are used to increase the signal to noise ratio. A schematic of this setup is presented in Fig. 3.7.

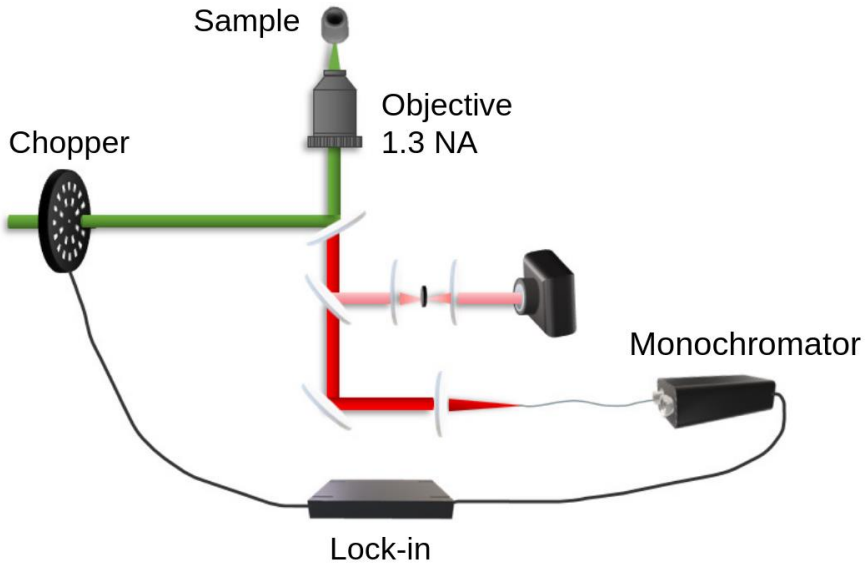

Figure 3.7 - Schematics of the setup used to localize the nanodiamonds and measure the fluorescence of the NV color centers in the microresonators.
Source: By the author

One important consideration is the integration time used in the lock-in amplifier. As can be observed in Fig. 3.8, for a given lock-in integration time, the signal takes about 4 times this integration time to fully decay. Therefore, to avoid crosstalk between adjacent measurements and ensure a spectrum with high resolution, after changing the wavelength at the monochromator it is necessary to wait for this decay time before reading the lock-in signal.

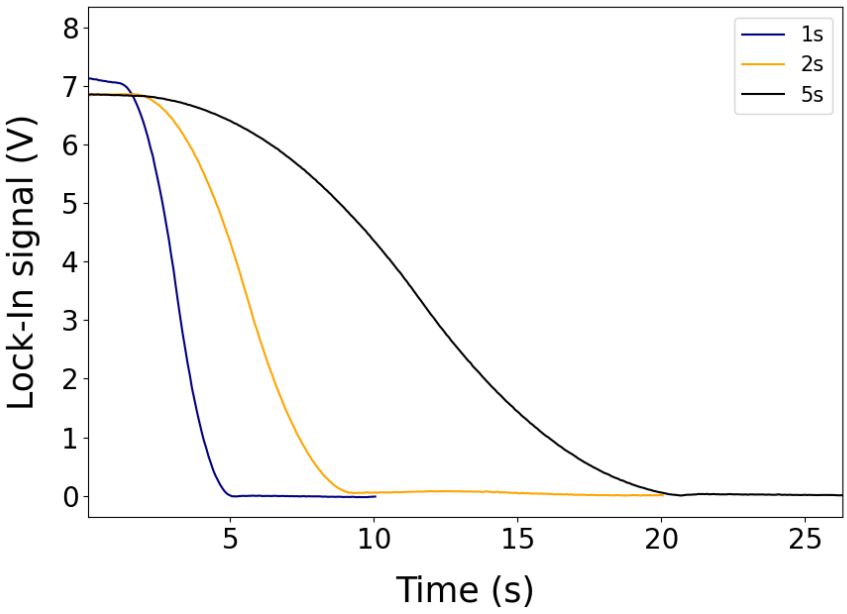

Figure 3.8 - Decay time of the lock-in signal for different integration times.
Source: By the author

Another important issue is to compensate the transmission of the dichroic mirror. Since it is a thin film dielectric mirror, its transmittance spectrum presents a characteristic modulation, as shown in the inset of Fig. 3.9. As one can observe, the raw signal will have distortions due to the mirror transmittance, that must be compensated to obtain the real signal.

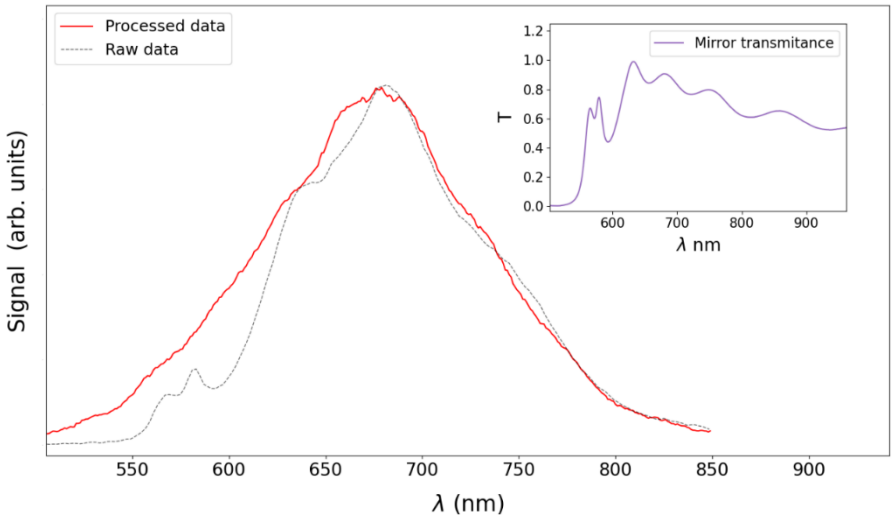

Figure 3.9 - In black, the raw spectrum presenting distortions due to the transmittance of the dichroic mirror (inset). In red, the processed data that compensates for the mirror transmittance.
Source: By the author

The data acquisition process is automated; thus, the monochromator sweeps the fluorescence at a given spectral region, with a predetermined step, and the signal from the lock-in amplifier is collected after the appropriate time as discussed above, and compensated by the mirrors transmittance.

To further confirm the presence of the nanodiamonds in discrete positions in the structures, Raman and photoluminescence measurements were carried out with a LabRAM equipment, using 532 nm and 633 nm excitation wavelengths, and a 100 x objective to focus the laser. Also, laser scanning microscope (LSM) measurements were carried out to map the nanodiamonds in a broad area.

4 Nanodiamond doped structures fabricated via Two-Photon Polymerization

4.1 Doped photoresist Characterization

Different concentrations of doped photoresist were prepared. Figure 4.1 shows the visual characteristics for different concentrations of UV-cured photoresist, where it is possible to observe high scattering for high concentrations.

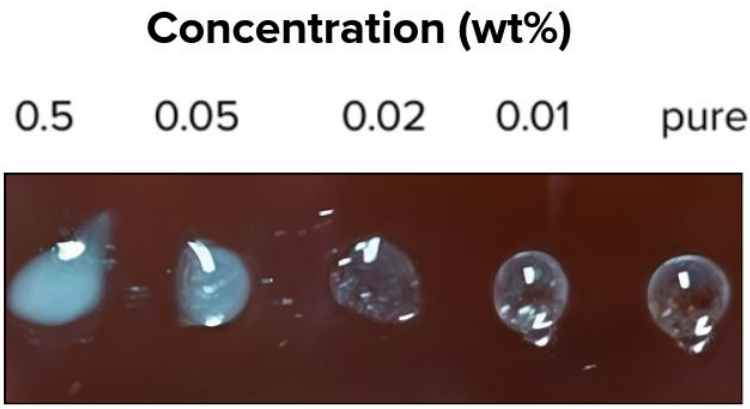

Figure 4.1 – Drop of UV cured photoresist doped with different concentrations.
Source: By the author

Thereafter, the fluorescence of the UV-cured doped photoresist was analyzed for different nanodiamond concentrations. A reference spectrum was obtained by analyzing a drop of the nanodiamond solution on a substrate. It is possible to observe in Fig 4.2 that the emission spectrum of the nanodiamonds in bulk photoresist overlaps with the emission spectrum of the residual photoinitiator, so only at high concentrations (0.5 wt%) can the characteristic NV spectrum be distinguished. Although this is an issue for bulk photoresist, it is less relevant for the microstructures, as the amount of polymer irradiated is lower than that irradiated from the bulk. Furthermore, due to the nonlinear nature of the 2PP process, the photoinitiator in the fabricated microstructures is expected to be consumed more efficiently than in the UV-cured bulk photoresist. To improve the nanodiamond signal, a high numerical aperture objective is used in conjunction with a pinhole placed at the focal point before coupling the fluorescence to the optical fiber. This configuration minimizes the out-of-focus signal, which is primarily unwanted photoresist fluorescence.

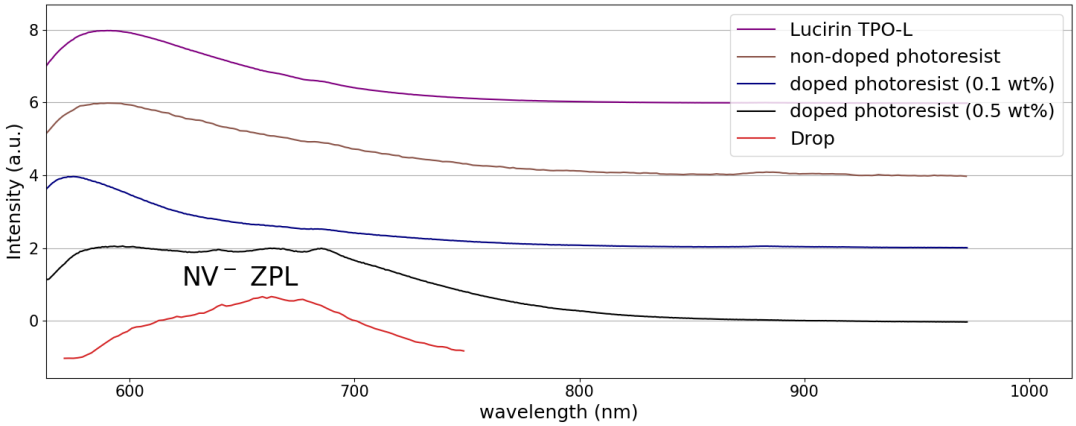

Figure 4.2 - Fluorescence spectrum of the photoinitiator, bulk resist for different concentrations and nanodiamonds dispersed in a glass substrate.
Source: By the author

As a reference, Fig 4.3 shows the emission and absorption spectrum of the nanodiamonds solution, as given by the vendor. [52]

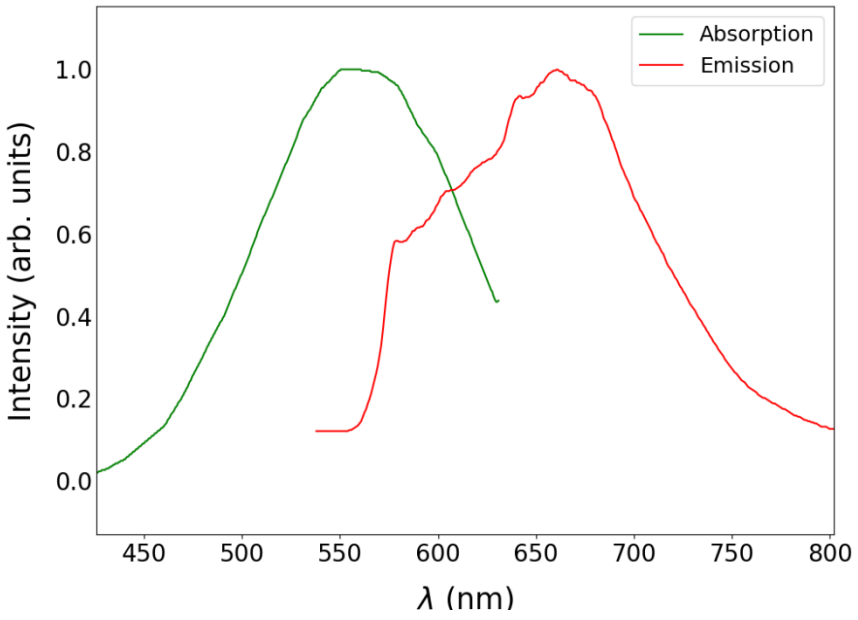

Figure 4.3 - Absorption (green) and emission (red) spectrum of the nanodiamonds, as reported in reference[52].
Source: By the author

The losses induced by the presence of the nanodiamonds were investigated with absorbance measurements, carried out in 0.5 mm thickness films of UV-cured photoresist, and the absorption coefficient was determined through Beer-Lambert law. In the results presented in Fig. 4.4, one can note that the doped photoresists have a general offset compared to the pure one, showing no features of the absorption of the NV color center (Fig. 4.3). Therefore, the losses are attributed mainly to scattering of the nanoparticles.

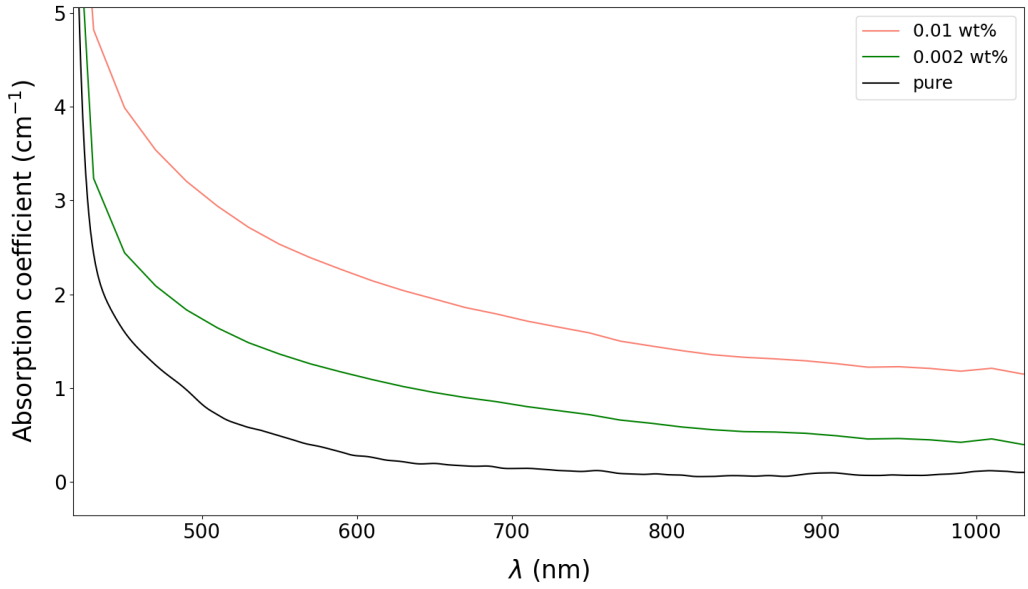

Figure 4.4 - Absorption coefficient of the pure photoresist (orange line) and of the photoresist doped with nanodiamonds at the proportion of 0.02 wt% and 0.002 wt%.
Source: By the author

To investigate the feasibility of the fabrication with the doped photoresist, we attempted to produce cubic structures with different concentrations, and analyze each structure through SEM micrographies, and investigate the presence of nanodiamonds through Raman and confocal spectroscopy. As can be seen in Fig. 4.5, for concentrations of nanodiamonds above 0.5 wt%, the structures cannot be fabricated. For lower concentrations, although the 2PP fabrication is achieved, there is a high presence of agglomerates. The presence of NV centers within the agglomerates is confirmed using both fluorescence spectroscopy and Raman spectroscopy, as detailed in Fig. 4.5.

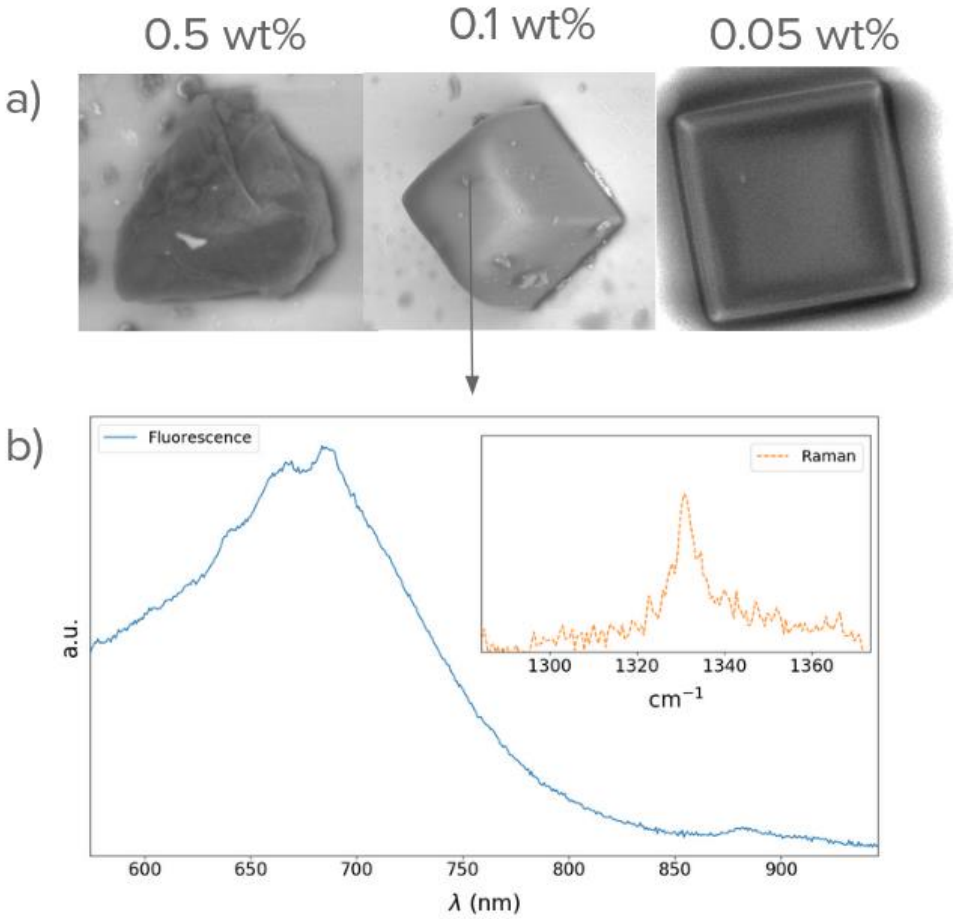

Figure 4.5 - (a) Cubes fabricated with doped photoresist with different concentrations. (b) Photoluminescence and Raman (inset) spectrum of an agglomerate, where it is possible to observe the NV PL spectrum and the Raman line of the pristine diamond lattice around 1333 cm^{-1}.
Source: By the author

To estimate the nanodiamond distribution in the resist, a film doped at 0.002 wt% was fabricated via spin-coating. The film was irradiated with green light illumination focused by a 40x objective in a confocal microscope, and the signal was integrated for 60 seconds after passing through a low-pass filter, to form the image presented in Fig. 4.6(a), where several fluorescent spots are observed. Additionally, ODMR measurements at zero field were carried out in the same film, where the typical contrast centered at 2.87 GHz resonance can be seen in Fig. 4.6(b). The two dips, separated by 16 MHz, indicate that the degenerate state of the $m_s \pm 1$ spin projections are lifted, which can be attributed to strain in the diamond lattice. This splitting agrees with results obtained in the literature for nanodiamonds,[55] and its value is lower than

those reported for bulk diamond processed by femtosecond-laser sources,[46] indicating that the polymeric matrix is not inducing additional strain or surface effects into the NV centers.

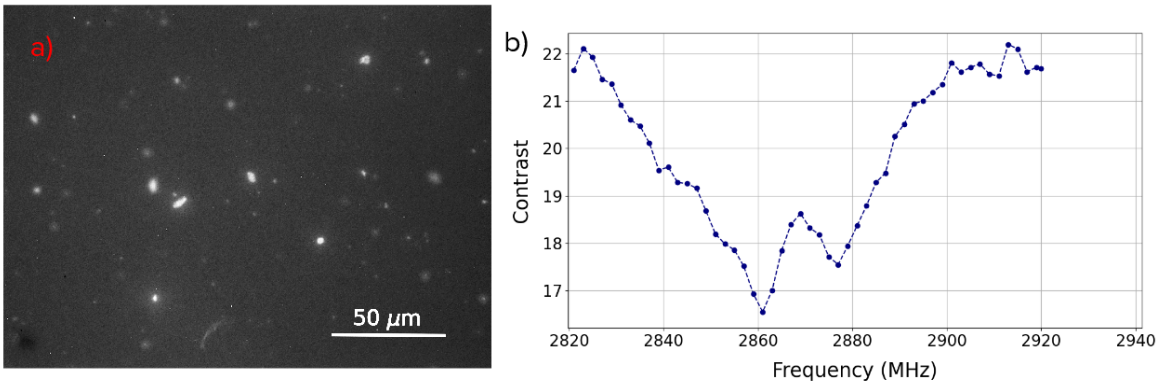

Figure 4.6 - (a) Fluorescence image of a film of photoresist obtained under green light illumination. (b) ODMR spectrum at zero-field for the same film.
Source: By the author

4.2 Cylindrical resonators

Firstly, the quality of the resonators as a function of the concentration of nanodiamonds in the photoresist was investigated. Scanning electron microscopy (SEM) was used to analyze the fabricated resonators qualitatively. As discussed before, for concentrations of 0.5 wt%, the fabrication via 2PP was not achieved. For concentrations ranging from 0.01 wt% to 0.05 wt%, fabrication is possible, but the final structures are not well formed and present many agglomerates, which can compromise their performance for applications in photonics and quantum optics. For proportions lower than 0.01 wt%, the fabrication of clean and well-formed cylindrical structures was achieved. Some of these structures, with different proportions of dopants, are presented in Fig. 4.7.

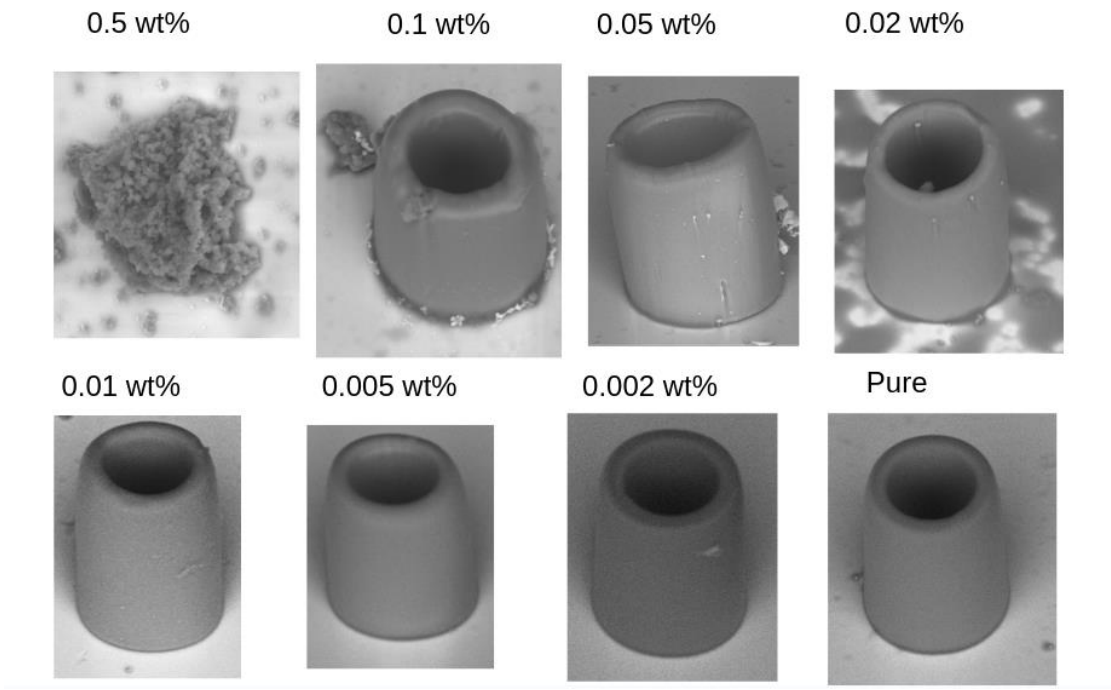

Figure 4.7 - SEM micrography of cylindrical microresonators fabricated with photoresists doped with different proportions of nanodiamonds.
Source: By the author

To further confirm the presence of nanodiamonds in specific locations in the resonators, Raman spectroscopy measurements were carried out in a previously characterized resonator, doped with a concentration of 0.002 wt%. The excitation was set at 633 nm, to avoid the fluorescence of the NV centers. As depicted in Fig. 4.8, the measurements were carried out in two different locations, one where a fluorescence spot was previously found with the confocal setup presented in Chapter 3.5, and the other in a neighboring location, where no fluorescence was detected (blue line – Fig.4.8(a)). Figure 4.8(b) illustrates the position in which each Raman spectrum was measured. As seen in Fig. 4.8(a), the Raman spectra are similar for both points (due to polymer bands) except for a small band at 1332 cm^{-1} (magnified in the inset of Fig. 4.8(a)), characteristic of the pristine diamond atomic lattice,[56] which is only visible at the point where the fluorescence was previously found.

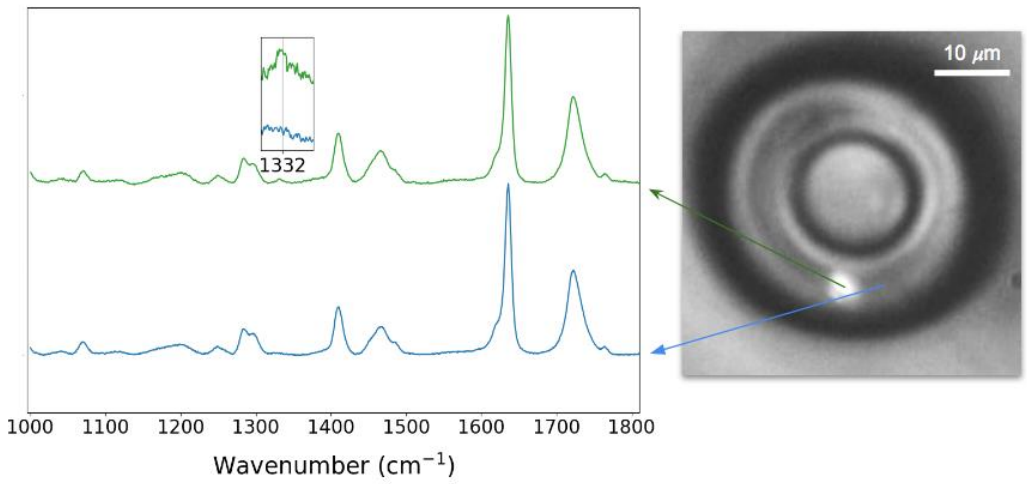

Figure 4.8 - (a) Raman spectra for two different points in a resonator doped with 0.002 wt% of nanodiamonds. The inset displays a zoom-in of the diamond peak at 1332 cm^{-1}, only in the point where the fluorescence was found. (b) Image from the setup depicted in Fig.9, while the fluorescent nanodiamond is excited with a 532 nm laser source focused with a 100 × microscope objective, illustrating the positions in which the Raman spectra were measured.
Source: By the author

To analyze the performance of these structures as resonant cavities, their Q factor was studied in the near-infrared region using a tapered optical fiber and a tunable laser source, as described in chapter 3.4. In Fig.4.9(a), one can observe a broadening in the WGM resonances of the cylindrical resonators when the concentration of dopant is increased, as well as a decrease in the number of visible resonances.

Figure 4.9(b) shows the dependence of the average Q factor on the nanodiamond content, considering the five most intense resonances for each concentration, where a rapid decay of the Q factor with the increase of the dopant in the photoresist can be seen. Hence, for high concentrations, the Q factor may be too low for most applications. On the other hand, for concentrations of 0.005 wt% and 0.002 wt%, it is possible to achieve a Q factor that is less than one order of magnitude lower than for the non-doped ones, and close to the theoretical maximum value estimated for this photoresist, around 10^5 [37], as shown by the inset in Fig. 4.9(a).

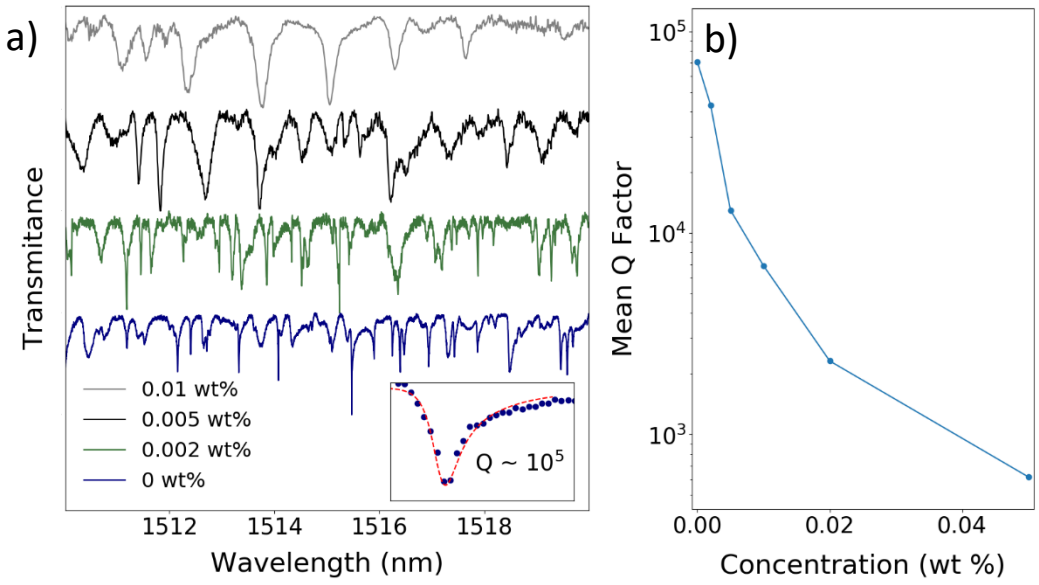

Figure 4.9 - (a) Spectra of resonances for resonators doped with different nanodiamond concentrations. In the inset, an example of a resonance modeled as an asymmetric Lorentzian function to estimate its Q factor. (b) Mean Q factor as a function of dopant concentration.
Source: By the author

To estimate the position and number of emitters in the resonators and collect their emission spectra, the confocal setup depicted in Chapter 3.5 was used to sweep the structures and map the positions where the NV color center fluorescence was located. For concentrations of 0.01 wt% and above, points with fluorescent spots can be easily found in many locations in the structure's volume. For concentrations of 0.005 wt% and below, almost all studied structures present one to three emitters. It is worth noting that, according to the nanodiamonds vendor, the NV color centers are present in about 70% of the nanoparticles.[52] Figure 4.9 shows an example of a structure doped with a concentration of 0.002 wt%, where three fluorescent points were located (Fig. 4.9(a)), as well as one fluorescence spectrum (Fig. 4.9(b)). The Q factor for that specific resonator was also measured, and it is on the order of 10^4. Therefore, for many applications, the concentrations of 0.005 wt% and 0.002 wt% may be the best options since they present a real likelihood of finding at least one emitter per structure, while maintaining a Q factor greater than 10^4. To validate these results, laser scanning microscopy measurements were also carried out. In Fig. 4.10, it is possible to observe

three emitters in the volume of a single resonator doped in a proportion of 0.002 wt%, which agrees with the measurements shown in Fig. 4.11.

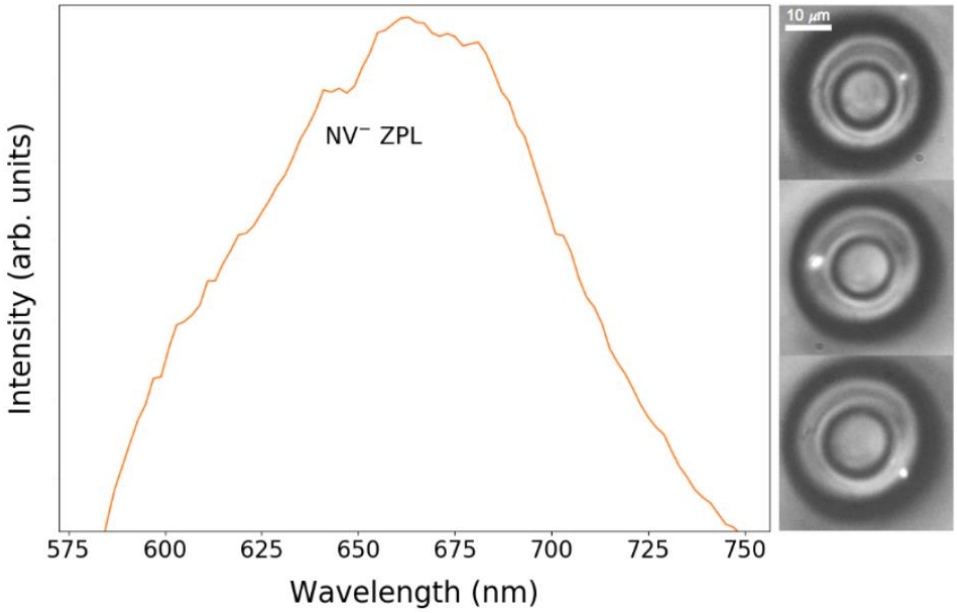

Figure 4.10 - (a) Fluorescence spectrum of a NV center inside a resonator. (b), Nanodiamond emission in three different spots of a single microresonator.
Source: By the author

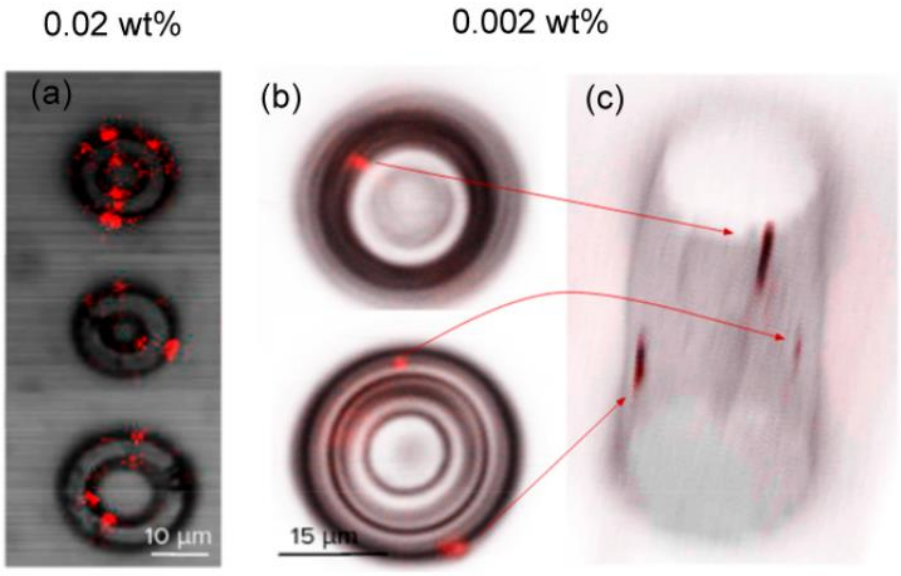

Figure 4.11 - (a) LSM micrography of three resonators doped with 0.02 wt%. b) LSM micrography of the top plane of one resonator doped with 0.002 wt%. (c) 3D image obtained via LSM where it is possible to observe the three fluorescent spots depicted in (b) at the volume of the resonator.
Source: By the author

To obtain a PL spectrum with better signal and spectral resolution, the same setup used to perform Raman spectroscopy (LabRAM) was used to measure the fluorescence of the nanodiamond, at the same points where the Raman measurements were carried out, using a 532 nm laser source. We can see in Fig. 4.12 that the NV PL spectrum is present only in the point where the Raman signal of diamond is observable (blue line) and absent in the neighboring point. In Fig. 4.12, the broad background that corresponds to the NV center emission can be seen, similar to the one presented in Fig. 4.10, as well as the Raman peaks of the polymer (575, 577, 583, 625 - 639 nm). Superimposed to this background, low-Q oscillations that are attributed to Fabry-Perot transverse modes along the microring diameter can be seen, with a FSR of approximately 11 nm and FWHM of 5 nm. Such FSR would be expected for a Fabry-Perot cavity of 29 µm, which corresponds to the resonator diameter (30 µm). As for the NV center emission coupled into the ring resonator modes, in principle a fraction of them would be scattered or radiated into the spectrometer objective and would appear as sharp peaks separated by about 3 nm, considering the lower radial orders of a cylindrical resonator with radius of 15 µm and refractive index of 1.5 [57]. The absence of these peaks is further discussed in Chapter 6.

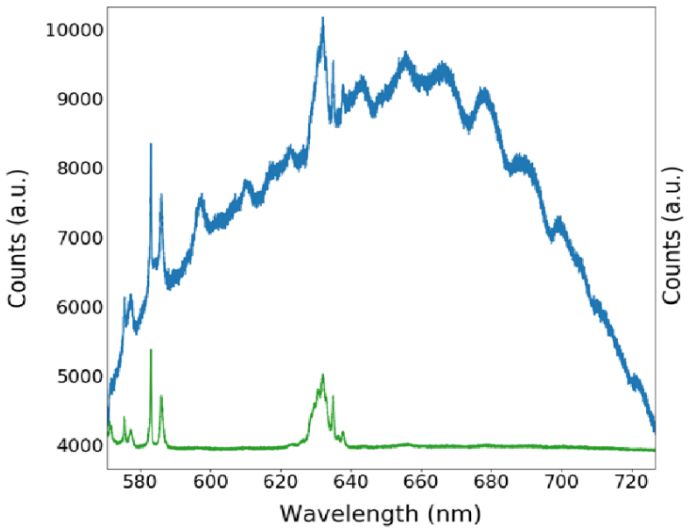

Figure 4.12 - Photoluminescence measurements carried out with the LabRAM equipment at two different points of the structure. In the blue line, the PL signal of the NV center is observable, decorated with the Raman signal of the host material and other modulations in the PL spectra, induced by the resonant cavity.
Source: By the author

5 Cavity engineering for color-center interaction in SiC

5.1 Introduction

Another relevant material for quantum technologies applications is Silicon Carbide (SiC), a technologically mature semiconductor that hosts a diverse family of spin-active point defects (color centers), which exhibit high coherence times. However, their brightness is often limited by shelf state transitions. Additionally, due to vibrational interactions with the crystal lattice, spin-conserving transitions typically constitute a small fraction of the overall emission. To address these challenges, integrating these quantum emitters into photonic cavities becomes imperative to leverage the Purcell effect (Eq. 2.56).

In this chapter we will discuss the work done during an internship at Prof. Evelyn Hu group at Harvard University, where we explored the design of nanophotonic cavities for efficient cavity-emitter coupling of color centers in 4H-SiC. We will start by presenting the nature of 1D photonic crystal cavities, which are the main object of this chapter. Next, we will discuss the numerical methods used to simulate and optimize such structures. Finally, we will discuss the design process and results of the crossbeam and the 'sawfish' nanocavities.

5.2 1D photonic crystal cavities

Photonic crystals are periodic structures with unit cells at scales close to the wavelength of light. Under these conditions, Bloch modes of EM waves can propagate through the periodic medium without scattering. Due to this periodicity, the allowed frequencies for the Bloch modes form a discrete set. A typical band diagram (wavevector as a function of frequency) of a photonic crystal is shown in Fig. 5.1. It is important to note that such band diagrams only need to be calculated in the first irreducible Brillouin zone. This zone represents the boundaries of the first unit cell in the reciprocal space, which is a transformation of real space but uses wavevectors instead of positions. The first irreducible Brillouin zone has the smallest rotational symmetry among all Brillouin zones.[58]

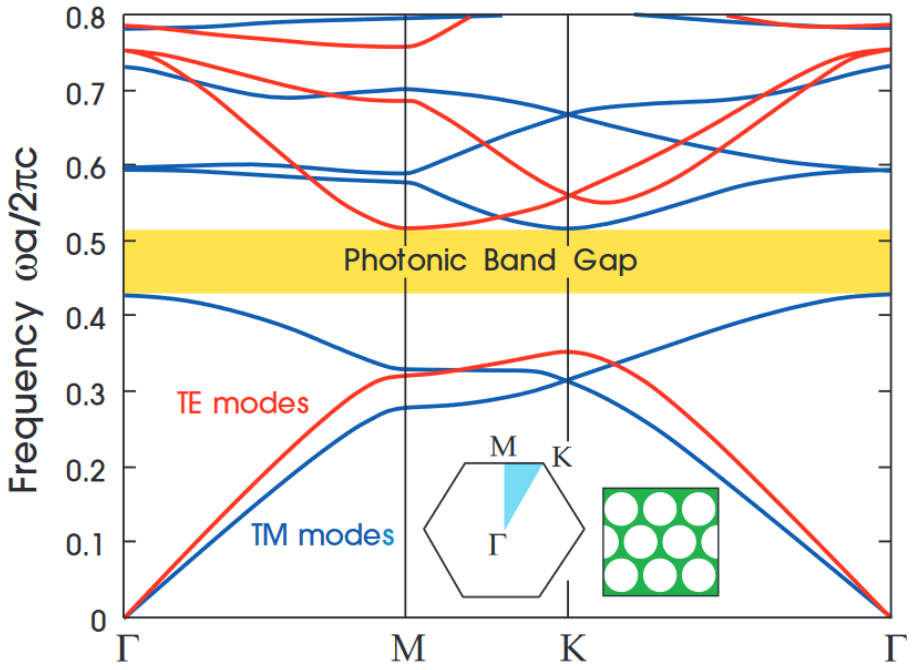

Figure 5.1 - Band diagram of a 2D photonic crystal presenting a complete bandgap. In the inset, representation of the first Brillouin zone, and in blue, the irreducible Brillouin zone.
Source: JOANNOPOULOS *et al*.[58]

It may happen that, for a given range of frequencies, no solution exists for a propagating wave, as can be seen in Fig. 5.1. In such conditions, the medium is perfectly reflective for EM waves at these frequencies, forming what is called the photonic bandgap. If one adds a point defect in a perfect crystal lattice, it will create new energy states within the crystal's bandgap, and hence confine light at frequencies within the photonic bandgap.

At first glance, a 3D photonic crystal, a structure periodic in all three dimensions, would be necessary to form a cavity. Such structures, however, are very complex to fabricate. As an alternative, 2D and 1D photonic crystals have been explored to form cavities,[59] in which the confinement at the non-periodic directions is due to total internal reflection.

Considering the simplicity of fabrication, high-quality factors and tight confinement of the EM mode, 1D photonic crystals have recently attracted more attention for use in emitter-cavity coupling applications.[4,27,60–62] The traditional structure, often called nanobeam cavity, consists of a slab waveguide with hole unit cells inscribed.[60] As can be seen in Fig. 5.2, a stack of unit cells at each side will act as Bragg mirrors and promote the confinement in the *x*-direction. In the central part of the structure, there is a tapered region where the unit cells parameters are adiabatic

changed to slowly move the bandgap position, forming a cavity region to accommodate the EM mode at the desired frequency.

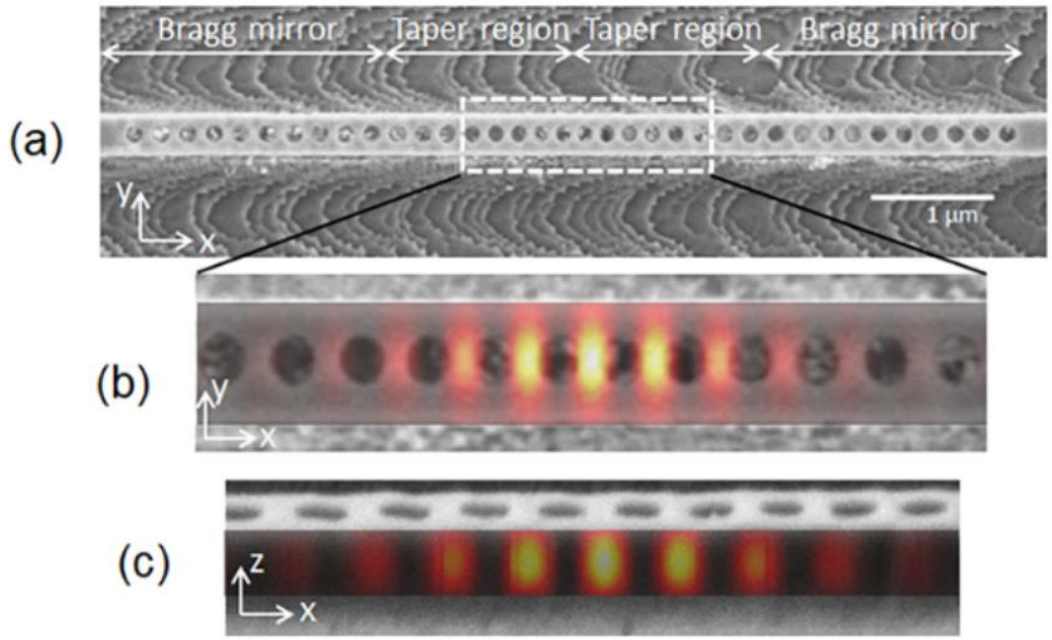

Figure 5.2 - (a) *xy* view of a typical nanobeam photonic cavity, depicting the mirror and taper regions. (b) Electric field profile at the *xy* and plane. (c) Field profile in the *xz* plane.
Source: BRACHER[62]

A straightforward approach to creating a cavity might involve simply removing the unit cells at the center of the structure. However, this abrupt change in the periodicity would lead to light scattered in the free space, since it would be prone to generate components in the frequency domain with k-vectors that do not fulfill the conditions for the total internal reflection at the non-periodic interfaces[63]. On the other hand, a gentle envelope of the EM field avoids the generation of components with low k-vectors, as illustrated in Fig. 5.3, greatly improving the cavity Q-factor.

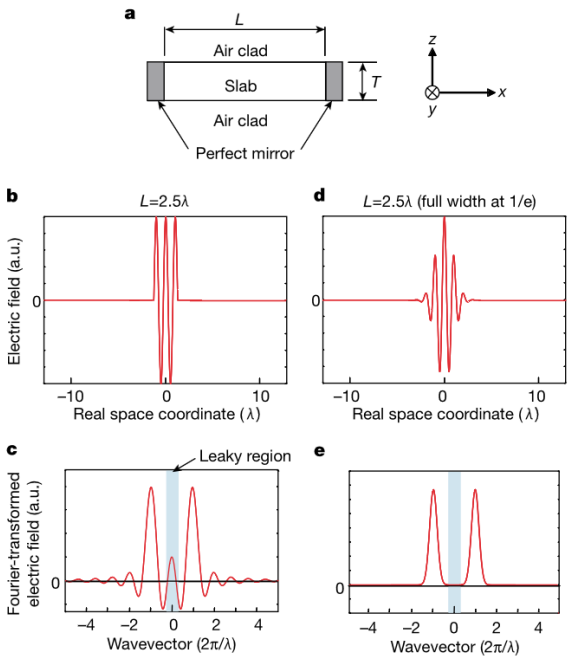

Figure 5.3 - (a) Simplified model of a cavity formed by perfect mirrors. (b) The electric field inside such cavity, where the abrupt change in the electric field leads to leak components in the FT spectrum shown in (c). (d) Electric field profile with a gentle envelope function, suppressing the leak components in the frequency spectrum (e).
Source: GERSHGORE[63]

5.4 The Finite-Difference Time Domain (FDTD) method

Due to the high parameter space of typical nanocavities, combined with the cost and time expenses of fabrication, it is not practical to optimize such devices in a try-and-error approach. Instead, it is useful to numerically solve Maxwell equations to find optimal parameters for a given structure. A common method to achieve this is the Finite-Difference Time Domain (FDTD) method, which consists of numerically solving the Maxwell equations using the Finite-Difference method, explicitly calculating its evolution in time with small steps.[64]

The FDTD method consists in discretizing the computational volume in a uniform grid, and solving the time domain evolution of the fields:

$$\frac{\partial \boldsymbol{B}}{\partial t} = -\nabla \times \boldsymbol{E} - \boldsymbol{J_B} \tag{5.1}$$

$$\frac{\partial \boldsymbol{D}}{\partial t} -= \nabla \times \boldsymbol{H} - \boldsymbol{J} \tag{5.2}$$

where J_B is an artificial magnetic current, useful for magnetic dipole sources.

FDTD simulations have some advantages over other methods, namely Finite-element methods (FEM), such as a high parallelization, less memory consumption (as it does not rely on linear algebra), and can naturally handle non-linear materials.[65]

Another feature of FDTD is the possibility of obtaining the frequency domain fields over a broad spectral region in a single run, by the Fourier transform of the time domain fields. This is particularly interesting for simulating resonant cavities as one cannot know beforehand what would be the exact resonant frequency after changing cavity parameters. Hence, one can excite a resonator with a broad Gaussian pulse and analyze the resonances in the frequency domain. However, there is one sublet: The Fourier transform of the time-domain fields would only be equivalent to the frequency domain fields in the limit that all field components go to zero. As an example, it is known that the Fourier transform of an exponential decaying oscillating field is a Lorentzian curve. On the other hand, for a truncated field, the Fourier transform becomes a Sinc function, as can be seen in Fig. 5.4, where the side oscillations in frequency domain are artifacts due to the truncated fields. As running simulations until the fields totally decay is unpractical for resonant cavities, the Fourier transform is not an appropriate method to calculate the Q-factors. Also, care must be taken to calculate other quantities, such as the mode volume.

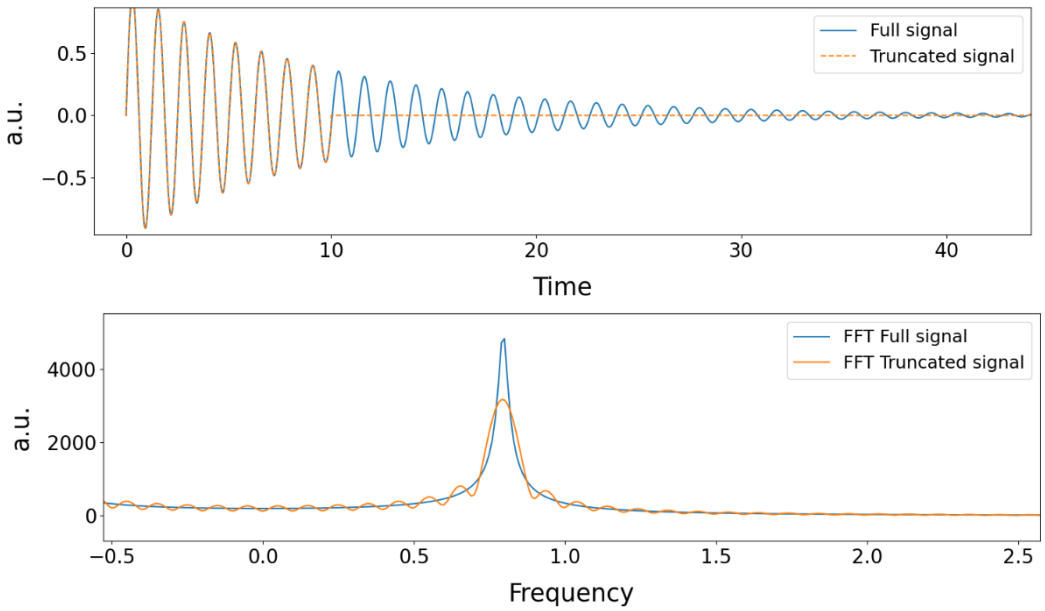

Figure 5.4 - Time and frequency domain spectrum of a full (orange) and truncated (blue) exponential decaying signal.
Source: By the author

For the Q-factor calculation, it is preferable to use the Harmonic-inverse algorithm[66], which assumes that the signal is an exponential decaying field, and decompose it as a discrete series of exponential components, with the form of:

$$E(t) = \sum_i e^{-f_i \alpha_i} \tag{5.3}$$

where f_i is the resonant frequency for a given component, and the Q-factor can be derived from the decaying constant α. Different from a Fourier transform, which is a generic approach, the Harmonic-inversion algorithm makes a strong assumption about the fields and can yield accurate results with less data points. To ensure that the signal will fall under the algorithm hypothesis and achieve accurate results, it is necessary to start the analyses after the full decay of the source.

An alternative method for Q-factor calculation is to accumulate the fields in all simulation volume at the final steps and calculate the flux leaving the simulation domain in all its 6 faces, during a time window equivalent to one oscillating period. The total energy is calculated as the temporal mean:

$$U = \frac{1}{\Delta T} \int |E(t)|^2 dt \tag{5.4}$$

and the Q-factor can be directly calculated by its definition:

$$Q = 2\pi\nu \frac{U}{U_{lost}} \tag{5.5}$$

Although this method is more computationally expensive than the harmonic inversion algorithm, as it needs to accumulate field data in all simulation domain for several time steps, while the harmonic inversion algorithm only demands a 1D field, this approach allows one to estimate the directional Q-factors, and hence gather information about what directions are the main source of losses. As an example, if the main source of losses is in the *x*-direction, a simple increase in the number of mirror unit cells can be enough to greatly improve the Q-factor. Also, some applications, such as tapered fiber coupled cavities,[4] demands cavity engineering to direct losses to the optical fiber. A third time-domain method for Q-factor calculation is to directly fit the exponential envelope of the decaying field. Although this method yields similar results

to the harmonic inversion, its implementation is complex and offers no advantage. Figure 5.5 shows a benchmark of the three methods.

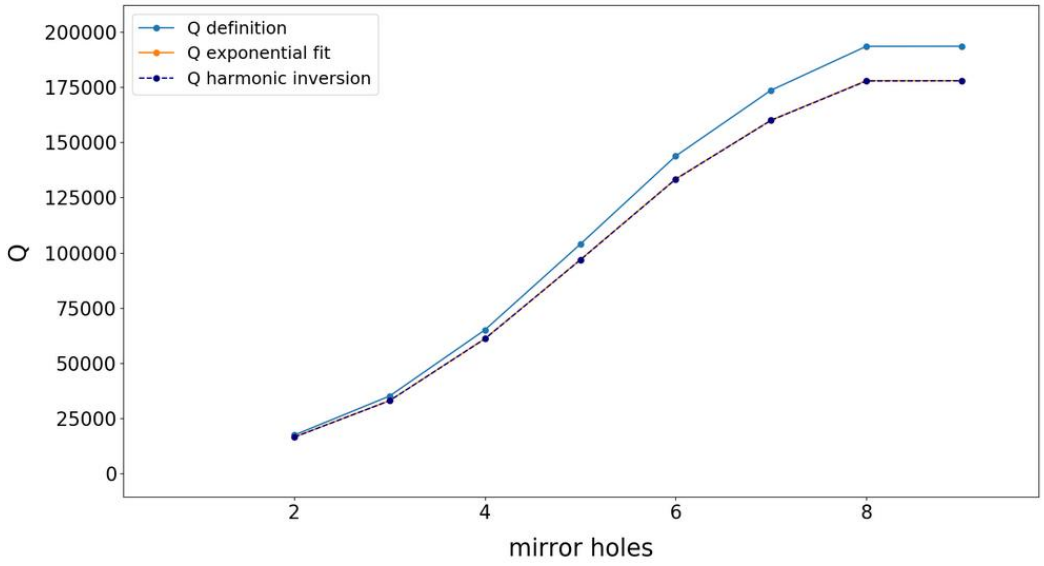

Figure 5.5 - Comparison of the Q-factor calculation of three different methods.
Source: By the author

For mode volume calculation, the temporal mean of the fields is computed at the end of the simulations (eq. 5.4), and the definition of Eq. 2.46 is calculated.

Finally, it is important to define the boundary conditions (BC) to truncate the simulation space to a limited volume. To simulate open boundaries, it is necessary to have a computational domain where the EM wave is fully absorbed without reflection before reaching a perfect electric or magnetic boundary, which would reflect incident EM fields. This is achieved by the Perfect-Matched Layer (PML), an artificial medium that absorbs EM radiation without reflection. A simple implementation involves adding a stretch factor ($s(x)$) in the wave equation, so it becomes:

$$\left[\left(\frac{1}{s(x)}\frac{\partial}{\partial \mathrm{x}}\right)^2 + \frac{\partial^2}{\partial \mathrm{y}^2} + \frac{\partial^2}{\partial \mathrm{z}^2} - \frac{1}{c^2}\frac{\partial^2}{\partial t^2}\right]E = 0 \tag{5.6}$$

where:

$$s(x) \equiv 1 + i\frac{\sigma}{\omega\epsilon_0}, x > 0 \tag{5.7}$$

Considering the simple case of a plane wave, we have:

$$E(x) = e^{i(\boldsymbol{k}.\boldsymbol{r}-\omega t)} e^{-\frac{\sigma}{c\epsilon_0}x} \tag{5.8}$$

So, inside the PML region, there is an exponential decaying term independent of the frequency and incidence angle, as illustrated in Fig 5.6:

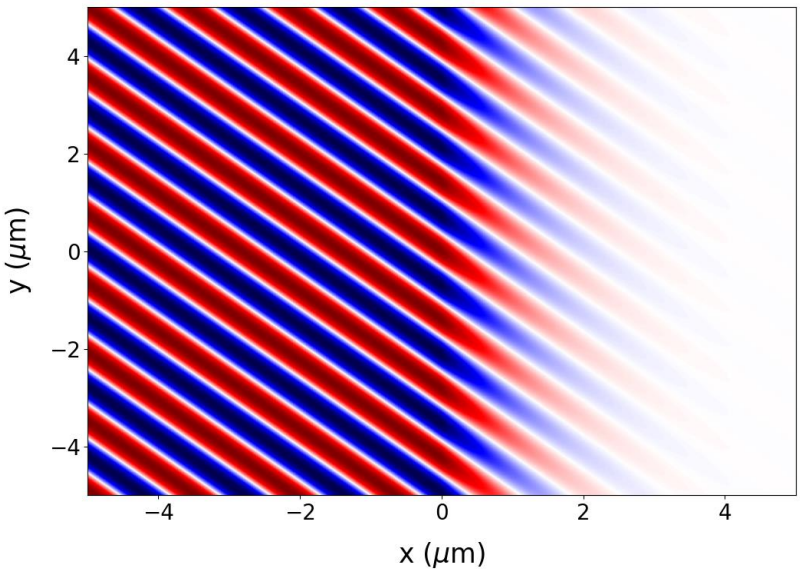

Figure 5.6 - Example of an angled plane wave incident in a PML layer (x > 0).

Source: By the author

However, it is important to note that the PML is perfect only in the limit of a continuous grid, so the discretization adds spurious reflections, which must be mitigated by adding multiple layers of PML, as well as a tapered σ(x) factor.[67] Also, the PML implementation previously presented will only absorb propagating fields. Although there are more complex implementations that can handle evanescent fields,[67] it is good practice to place the structures at enough distance from the PMLs.

Another important BC is the Bloch periodic boundary condition. This technique involves copying the fields from the opposite boundary, but with a specific phase shift to account for the wave's angle of incidence. This ensures that the wave leaving one boundary seamlessly re-enters from the opposite boundary, mimicking an infinite periodic system. Bloch periodic boundary conditions are particularly useful for simulating plane waves propagating with some given angle, and band-diagram simulations.

5.3 Double nanobeam cavity optimization

As the Purcell effect can enhance the emission at a sharp spectral band, it becomes a valuable tool for resolving a specific defect from a broad emission spectrum composed of many emitters. Given that many defects are only bright in a specific charge state, leveraging the Purcell effect offers a valuable resource for studying the charge dynamics of these emitters. In particular, the V_{Si} color center in 4H-SiC exhibits a bright state only in the V_{Si}^- charge state, while the VV defect is bright only in its neutral state. This phenomenon has been explored in different papers,[68-69] where variations in the fluorescence intensity of V_{Si} color centers over time were observed under continuous light excitation, as depicted in Fig. 5.7:

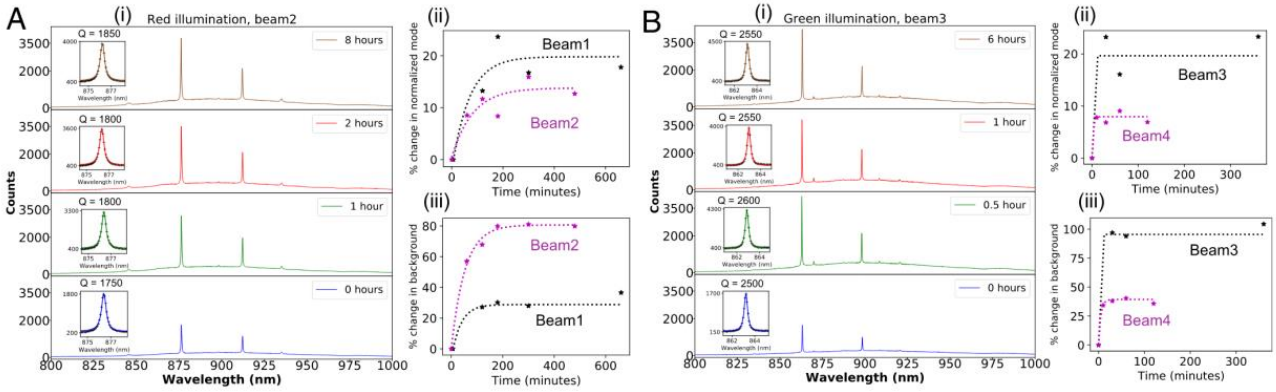

Figure 5.7 - Fluorescence over time under continuous red (A) and green(B) illumination.
Source: Adapted from GADALLA [69]

From Fig. 5.7, one can observe an enhancement in the emission of the V_{si} center until a saturation point, which is reached more rapidly under green illumination. A hypothesis for this behavior is that the illumination may promote electrons from other defects into the conduction band. These electrons are then captured by neutral V_{si} centers, whose energy is close to the SiC valence band, causing them to transition from a dark state to a bright state. The faster saturation time observed with the green laser can be understood by referring to the energy diagram of defects within the bandgap of SiC, as illustrated in Fig. 5.8:

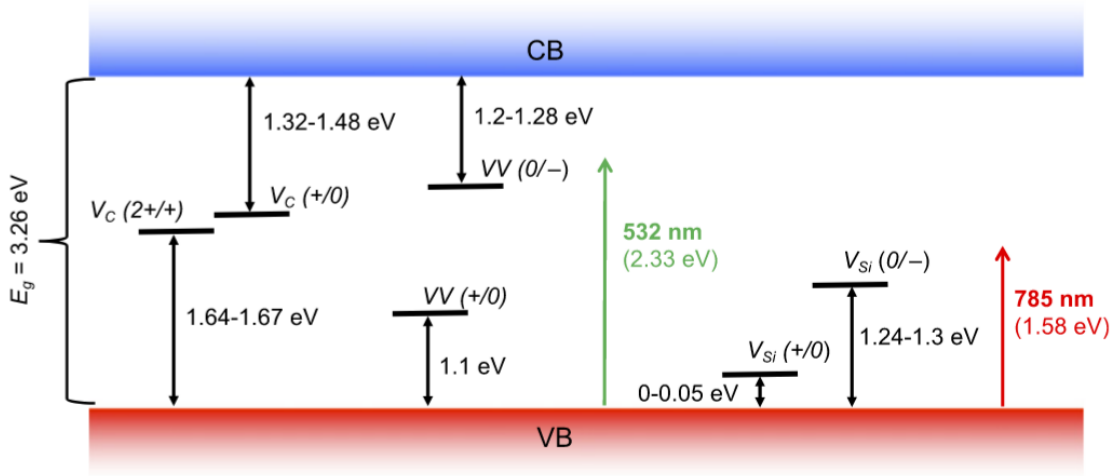

Figure 5.8 - Energy diagram for different color centers in 4H-SiC, within the bandgap of the semiconductor.
Source: Adapted from GADALLA [69]

From the diagram, it is noticeable that laser irradiation at 532 nm provides enough energy to ionize more defects than irradiation at 785 nm, thereby explaining its faster saturation time. One way to directly investigate this mechanism can be realized with a cavity having two resonances in the same mode volume, allowing for the monitoring of fluorescence dynamics from two defects simultaneously. One potential structure for this purpose is the "crossbeam" cavity, comprising two orthogonal nanobeam cavities that are independently tuned. While feasible, designing this structure is not trivial, given that each nanobeam represents a potential leakage path for the other.

This structure has been previously studied, and one approach to mitigate leakage from the orthogonal cavity involves using square holes instead of the traditional elliptical holes found in nanobeam cavities.[62] This modification allows for a larger dielectric-air region, facilitating better light confinement. While progress has been made, as illustrated in Fig. 5.9, achieving a deterministic method for tuning the cavities to specific wavelengths while maintaining reasonable Q factors remained challenging. It's noteworthy that inverse design approaches were also explored (Fig. 5.9(b)), and although successful in tuning the cavities, Q factors were insufficient for practical experimental applications.

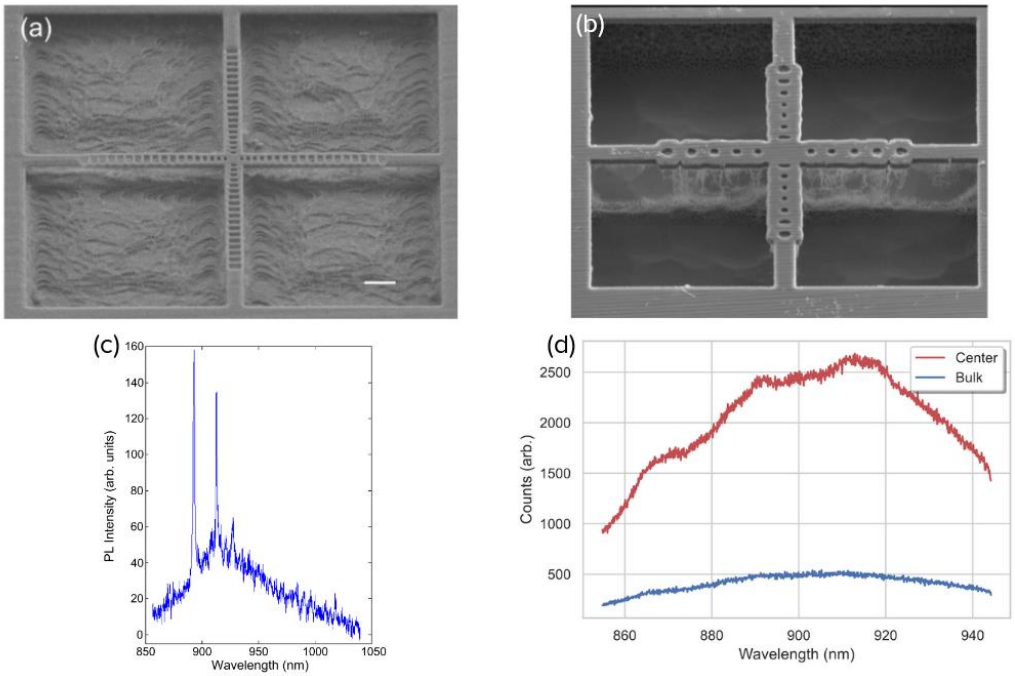

Figure 5.9 - (a) SEM micrography and photoluminescence spectrum and of a crossbeam designed with forward design. (b) Photoluminescence spectrum of the cavity presented in (a). Q factors are on the order of 2,000. (c) SEM of a crossbeam designed with inverse design. (d) Spectrum of the cavity presented in (c). Q factors on the order of 500.
Source: Adapted from BRACHER [62]

To further improve the Q-factors and tunability of such structure, FDTD solvers were employed to simulate the cavities, and computational algorithms were explored to automatically search for optimal parameters, enabling the tuning of the cavities for specific wavelengths, particularly 916 nm (V_{Si}) and 1074 nm (VV).

The first step involves optimizing independent nanobeam cavities for the desired wavelengths. To achieve this, we begin by optimizing the unit cell parameters to obtain a large photonic bandgap centered at the desired resonant frequency. We simulate a single unit cell with Bloch periodic BC in the *x*-coordinate (the direction of periodicity) and PML BCs in the other directions. To excite a broad range of modes, 5 point-dipoles are randomly distributed within the computational volume. Additionally, five field monitors are also randomly placed to collect the fields and retrieve the resonances. Figure 5.10 shows a typical resonance map for a 1D-photonic crystal. Here, we can observe the Bloch modes below the air cone and the bandgap at the edge (last point) of the Brillouin zone. To reduce computational cost and simplify the analysis, during optimization steps only the resonances at this last point are calculated.

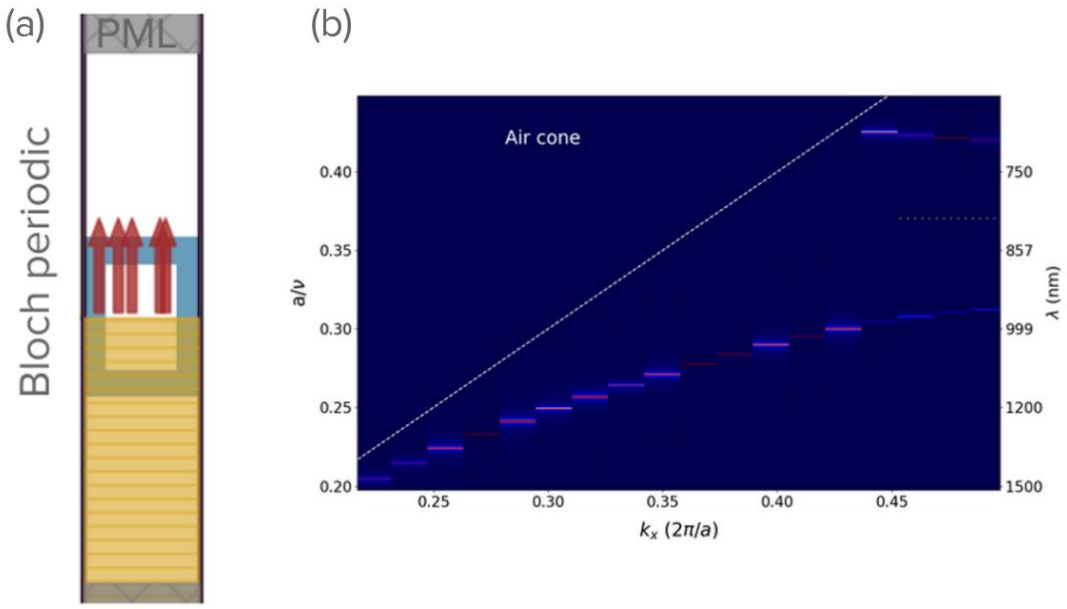

Figure 5.10 - (a) Schematics of the computational model used for band diagram calculation. The arrows represent the position of each point-dipole source. The blue region represents the material (SiC). The yellow area represents the symmetry plane. (b) Map of the Fourier transform fields for each k_x value, where the frequency of the Bloch-modes can be seen as peaks in the Fourier transform.
Source: By the author

The next step consists in optimizing the tapered region of the resonator, which is a region where the unit cells are gently modified, to slowly detune the photonic bandgap, forming a cavity region. As shown in Fig. 5.11, the dimensions and lattice constant of the unit cells are then modified according to a polynomial function until they reach a predefined factor, which is a free parameter to be optimized.

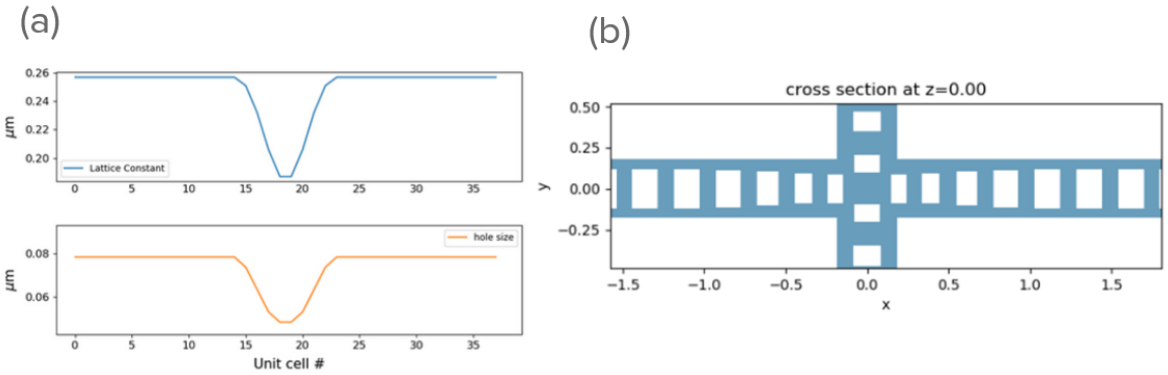

Figure 5.11 - (a) Size variation of the lattice constant (blue) and hole size (orange). (b) Cross section of the structures tapered region.
Source: By the author

The choice of the number of unit cells in the cavity region was taken from the

Literature.[60] To excite the resonant modes, a point dipole source is placed in the middle of the cavity, with a Gaussian time dependency. This approach allows for the simultaneous investigation of a broad frequency range.

The next step involves crossing the independent nanobeams and optimizing the free parameters to achieve the desired resonances. To prevent overlap between the first unit cells of the crossed nanobeams, an additional free parameter is introduced: the cavity gap. This gap defines the distance between these first unit cells.

Due to the large parameter space for this problem (eight parameters for each nanobeam), we categorized the parameters into two groups, as illustrated in Fig. 5.12: cavity parameters, primarily responsible for confining the fields and directly contributing to achieving high Q factors and low mode volumes, and mirror parameters, which control the photonic crystal bandgap and are mainly responsible for the resonance frequency.

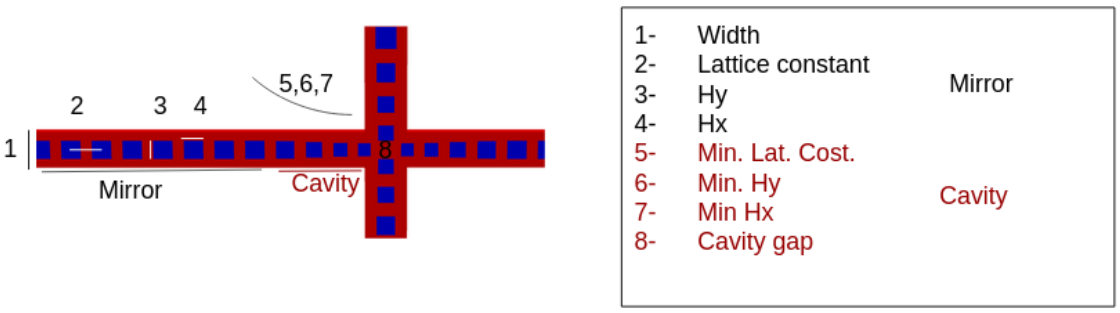

Figure 5.12 - Schematics of the model and parametrization of the crossbeam.
Source: By the author

Since the computational volume is large, it is important to take full advantage of the problem symmetries. Hence, mirror symmetries are applied in all three dimensions, reducing eight times the computational cost, as shown in Fig. 5.13. One issue is that it is necessary to simulate each cavity separately since the field symmetries are different. For the horizontal cavities, the symmetries are even in *x* and z-direction, and odd in *y*-direction, while for the vertical cavity, they are even in *y* and *z*-directions, and odd in *x*-direction.

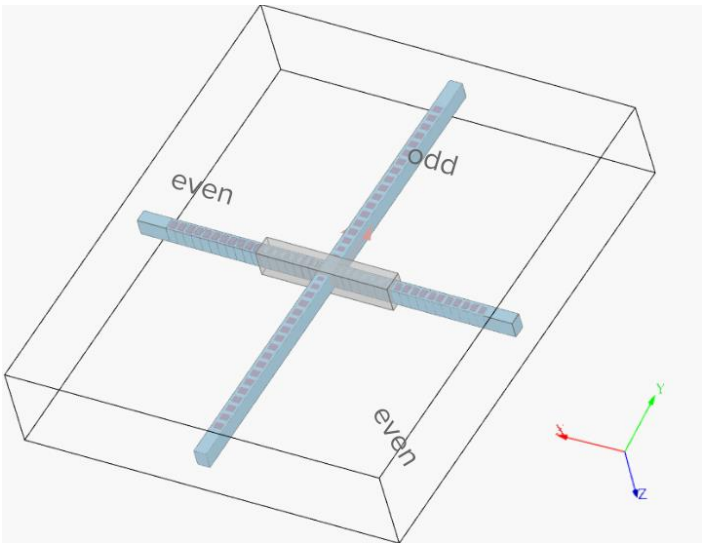

Figure 5.13 - Computational model of the crossed nanobeam, depicting the proper symmetries for simulating the resonances at the horizontal cavity.
Source: By the author

Owing to the large parameter space, a gradient-based optimization algorithm is not practical. Therefore, the simplex algorithm[70] was employed to find optimal parameters that minimize the given objective function:

$$F = Q_{penalty}\sqrt{(100000)\frac{V_x V_y}{Q_x Qy}\, e^{(\Delta\lambda_x+\Delta\lambda_y)}} \tag{5.8}$$

$$Q_{penalty} = \min(Q_x, Q_y) \tag{5.9}$$

$$\Delta\lambda = \alpha\sqrt{\left(\lambda_{target} - \lambda_{simulated}\right)^2} \tag{5.10}$$

The term $Q_{penalty}$ is introduced to prevent significant improvement in the Q-factor of one cavity at the expense of the other. The term $(V_xV_y)/(Q_xQ_y)$ enforces a high Q/V ratio for the cavities, and the parameter $\Delta\boldsymbol{\lambda}$ is the detuning penalty, weighted by the parameter α. It was observed that the most effective approach is to initially set α = 0, allowing the parameters to freely optimize for the highest possible Q factors without constraint on the resonance frequency. After the Q-factor optimization, each nanobeam is scaled in to be resonant with the desired frequencies. Since Maxwell equations are scale-invariant, this approach would work perfectly for a single nanobeam. However, since this is a coupled problem, the Q-factor and resonance frequency of one cavity depend on the other. Also, the height is a fabrication constraint, hence cannot be modified. Nevertheless, this approach allows the cavities to get closer to their intended resonance frequency, while keeping high Q-factors.

Subsequently, the optimization is rerun with a gradual increase in the parameter α, thereby slowly constraining the cavities to the desired resonant frequencies. After several optimization steps, a cavity tuned to the desired wavelengths with Q factors on the order of 10^4 was achieved. A plot of the electric field profiles of such cavity are shown in Fig. 5.14:

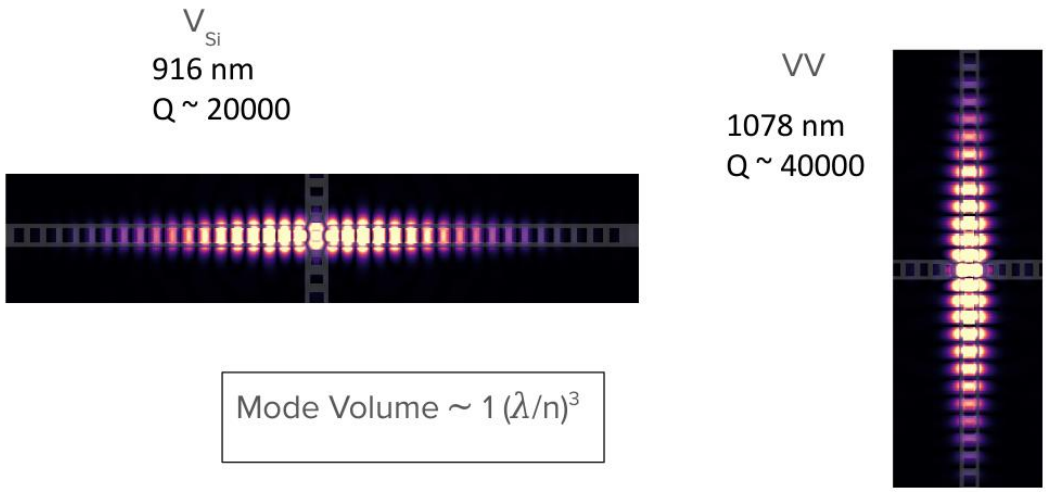

Figure 5.14 - Plot of the electric field of the optimized crossbeam structure.
Source: By the author

To broaden the applications of such a design, we explored convenient methods for tuning the optimized cavity. As illustrated in Fig. 5.15, the fields of one cavity exhibit low penetration into the orthogonal one. Therefore, only the parameters of the central unit cells are crucial for providing confinement of the fields of the orthogonal one. Hence, starting from a previously optimized crossbeam, it becomes possible to decouple both cavities by maintaining these unit cells constant.

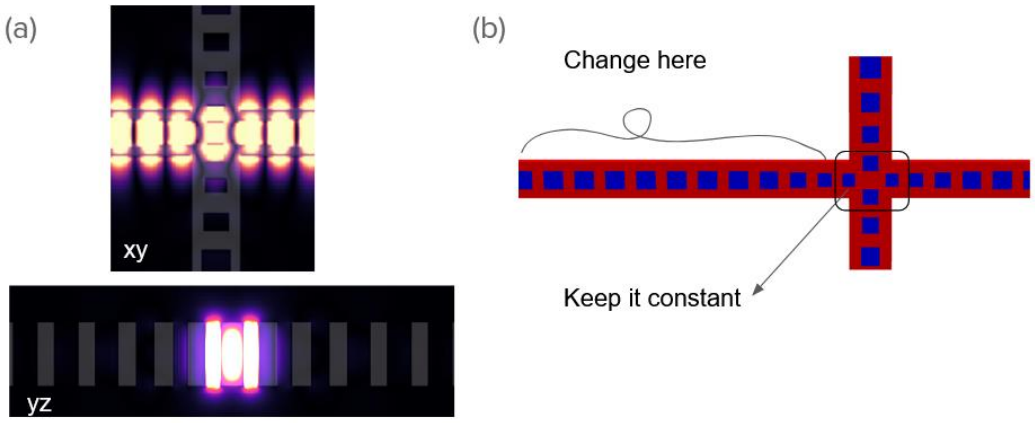

Figure 5.15 - (a) Cross-section of the electric field at the *xy* and *yz* planes. (b) Scheme of the free unit cells to decouple the nanobeams.
Source: By the author

To investigate this approach, simulations were conducted by keeping the central unit cells constant while varying the lattice constant of one of the nanobeams. As depicted in Fig. 5.16, the resonant wavelength of one of the beams is tuned, while the Q factor of the orthogonal beam does not abruptly change. Conversely, if the parameters of the central unit cells are also altered, the Q-factor of the orthogonal nanobeam is significantly affected, as shown in Fig. 5.16(a).

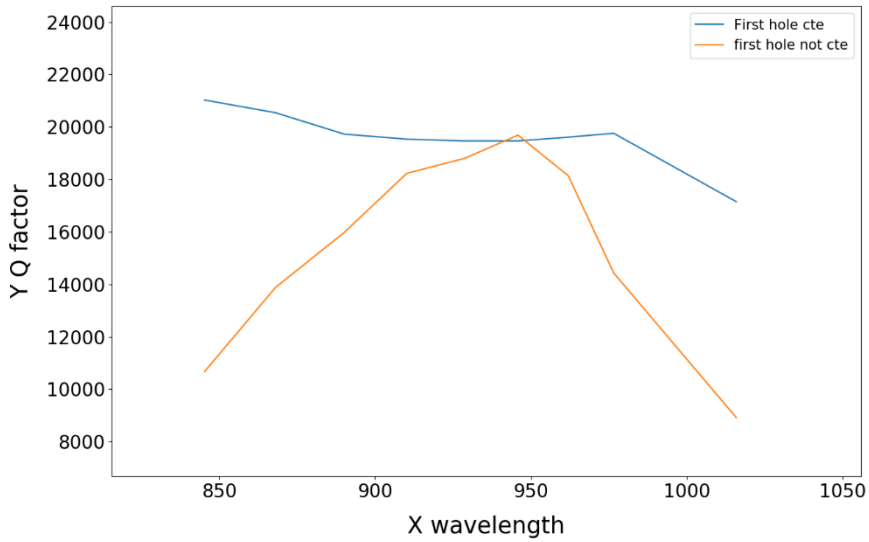

Figure 5.16 - Q factor variation of one nanobeam while tuning the other, keeping the central unit cells constant (blue line) and changing the central unit cells (orange line).
Source: By the author

In conclusion, we have successfully designed the crossbeam cavity for experimental applications and developed a straightforward approach to tune each cavity. For future development of the design, other optimization approaches, such as genetic algorithms, can be considered. The cavities are currently in fabrication, and a recently fabricated structure is displayed in Fig. 5.17.

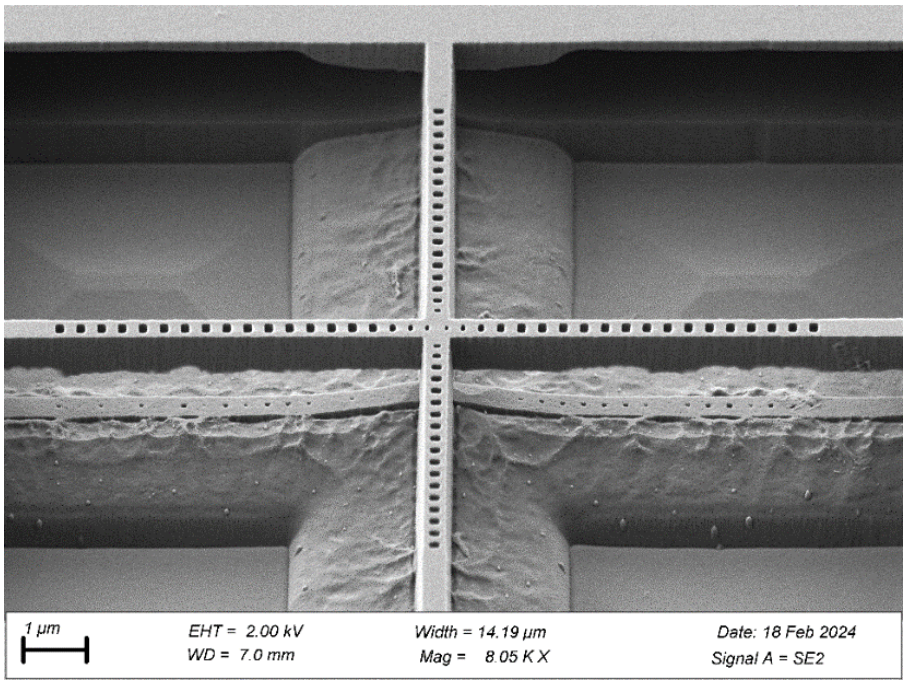

Figure 5.17 - SEM image of a partially fabricated crossbeam cavity.
Source: By the author

5.4 Sawfish cavity and edge coupler design sawfish

While nanobeam cavities have been successfully used for emitter-cavity coupling, there are some downsides to using this structure. The small size of the holes makes them prone to proximity effects during the electron beam lithography. Additionally, varying sizes of the holes in the tapered region pose extra challenges for optimization in various steps of fabrication processes. Finally, a hole-based lattice constant will act as a mirror for TE-polarized light (electric field confined in the plane of the cavity)[58], which is not ideal for defects such as V_{Si}, where the electric dipole moment has a larger component oriented in the *z*-axis.

Recently, a new nanocavity design called the "sawfish" cavity was proposed[71]. The sawfish cavity is a type of 1D photonic crystal cavity where the lattice constant is formed by sinusoidal structures around a thin waveguide, as depicted in Fig. 5.18. This structure holds promising advantages for applications in SiC, as it displays larger features that could potentially ease the requirements for electron beam lithography. Additionally, it accommodates TM modes, allowing for better cavity-dipole alignment for V_{Si} centers.

To explore this type of device, we conducted simulations using SiC parameters, aiming for resonances near the V_{Si} ZPL (around 916 nm). Additionally, to avoid breakage and anticipate difficulties in the fabrication process, we aimed to optimize the structures for larger sizes of the central waveguide. Using similar methods described in the previous chapter, we were able to design cavities presenting theoretical Q factors on the order of 10^5, with central waveguide sizes up to 100 nm.

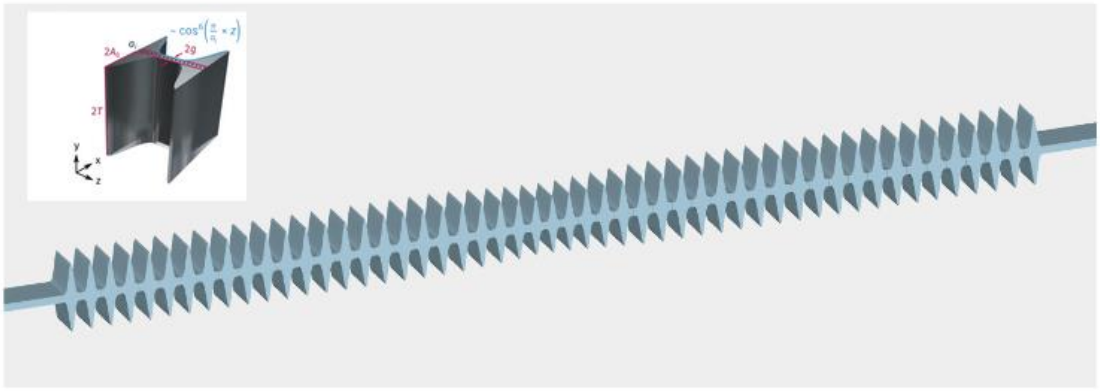

Figure 5.18 - Model of the ‘sawfish’ cavity. The inset represents the unit cell model.
Source: Adapted from BOPP [71]

A useful method for light extraction of nanobeam cavities is using side-couplers that allow for efficient interaction and controlled light extraction. Although it has been explored in traditional nanobeams,[72] due to the large size of the lattice constant of the sawfish cavities, new approaches to incorporate edge couplers to these structures are necessary.

One possibility is a sawfish-like coupler, with the photonic crystal phased from the nanocavity, as depicted in Fig. 5.19(a). In this approach, the lattice constant on the left

side of the coupler acts as a mirror, while the phase difference allows placing the coupler in proximity to the cavity to interact with the evanescent wave.

Another approach involves an asymmetric tapering in the cavity region of the nanocavity, creating space for a sinusoidal-like coupler to interact via evanescent wave, as illustrated in Fig. 5.19(b). Both designs seem promising for out-coupling light from the resonances, presenting theoretical coupled Q factors on the order of 10^5 while directing most of the losses to the coupler.

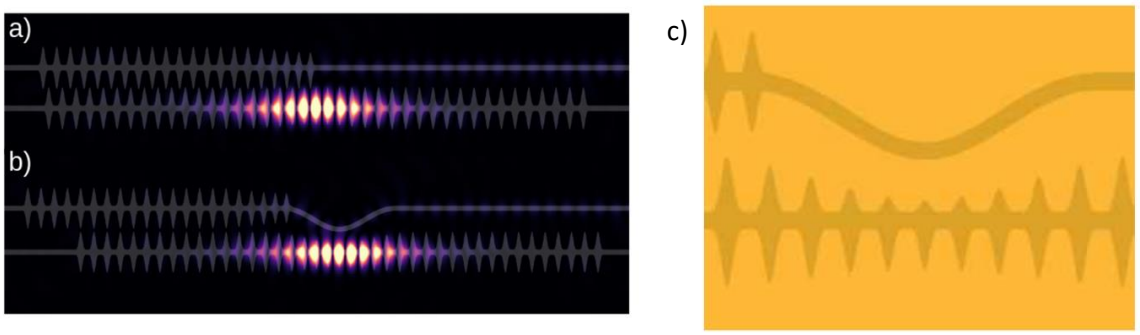

Figure 5.20 - (a) and (b) Different designs of edge couplers for the ‘sawfish’ cavity. (c) Representation of the asymmetric tapering at the coupling region.
Source: By the author

A slightly different simulation is carried out to estimate the coupling efficiency. Instead of exciting the mode with a point dipole source at the center of the structure, a guided mode is launched at the right side of the coupler, and its reflectance spectrum is analyzed. Field monitors inside the cavity track the resonance frequency and Q factors. The coupling efficiency can be defined as[73]:

$$\eta_c = \sqrt{\frac{P_R}{P_0}} \tag{5.11}$$

where P_R is the reflected power and P_0 is the injected power.

Hence, 100% efficiency is attained when the reflectance dip drops to 0. An example spectrum is depicted in Fig. 5.20(c), where a broad reflected spectrum caused by the photonic crystal bandgap is seen, with a dip in the middle due to light coupled to the cavity. As one can see in Fig. 5.20 (a) and (b), the steady-state field profiles using the point dipole and the guided mode are equivalent.

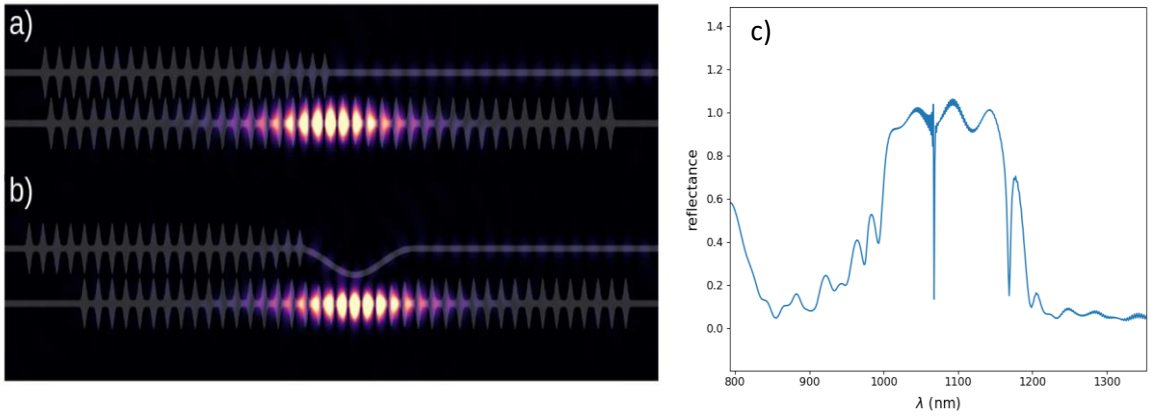

Figure 5.21 - (a) and (b) show the simulations where a mode is launched from the waveguide and coupled to the cavity. (c) reflectance spectrum of the coupler.
Source: By the author

6 New geometries for better cavity-emitter interaction

6.1 Mode volume analysis

Considering the results presented in Chapter 4, no Purcell enhancement was observed in the cylindrical structures fabricated via 2PP. In Chapter 5, the importance of the Q/V factor while designing structures for cavity-emitter coupling is discussed. The issue of optical insulation is an object of many studies regarding the designing and fabrication of photonic cavities for cavity-emitter applications, [74-75] aiming to improve Q-factor and reduce mode volume. Typical nanobeam cavities reach mode volumes on the order of $1\left(\frac{\lambda}{n}\right)^3$, achieving Purcell enhancement of 50 to 80-fold, for cavities presenting Q-factors on the order of 10^3 [48,76].

For the structures presented in Chapter 4, although Q-factors of 10^4 can be easily achieved, the issue of confining the mode to a small volume is not addressed. In order to investigate the magnitude of the mode volume of our structures, we simulated cylindrical resonators with different heights, and calculated their Q-factors and mode volume using the same methods presented in Chapters 4 and 5. Due to the large size of the resonators, we constrained the simulations to structures with a fixed radius of 5 μm, and heights ranging from 1 μm to 10 μm, and structures with fixed height of 2 μm, and radius varying from 5 μm to 15 μm.

The results, shown in Fig. 6.1, reveal an approximately linear increase of the mode volume as a function of the height, which can be understood by the electric field distribution in the *z*-direction, depicted in the inset of Fig. 6.1. Projecting the results for a typical structure with 20 μm radius, and 50 μm tall, we can estimate that mode volume can be higher than 1000 $\left(\frac{\lambda}{n}\right)^3$, which agrees with values already reported in the literature for WGM resonators[77]. Hence, Purcell enhancements around 100 times lower than typical reported values would be expected, yielding emission enhancements too low to be observed in experiments. Also, the low contrast index between the polymer and glass substrate (~1.5) may pose another factor to increase mode volume.

6.2 Disk cavity fabricated with 0.25 NA objective

To enhance cavity-emitter coupling, it is necessary to modify the geometry of the tall cylinder resonator to obtain a better confined mode. A possible approach to achieve this, that leverages the already optimized fabrication protocol, is implementing a variable radius as an exponential function of the *z*-coordinate, defined as:

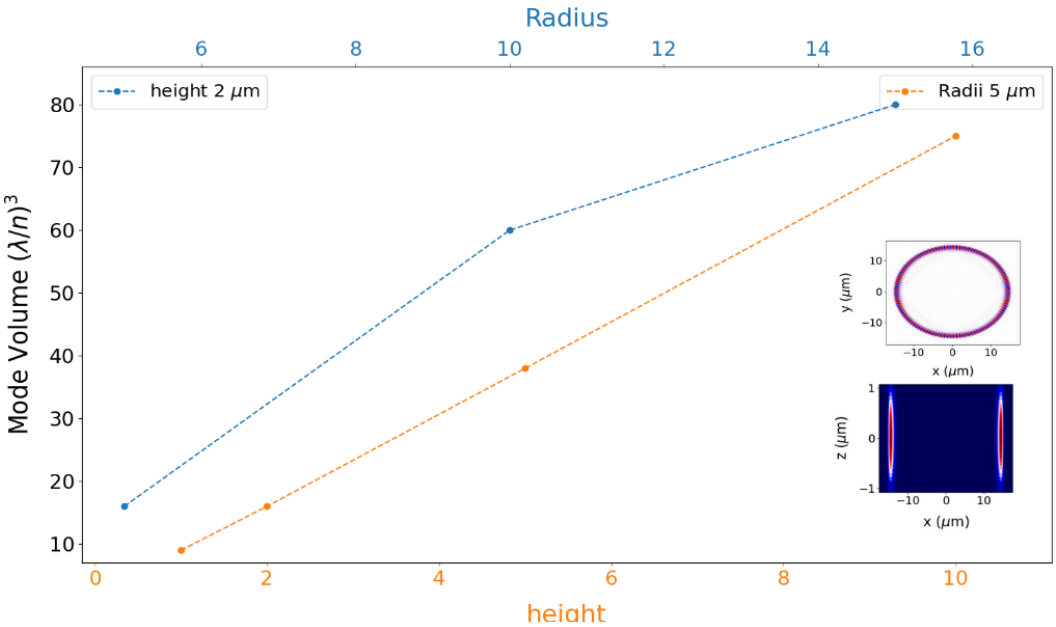

Figure 6.1 - Mode volume of a first-order resonance of a cylindrical resonator as a function of height (orange) and radius (blue). In the inset, field profile in the *xy* and *xz* planes.
Source: By the author

$$R_{trasition}(z) = R_0 + (R - R_{base})e^{\alpha[(z-z_0)-L_t]} \tag{6.1}$$

In Eq. 6.1, R_0 is the radius at the base, R is the final radius, Z_0 is the *z*-coordinate of the start of the transition region, and L_t is the length of the transition region. This transition is necessary to sustain an upper disk that will form the resonant cavity. A schematic of such geometry can be seen in Fig. 6.2(a).

To confirm that such structure can confine a mode at the upper disk that will not leak into the transition region, FEM simulations were carried out to compute the cavity modes. The result for a structure with disk radius of 5 μm and disk height of 2 μm can be seen in Fig. 6.1, where (b) is the *xz*-plane, and (c) the *xy*-plane. The resonant modes

exist for structures with α values as low as 0.5, indicating that a smooth transition can host a confined mode. The calculated mode volume is 20 $\left(\frac{\lambda}{n}\right)^3$, and Q-factor on the order of 10^4.

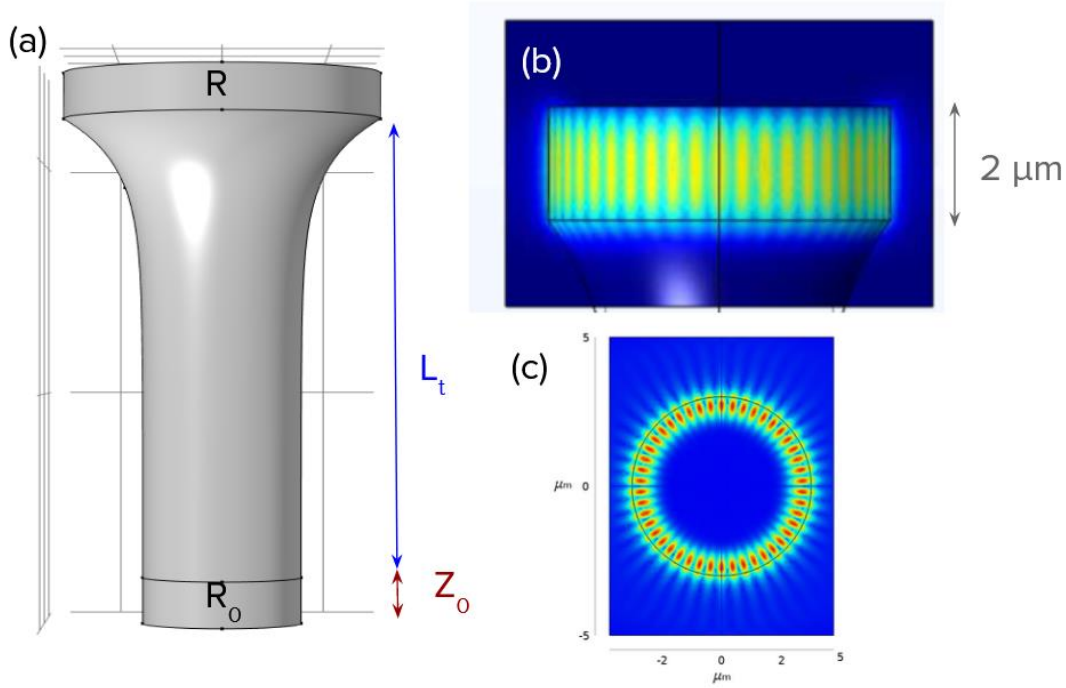

Figure 6.2 - (a) Schematics of the proposed structure. (b) Electric field profile at the *xz* and *xy* (c) planes.
Source: By the author

To fabricate these new geometries, the fabrication algorithm is modified to implement Eq. 6.1. Figure 6.3 shows the *xz*-plane for structures with a transition length of $50\ \mu$m fabricated with different values of α.

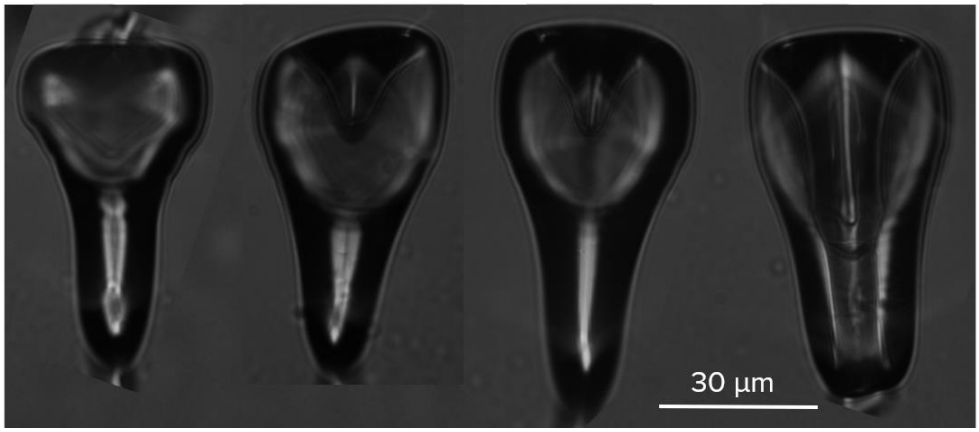

Figure 6.3 - Optical micrographies of *xz*-plane of structures fabricated with increasing values of α parameter.
Source: By the author

Subsequently, we estimated the minimum disk height that can be achieved. Figure 6.4 shows structures fabricated with final radius of 30 μm (a) and 15 μm (b), where the disk was built with only one layer, so its height is constrained by the voxel size.

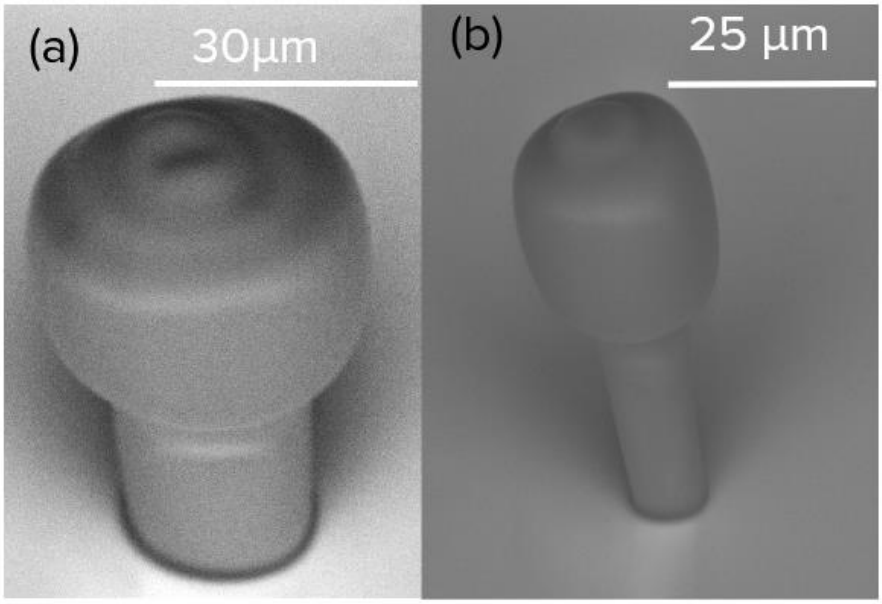

Figure 6.4 - SEM micrographies of structures with disk radius of 30 μm (a) and 15 μm (b).
Source: By the author

To estimate the minimum height that can be fabricated with the 0.25 NA objective, similar structures as shown in Fig. 6.4(a) were fabricated using different laser powers. By measuring the disk height as a function of the laser power (P), it is possible to fit the data with an adaptation of the function given by Eq. 2.75:

$$Z(P) = \frac{4\pi w_0}{\lambda}\sqrt{\left(\frac{P}{P_{tsh}}\right)^{0.5} - 1} \tag{6.2}$$

where P_{tsh} (2PP threshold power) and w_0 (beam waist) are free parameters. The fitting, shown in Fig. 6.5, yields $P_{tsh} = 79 \pm 1\, mW$ and $w_0 = 2.48 \pm 0.03\, \mu$m. As can be seen in Fig 6.5, the minimum voxel length (and therefore disk heigh), is about 10 μm. To further reduce the mode volume, a lower w_0 is necessary, which demands a higher NA

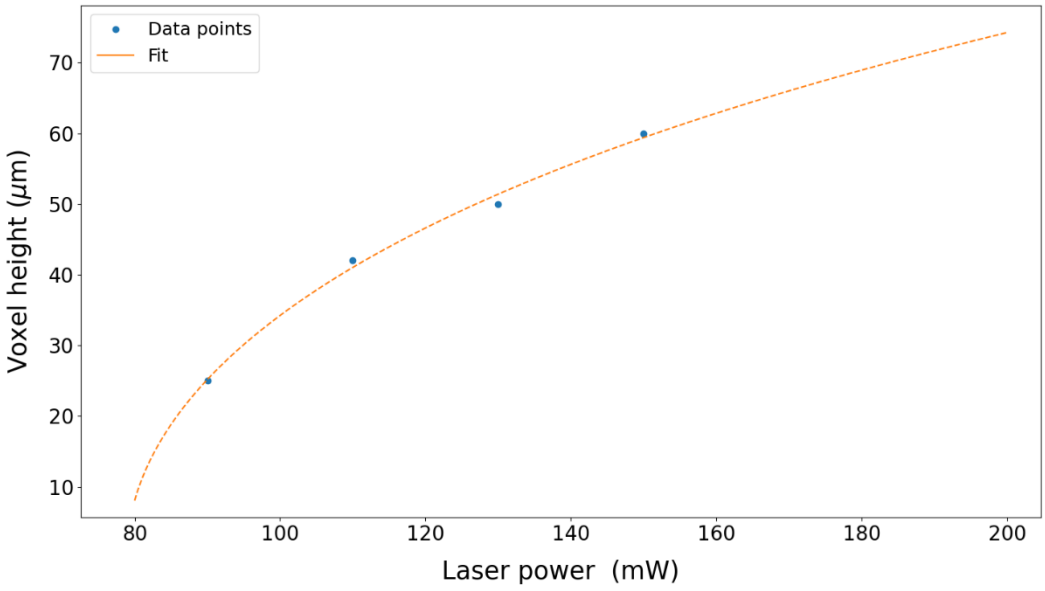

Figure 6.5 - Data points and curve fit of the voxel height as function of laser power.
Source: by the author

6.3 Disk cavity fabricated with 0.65 NA objective

Figure 6.6 shows a structure fabricated in the same conditions as structures presented in Fig. 6.4, using a 0.65 NA objective. The step in the *z*-direction is 5 μm higher than the voxel height, which is around 2 μm. Therefore, this NA is suitable for

fabricating structures that can significantly decrease the mode volume, although it requires re-optimizing fabrication parameters.

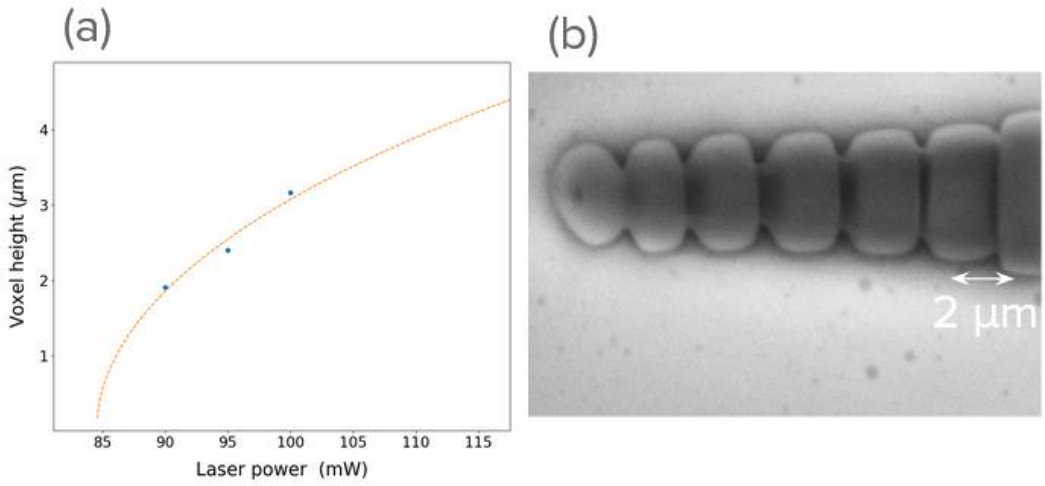

Figure 6.6 - SEM image of a structure fabricated with a 0.65 NA objective, with step between layers of 5 μm.
Source: By the author

The results indicate that a smaller step in the *z*-direction is necessary to fabricate these structures. However, due to the limitations of the step motor resolution, achieving complete overlap between each layer may not be possible. To investigate if a single layer with partial overlap between adjacent slices could support a confined mode, avoiding losses due to propagation into the lower layers, FDTD simulations were conducted. Results shown in Fig. 6.7 indicate that a structure of 3.5 μm disks, with a 1 μm overlap in the *z*-direction, and radius difference greater than $1\,\mu$m would allow high Q ($> 10^5$) WGM resonances at the top disk, with mode volumes around 100 $\left(\frac{\lambda}{n}\right)^3$.

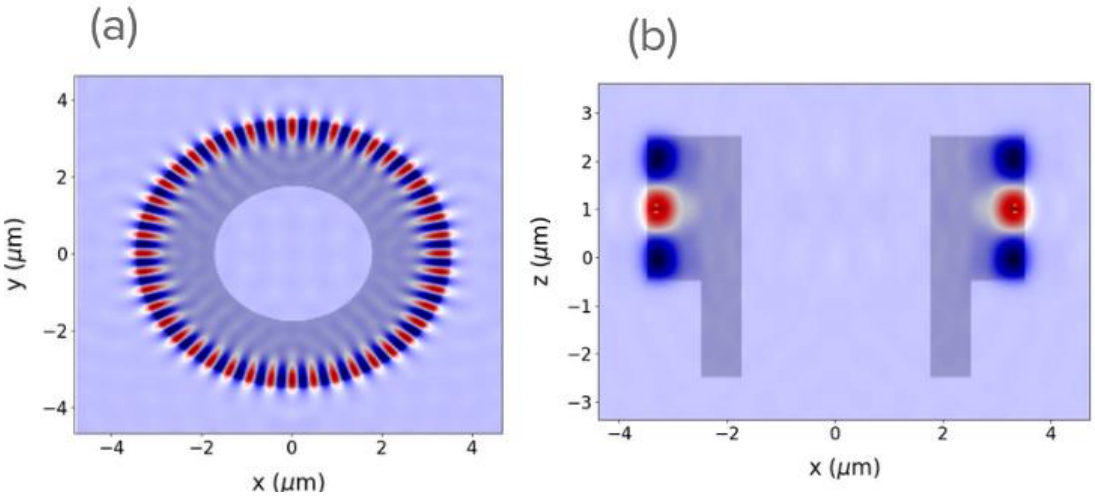

Figure 6.7 - *xy* (a) and *xz* (b) transversal planes of a WGM resonance in a disk.
Source: By the author

To fabricate these structures, we used a photoresist doped with 0.002 wt% of nanodiamonds. The design incorporates ten transition layers with α parameter set as 0.9 μm^{-1}. This value was chosen to support an upper disk with a radius around 5 μm smaller than the previous one. Figure 6.8(a) shows a SEM micrograph of such

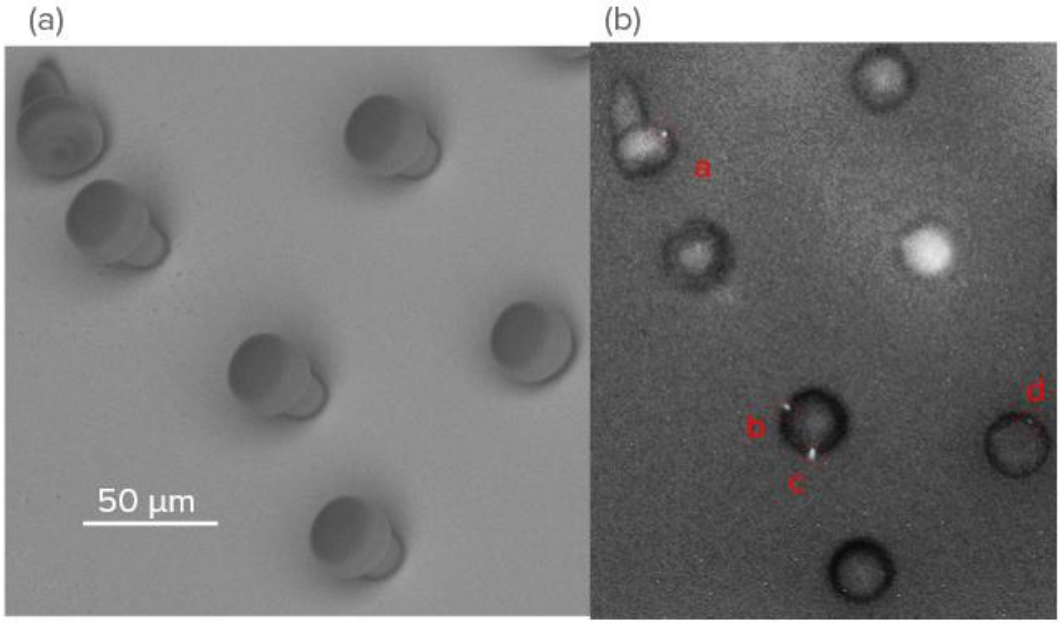

Figure 6.8 - (a) SEM micrograph of the disk structures fabricated with doped photoresist taken at a 45-degree angle. (b) LSM over green light irradiation of the structures, where 4 fluorescent spots can be identified.
Source: By the author

To map the fluorescent nanodiamonds in the structures, we imaged the structures under green light illumination using a LSM microscope, integrated over 60 seconds. The results, presented in Fig. 6.8(b), show at least four fluorescent spots. Their spectra were analyzed using the setup described in Chapter 3.5 and are shown in Figure 6.9.

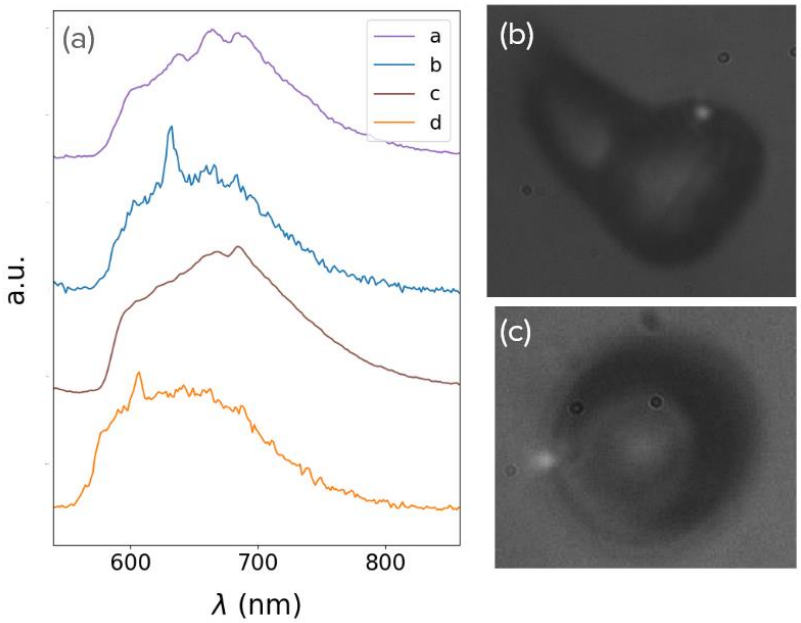

Figure 6.9 - (a) Emission spectra of each fluorescence spot from disk structures fabricated with a 0.65 NA objective. (b) Fluorescence image of nanodiamond a. (c) Fluorescence image of nanodiamond b.
Source: By the author

In Fig. 6.9(a), spectra a and c show no distinct features compared to a regular NV^- spectrum, while (b) and (d) exhibit peaks at 631.6 nm and 606.5 nm, respectively. Comparing with the results presented in Fig. 4.12, the peak in (b) (631 nm) can be related to a Raman peak attributed to the polymeric matrix. To further confirm this, spectrum d was acquired using the 514 nm line of an argon laser. The energy difference between the peaks in spectrum (b) and (d) (632 nm and 603 nm) matches the energy difference for the excitation (532 nm and 514 nm). The absence of the Raman peak in spectra (a) and (d) is due to their higher fluorescence, suggesting a higher number of NV centers at these locations.

The measurements presented in Fig. 6.9 were taken using a spectral resolution exceeding 0.8 nm. Consequently, resolving resonances with linewidths smaller than

0.05 nm (corresponding to Q factors greater than 10^4) would not be possible. Figure 6.10 compares the spectrum (b) of Fig. 6.9, measured using the confocal setup described in Chapter 3.5, with the spectrum obtained with a commercial LabRAM equipment (Fig. 4.12). It is possible to note that the peak at 631.6, which exhibits a linewidth of about 4 nm in the LabRAM equipment, can be resolved by the confocal setup. However, the peaks at 583 nm and 586 nm, with linewidths lower than 0.5 nm, remain unresolved despite having similar intensities to the resolved peak at 631.6 nm.

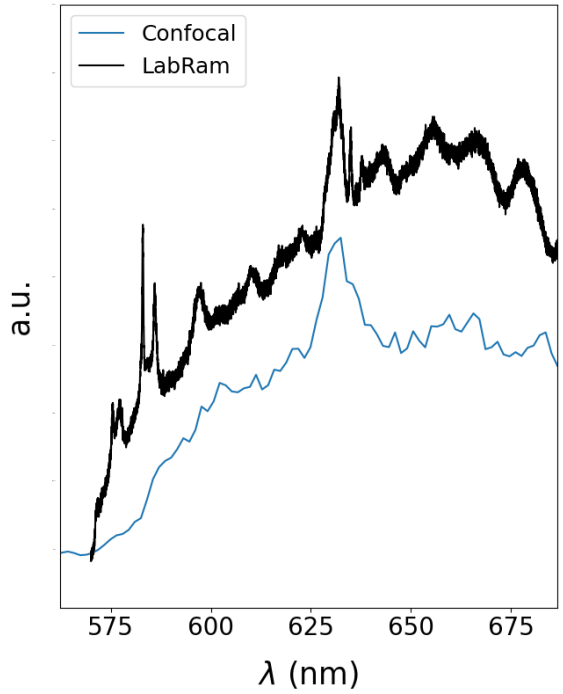

Figure 6.10 – Normalized spectrum obtained with LabRAM equipment (black line) and homemade confocal setup (Blue line).
Source: By the author

containing NV centers that theoretically possess a Q/V factor exceeding one hundred. This suggests that further optimization of the fabrication process to achieve higher Q-factors, along with employing a system with superior spectral resolution, could enable Purcell enhancement to be experimentally observed.

7 Conclusions and outlook

This work investigated novel approaches for incorporating color centers into photonic structures and explored innovative cavity designs to achieve efficient cavity-emitter coupling. We implemented these strategies in two distinct platforms: polymeric structures doped with nanodiamonds fabricated via two-photon polymerization (2PP) and silicon carbide (SiC) nanobeams realized through traditional lithographic and etching processes.

We successfully demonstrated the feasibility of fabricating photonic structures containing NV color centers embedded in nanodiamonds using the 2PP technique. By exploring the trade-off between nanodiamond concentration and resulting structural quality, we found that concentrations ranging from 0.005% to 0.002 wt% in the photoresist yielded structures containing 1 to 3 fluorescent spots per 8×10^4 μm³ (cubic micrometers). These structures exhibited good structural quality and high Q-factors on the order of 10^4 to 10^5. Raman and PL measurements confirmed the presence and specific positioning of fluorescent nanodiamonds within the fabricated structures.

Additionally, we explored, via FDTD simulations, novel designs for efficient emitter-cavity coupling with color centers in 4H-SiC nanostructures. We optimized a design for a double nanobeam cavity that can host two independent resonances, each one with Q-factors on the order of 10^4 and mode volumes on the order of 1 $\left(\frac{\lambda}{n}\right)^3$, and explored efficient ways for independently tuning each resonance. We also explored a new ‘sawfish’ cavity design, which has promising features that can ease fabrication issues of nanocavities in SiC and promote a better cavity-dipole alignment with the V_{Si} color-center. Additionally, different optimized edge coupler designs for this nanocavity were proposed. These results help to augment the range of applications of color centers in SiC in quantum technologies.

Leveraging the expertise gained from optimizing SiC cavities, we explored new designs for improved cavity-emitter coupling with nanodiamond-doped resonators fabricated via 2PP, aiming to achieve an experimentally observable Purcell enhancement. A critical challenge for achieving strong coupling is isolating the cavity from the substrate due to the low refractive index contrast between the polymer and the substrate. We addressed this challenge by proposing a fabrication protocol that

leverages existing techniques to fabricate cylindrical resonators to produce disk-like cavities. These disk resonators aim for better field confinement and hence a lower mode volume. Structures containing disks of 6 μm radii and $3\,\mu$m height were successfully fabricated, and simulations showed a theoretical Q/V factor on the order of 100 $\left(\frac{\lambda}{n}\right)^{-3}$, indicating a possible two orders of magnitude improvement for the cylinder resonators fabricated with the 0.25 NA objective.

The results presented in this work pave the way for exploiting the versatility of the 2PP technique to a wider range of quantum technology applications with color centers in nanodiamonds. Further optimization in fabrication parameters can produce polymeric cavities with high interaction with NV color-centers, using a simple and fast fabrication technique. Also, exploring higher NA objectives and characterizing the optical properties of smaller structures is a possible continuity to this work. Additionally, the fabrication protocol that creates optical insulation between resonator and substrate holds promise for applications beyond the current research.

Moreover, the doping protocol and characterization of the photoresist developed in this work set the stage for applications of 2PP in quantum sensing applications. As an example, studying the effects of strain in the polymeric matrix in the ODMR signal of the NV center can be explored as a pressure sensor. Other structures, such as waveguides, can be potentially explored. Additionally, the versatility of 2PP and biocompatibility of the polymer form a promising platform for biological sensing applications. Finally, this work can be a starting point for exploring the incorporation of other color centers in diamond and other materials into the photoresist.

REFERENCES

1 NAWROCKI, W. Some physical limits for miniaturization of electronic devices. *In*: BORISENKO, V. (ed.) **Physics, chemistry and application of nanostructures**. New York: World Scientific, 2009. p.557-560. DOI:10.1142/9789814280365_0131.

2 LUO, W. *et al*. Recent progress in quantum photonic chips for quantum communication and internet. **Light**: science & applications, v.12, p.175, 2023.

3 ZHANG, G. *et al*. An integrated silicon photonic chip platform for continuous-variable quantum key distribution. **Nature Photonics**, v. 13, p. 839–842, 2019.

4 KNALL, E. N. *et al*. Efficient source of shaped single photons based on an integrated diamond nanophotonic system. **Physical Review Letters**, v. 129, n.5, p.53603, 2022.

5 PIRANDOLA, S. *et al*. Advances in photonic quantum sensing. **Nature Photonics**, v.12, p.724–733, 2018.

6 SANTORI, C. *et al*. Nanophotonics for quantum optics using nitrogen-vacancy centers in diamond. **Nanotechnology**, 21, n.27, p.1-11, 2010.

7 MOODY, G. *et al*. Roadmap on integrated quantum photonics. **Journal of Physics**: photonics, v. 4, p. 012501, 2022.

8 HARVEY, S. P. **Quantum dots/spin qubits**. Oxford: Oxford University Press, 2022. DOI: 10.1093/acrefore/9780190871994.013.83.

9 CASTELVECCHI, D. Quantum-computing approach uses single molecules as qubits for first time. **Nature**, 2023. DOI: 10.1038/d41586-023-03943-1.

10 RASMUSSEN, S. E. *et al*. Superconducting circuit companio: an introduction with worked examples. **PRX Quantum**, v. 2, p.040204, 2021.

11 IRBER, D. M. *et al*. Robust all-optical single-shot readout of nitrogen-vacancy centers in diamond. **Nature Communications**, v. 12, n.532, 2021.

12 KURTSIEFER, C. *et al*. Stable solid-state source of single photons. **Physical Review Letters**, v.85, p.290–293, 2000.

13 GRUBER, A. *et al*. Scanning confocal optical microscopy and magnetic resonance on single defect centers. **Science**, v. 276, n.5321, p. 2012–2014, 1997.

14 ZHANG, T. *et al*. Toward quantitative bio-sensing with nitrogen-vacancy center in Diamond. **ACS Sensors**, v. 6, p.2077–2107, 2021. DOI: 10.1021/acssensors.1c00415.

15 WU, K. et al. Applying NV center-based quantum sensing to study intracellular free radical response upon viral infections. **Redox Biology**, v.52, p.1-11, 2022.

16 WALDHERR, G. *et al*. Dark states of single nitrogen-vacancy centers in diamond unraveled by single shot NMR. **Physical Review Letters**, v.106, n.5, p.157601, 2011.

17 XU, Z. *et al*. Quantum information processing with closely-spaced diamond color centers in strain and magnetic fields. **Optical Materials Express**, v.9, n.12, p.4654-4668, 2019. DOI: 10.1364/OME.9.004654.

18 CHILDRESS, L. *et al*. Coherent dynamics of coupled electron and nuclear spin qubits in diamond. **Science**, v. 314, p.281–285, 2006.

19 RADULASKI, M. *et al*. Nanodiamond integration with photonic devices. **Laser and Photonics Reviews**, v. 13, n.8, p.1800306, 2019. DOI: 10.1002/lpor.201800316 .

20 BUREK, M. J. *et al*. High quality-factor optical nanocavities in bulk single-crystal diamond. **Nature Communications**, v. 5, p.5718, 2014.

21 SCHRÖDER, T. *et al*. Quantum nanophotonics in diamond. **Journal of the Optical Society of America B**, v.33, n.4, p. B65-B83, 2016.

22 BARCLAY, P. E. *et al*. Coherent interference effects in a nano-assembled diamond NV center cavity-QED system. **Optics Express**, v.17, p. 8081, 2009.

23 WOLTERS, J. *et al*. Enhancement of the zero phonon line emission from a single nitrogen vacancy center in a nanodiamond via coupling to a photonic crystal cavity. **Applied Physics Letters**, v.97, n.14, p.141108, 2010.

24 SCHIETINGER, S.; SCHRÖDER, T.; BENSON, O. One-by-one coupling of single defect centers in nanodiamonds to high-Q modes of an optical microresonator. **Nano Letters**, v. 8, p3911–3915, 2008.

25 BARCLAY, P. E. *et al.* Chip-based microcavities coupled to nitrogen-vacancy centers in single crystal diamond. **Applied Physics Letters**, v. 95, n.19, p. 19115, 2009.

26 RIEDEL, D. *et al*. Deterministic enhancement of coherent photon generation from a nitrogen-vacancy center in ultrapure diamond. **Physical Review X**, v. 7, p.31040, 2017.

27 JUNG, T. *et al*. Spin measurements of NV centers coupled to a photonic crystal cavity. **APL Photonics**, v.4, p.120803, 2019.

28 VOROBYOV, V. V. *et al*. Coupling of single nv center to adiabatically tapered optical single mode fiber. **European Physical Journal D**, v.70, p.269, 2016.

29 ZOLLER, P. *et al*. Quantum information processing and communication. **European Physical Journal D**, v.36, p. 203–228, 2005.

30 SERBIN, J.; OVSIANIKOV, A.; CHICHKOV, B. Fabrication of woodpile structures by two-photon polymerization and investigation of their optical properties. Optics Express, v.12, n.21, p.5221-5228, 2004.

31 NOCENTINI, S. *et al*. Three-dimensional photonic circuits in rigid and soft Polymers tunable by light. **ACS Photonics**, v. 5, p.3222–3230, 2018.

32 GITTARD, S. D. *et al*. Two photon polymerization-micromolding of polyethylene glycol-gentamicin sulfate microneedles. **Advances Engeneering Materials**, v.12, n.4, p. B77-B82, 2010.

33 ZHANG, S. *et al*. High-Q polymer microcavities integrated on a multicore fiber facet for vapor sensing. **Advanced Optical Materials**, v.7, n.20, 2019.

34 OTUKA, A. J. G. *et al*. Two-photon polymerization: functionalized microstructures, micro-resonators, and bio-scaffolds. **Polymers**, v.13, n.12, p.1-30, 2021.

35 OTUKA, A. J. G. *et al*. Single-walled carbon nanotubes functionalized with carboxylic acid for fabricating polymeric composite microstructures. **Journal of Nanoscience and Nanotechnology**, v. 15, p.9797–9801, 2015.

36 TOMAZIO, N. B.; DE BONI, L.; MENDONCA, C. R. Low threshold Rhodamine-doped whispering gallery mode microlasers fabricated by direct laser writing. **Scientific Reports**, v. 7, p.1-7, 2017.

37 TOMAZIO, N. B. *et al*. Mode cleaning in graphene oxide-doped polymeric whispering gallery mode microresonators. **Journal Materials Chemistry C**, v. 8, p. 9707–9713, 2020.

38 TOMAZIO, N. B. **Direct laser writing of high-Q polymeric microresonators for photonics**. 2020. 122p. Thesis (Doctor in Science) – Instituto de Física de São Carlos, Universidade de São Paulo, São Carlos, 2020. DOI: 10.11606/T.76.2020.tde-02062020-084220.

39 HAUS, H. A. **Waves and fields in optoelectronics**. New Jersey: Prentice Hall, 1984.

40 ABRAMOWITZ, M. **Handbook of mathematical functions**. New York: Dover, 1972.

41 ZÍLIO, S. C. **Óptica moderna**. São Carlos: IFSC, 2009.

42 BALANIS, C. A. **Advanced engineering electromagnetics**. New York: Wiley, 1989.

43 CAI, M.; PAINTER, O.; VAHALA, K. J. Observation of critical coupling in a fiber taper to a silica-microsphere whispering-gallery mode system. **Physical Review Letters**, v. 85, n.1, 2000. DOI: 10.1103/physRevLett.8574.

44 AHARONOVICH, I. *et al*. Diamond-based single-photon emitters. **Reports on Progress in Physics**, v. 74, p.1-28, 2011. DOI: 10.1088/0034-4885/74/7/076501.

45 DOHERTY, M. W. *et al*. The nitrogen-vacancy colour centre in diamond. **Physics Reports**, v. 528, p. 1–45, 2013. DOI: 10.1016/j.physrep.2013.02.001.

46 SEGURA, C. O. O. **Diamond studies for applications in quantum technologies**. 2017. 115p. Thesis (Doctor in Science) - Instituto de Física de São Carlos, Universidade de São Paulo, São Carlos, 2019. DOI: 10.11606/T.76.2019.tde-01082019-152208.

47 RONDIN, L. *et al*. Surface-induced charge state conversion of nitrogen-vacancy defects in nanodiamonds. **Physical Review B**, v. 82, p. 115449, 2010.

48 BRACHER, D. O.; ZHANG, X.; HU, E. L. Selective Purcell enhancement of two closely linked zero-phonon transitions of a silicon carbide color center. **Proceedings of the National Academy of Science**, v. 114, p.4060–4065, 2017.

49 BOYD, R. W. **Nonlinear optics**. Burlington: Academic Press, 1992.

50 CORREA, D. S. *et al*. Two-photon polymerization fabrication of doped microstructures. *In*: GOMES, A. S. (ed.). **Polimerization**. London: InTech Open, 2012. DOI: 10.5772/36061.

51 PASCHOTTA, R. Gaussian beams. **RP Photonics Encyclopedia**. 2005. DOI: 10.61835/mla.

52 ADÁMAS NANOTECHNOLOGIES. Product sheet functionalized fluorescent nanodiamond. 2024. Available at: https://www.adamasnano.com/wp-content/uploads/2019/06/functionalized-FND-pdf.pdf. Accessible at: 13 May 2023.

53 BIRKS, T. A.; LI, Y. W. The shape of fiber tapers. **Journal of Lightwave Technology**, v.10, p.432–438, 1992.

54 STANCIK, A. L.; BRAUNS, E. B. A simple asymmetric lineshape for fitting infrared absorption spectra. **Vibrational Spectroscopy**, v.47, 66–69, 2008.

55 NISHIMURA, Y. *et al*. Wide-field fluorescent nanodiamond spin measurements toward real-time large-area intracellular thermometry. **Scientific Reports**, v.11, p. 4248, 2021.

56 KNIGHT, D. S.; WHITE, W. B. Characterization of diamond films by Raman spectroscopy. **Journal of Materials Research**, v.4, n.2, p.385-393, 1989.

57 TOMAZIO, N. B. *et al*. Femtosecond laser fabrication of high-Q whispering gallery mode microresonators via two-photon polymerization. **Journal of Polymer Science B**, v. 55, p. 569–574, 2017.

58 JOANNOPOULOS, J. *et al*. **Photonic crystals**: molding the flow of light. Princeton: Princeton University Press, 2008.

59 AKAHANE, Y. *et al* High-Q photonic nanocavity in a two-dimensional photonic crystal. **Nature**, v.425, p.944–947, 2003.

60 DEOTARE, P. B. *et al*. High-quality factor photonic crystal nanobeam cavities. **Applied Physics Letters**, v. 94, p.121106, 2009.

61 BUREK, M. J. *et al*. High quality-factor optical nanocavities in bulk single-crystal diamond. **Nature Communications**, v. 5, p. 5718, 2014.

62 BRACHER, D. O. **Development of photonic crystal cavities to enhance point defect emission in silicon carbide**. 2017. 199 p. Dissertation (Doctor in Philosophy) – Harvard University, Cambridge, 2017.

63 LI, L. *et al*. High-performance microring resonators fabricated with multiphoton absorption polymerization. **Advanced Materials**, v. 20, p.3668–3671, 2008.

64 OSKOOI, A. F. *et al*. Meep: a flexible free-software package for electromagnetic simulations by the FDTD method. **Computer Physics Communications**, v.181, p.687–702, 2010.

65 TAFLOVE, A.; HAGNESS, S. C.; PIKET-MAY, M. Computational electromagnetics: the finite-difference time-domain method. *In*: CHEN, W. **The electrical engineering handbook**. New York: Elsevier, 2005. p. 629-670. DOI: 10.1016/B978-012170960-0/50046-3.

66 MANDELSHTAM, V. A.; TAYLOR, H. S. Harmonic inversion of time signals and its applications. **Journal of Chemical Physics**, v. 107, p. 6756–6769, 1997.

67 CHEW, W. C.; WEEDON, W. H. A. 3D perfectly matched medium from modified maxwell's equations with stretched coordinates. **Microwave Optical Technology Letters**, v. 7, p. 599–604, 1994.

68 WOLFOWICZ, G. *et al*. Optical charge state control of spin defects in 4H-SiC. **Nature Communications**, v. 8, p.1876, 2017.

69 GADALLA, M. N. *et al*. Enhanced cavity coupling to silicon vacancies in 4H silicon carbide using laser irradiation and thermal annealing. **Proceedings of the National Academy of Sciences**, v.118, 2021. DOI: 10.1073/pnas.2021768118.

70 NELDER, J. A.; MEAD, R. A Simplex method for function minimization. **Computer Journal**, v. 7, p. 308–313, 1965.

71 BOPP, J. M. *et al*. 'Sawfish' photonic crystal cavity for near-unity emitter-to-fiber interfacing in quantum network applications. **Advanced Optical Materials**, v. 12, n. 13, p.1-11, 2022. DOI: 10.1002/adom.202301286.

72 AFZAL, F. O.; HALIMI, S. I.; WEISS, S. M. Efficient side-coupling to photonic crystal nanobeam cavities via state-space overlap. **Journal of the Optical Society of America B**, v. 36, p. 585, 2019.

73 BUREK, M. J. *et al*. Fiber-coupled diamond quantum nanophotonic interface. **Physical Review Applied**, v.8, p.24026, 2017.

74 TAMBOLI, A. C. *et al*. Photoelectrochemical undercut etching of m-plane gan for microdisk applications. **Journal of Electrochemical Society**, v.156, p. H767-H771, 2009.

75 SCHRÖDER, T. *et al*. Quantum nanophotonics in diamond. **Journal of the Optical Society of America B**, v. 33, p.B65-B83, 2016.

76 CROOK, A. L. *et al*. Purcell enhancement of a single silicon carbide color center with coherent spin control. **Nano Letters**, v. 20, p.3427–3434, 2020.

77 LOUYER, Y.; MESCHEDE, D.; RAUSCHENBEUTEL, A. Tunable whispering-gallery-mode resonators for cavity quantum electrodynamics. **Physical Review A**, v. 72, p. 031801, 2005.

ANNEX A – List of publications and conference presentations

Journal papers:

1. Jorge, G.H.A.; **Couto, F.A**.; Almeida, J.M.P.; Marques, V.A.S.; Andrade, M.B.; Mendonça, C.R. Active Optical Tuning of Azopolymeric Whispering Gallery Mode Microresonators for Filter Applications. *Photonics* 2024, *11*, 167. https://doi.org/10.3390/photonics11020167

2. Clabel H., J. L.; Paula, K. T.; Pereira-da-Silva, M. A.; Vollet-Filho, J. D.; **Couto, F. A**., Marega J., E. & Mendonça, C. R. (2023). Femtosecond laser-induced crystallization in Er/Yb:BaTiO3 perovskite films: Effects on the optical and electrical properties. *Applied Surface Science*, *642*. https://doi.org/10.1016/j.apsusc.2023.158634

3. **Couto, F. A**.; Andrade, M. B.; Otuka, A. J. G.; Pratavieira, S.; Muniz, S. R. & Mendonça, C. R. (2023). Integrating Fluorescent Nanodiamonds into Polymeric Microstructures Fabricated by Two-Photon Polymerization. *Nanomaterials*, *13*(18), 2571. https://doi.org/10.3390/nano13182571

4. Nolasco, L. K.; **Couto, F. A**.; Andrade, M. B. & Mendonça, C. R. (2023). Femtosecond laser micromachining study with multiple wavelengths in CVD diamond. *Diamond and Related Materials*, *131*. https://doi.org/10.1016/j.diamond.2022.109589

5. **Couto, F. A**.; Paula, K. T.; Santos, M. v.; Ribeiro, S. J. L. & Mendonça, C. R. (2023). Direct femtosecond laser printing of silk fibroin periodic structure with lower mid-infrared reflectivity. *Optical Materials*, *135*. https://doi.org/10.1016/j.optmat.2022.113335

6. Santos, S. N. C.; Paula, K. T.; **Couto, F. A**.; Facure, M. H. M.; Correa, D. S. & Mendonca, C. R. (2022). Femtosecond laser micromachining optical waveguides on transparent silica xerogels. *Optical Materials*, *132*. https://doi.org/10.1016/j.optmat.2022.112819

Conference Papers:

Couto, F. A., Andrade, M. B., Otuka, A. J. G., Pratavieira, S., Muniz, S. R., & Mendonça, C. R. (2023). Microresonators With Nanodiamonds Fabricated via Two-Photon Polymerization for Quantum Photonics. *CLEO 2023*, JTh2A.43. https://doi.org/10.1364/CLEO_AT.2023.JTh2A.43

Couto, F. A., Paula, K. T., Santos, M. v., Ribeiro, S. J. L., & Mendonça, C. R. (2023). Silk Fibroin Periodic Surface With Low Mid-Infrared Reflectivity Fabricated via Laser-Induced Forward Transfer. *CLEO 2023*, JTu2A.14. https://doi.org/10.1364/CLEO_AT.2023.JTu2A.14

Couto, F. A., Otuka, A. J. G., & Mendonça, C. R. (2022). Preparation of Fluorescent Nanodiamond Doped Photoresist for Fabrication via Two-Photon Polymerization Technique. *Latin America Optics and Photonics (LAOP) Conference 2022*, M3D.4. https://doi.org/10.1364/LAOP.2022.M3D.4

Couto, F. A., Tomazio, N. B., & Mendonça, C. R. (2022). Coupling Efficiency of Radial Whispering Gallery Modes via Finite-Element Simulation. *Latin America Optics and Photonics (LAOP) Conference 2022*, M4D.3. https://doi.org/10.1364/LAOP.2022.M4D.3

Presentation in international conference:

SPIE Photonics West San Francisco, CA – 2024
Oral presentation: *Mode-cleaning effects in graphene oxide-doped microresonators fabricated via two-photon polymerization: A finite-element simulation analysis*

MSR 2023 Fall meeting Boston, MA – 2023
Poster presentation: *Fabrication of Polymeric Microresonators Embedded with NV Color Centers in Nanodiamonds using Two-Photon Polymerization*

CLEO Conference San Jose, CA – 2023
Poster presentation: *Microresonators With Nanodiamonds Fabricated via Two-Photon Polymerization for Quantum Photonics*

CLEO Conference San Jose, CA – 2023
Poster presentation: *Fibroin Periodic Surface With Low Mid-Infrared Reflectivity Fabricated via Laser-Induced Forward Transfer*

Latin America Optics and Photonics Conference (LAOP) Recife, PE, Brazil – 2022
Oral presentation: *Preparation of Fluorescent Nanodiamond Doped Photoresist for Fabrication via Two-Photon Polymerization Technique*

Latin America Optics and Photonics Conference (LAOP) Recife, PE, Brazil – 2022
Oral presentation: *Coupling Efficiency of Radial Whispering Gallery Modes via Finite-Element Simulation*